UNIVERSITY OF CALIFORNIA SAN DIEGO

Multiscale Computational Approaches for the study of Dilated Cardiomyopathy Mechanisms and Therapy

A dissertation submitted in partial satisfaction of the
requirements for the degree of Doctor of Philosophy

in

Bioengineering with a Specialization in Multi-Scale Biology

by

Kimberly Joan McCabe

Committee in charge:

Professor Andrew D McCulloch, Chair
Professor James A McCammon, Co-Chair
Professor Rommie A Amaro
Professor Ju Chen
Professor Jeffrey H Omens

2019

The Dissertation of Kimberly Joan McCabe is approved and is acceptable in quality and form for publication on microfilm and electronically:

_____

_____

_____

_____
Co-Chair

_____
Chair

University of California San Diego

2019

DEDICATION

In recognition of the sacrifices she made so that I could freely pursue my goals, the unending support she has provided, and the example she set as a tireless achiever, this dissertation is dedicated to my mother, Robin J McCabe.

I also dedicate this work to the memory of my father, Thomas P McCabe. He was an unapologetically kind and resilient hero who instilled in me a love of history and honest debate. His untimely passing due to acute heart failure has inspired my scientific direction.

TABLE OF CONTENTS

LIST OF FIGURES

LIST OF TABLES

ACKNOWLEDGEMENTS

I would like to acknowledge Professor Andrew D McCulloch for his support as the chair of my committee. His guidance through moments of scientific curiosity and uncertainty helped me keep pushing toward success.

I was co-advised by Michael Regnier at the University of Washington, and wish to acknowledge his support and scientific direction.

I would also like to acknowledge the Cardiac Mechanics Research Group, who have provided scientific guidance, constructive feedback, and many fond moments. Special thanks to Jen Stowe, Yasser Aboelkassem, Sukriti Dewan, Kevin Vincent, Abby Teitgen, William Valdez, and Nickolas Forsch.

Members of the McCammon and Amaro lab provided technical and theoretical support during my late start in the world of computational biochemistry. Thanks especially to Sophia Hirakis, Christopher Lee, Ben Jagger, and Bryn Taylor.

The Introduction contains excerpts of the material as it appears in: Dewan, S*, McCabe, KJ*, Regnier, M, McCulloch, AD (2017). ”Insights and Challenges of Multi-scale Modeling of Sarcomere Mechanics in cTn and Tm DCM mutants-Genotype to Cellular Phenotype”. Frontiers in Physiology, 8, p 151. The dissertation author was the co-first author of this review article.

Chapter 1, in full, is a reprint of the material as it appears in: Dewan S, McCabe KJ, Regnier M, McCulloch AD, Lindert S (2016) ”Molecular Effects of cTnC DCM Mutations on Calcium Sensitivity and Myofilament Activation - An Integrated Multi-Scale Modeling Study”. J. Phys. Chem. 120(33), pp 8264-8275. The dissertation author was the second author of this paper, and contributed the subcellular markov state ODE model to the work.

Chapter 2 contains excerpts of material as it appears in Aboelkassem Y, McCabe KJ, Huber G, Regnier M, McCammon JA, McCulloch AD (2019) ”A Coarse-Grained Multiscale Model of Thin Filament Activation using Brownian and Langevin Dynamics”. Biophysical

Journal. *(Submitted)*. The dissertation author was a contributing author on this publication, but her specific contributions are the only elements contained herein.

Chapter 3 contains excerpts of material as it appears in: Powers JD, Yuan C, McCabe KJ, Murray JD, Childers MC, Flint GV, Moussavi-Harami F, Mohran S, Castillo R, Zuzek C, Ma W, Daggett V, McCulloch AD, Irving TC, Regnier M. (2019) "Cardiac myosin activation with 2-deoxy-ATP: A charged affair". PNAS. *(In Press)*. The dissertation author was a contributing author on this publication, but her specific contributions are the only elements contained herein.

Chapter 4, in full, has been submitted for publication of the material: McCabe KJ, Aboelkassem Y, Dewan S, Regnier M, and McCulloch AD. "Predicting the effects of dATP on cardiac contraction using a Markov Chain model of the sarcomere". J Physiol. *(Submitted)*. The dissertation author was the primary investigator and author of this material.

Chapter 5, in full, is currently being prepared for submission for publication of the material: McCabe KJ, Hirakis SP, Teitgen AE, Duclos A, Regnier M, Amaro RE, and McCulloch AD. "A multiscale computational modeling study to determine the effects of 2-deoxy-ATP on SERCA pump function". *(in preparation)*. The dissertation author was the primary investigator and author of this material.

VITA

2013	Bachelor of Science, Biomedical Engineering, Yale University
2013–2014	Management Science Consultant
2014–2016	Teaching Assistant, Department of Bioengineering University of California, San Diego
2016	Master of Science, Bioengineering, University of California, San Diego
2014–2019	Research Assistant, University of California, San Diego
2019	Doctor of Philosophy, Bioengineering with a Specialization in Multi-Scale Biology, University of California, San Diego

PUBLICATIONS

Dewan, S*, McCabe, KJ*, Regnier, M, McCulloch, AD (2017). ”Insights and Challenges of Multi-scale Modeling of Sarcomere Mechanics in cTn and Tm DCM mutants-Genotype to Cellular Phenotype”. Frontiers in Physiology, 8, p 151. * Co-first Author

Dewan S, McCabe KJ, Regnier M, McCulloch AD, Lindert S (2016) ”Molecular Effects of cTnC DCM Mutations on Calcium Sensitivity and Myofilament Activation - An Integrated Multi-Scale Modeling Study”. J. Phys. Chem. 120(33), pp 8264-8275.

Powers JD, Yuan C, McCabe KJ, Murray JD, Childers MC, Flint GV, Moussavi-Harami F, Mohran S, Castillo R, Zuzek C, Ma W, Daggett V, McCulloch AD, Irving TC, Regnier M. (2019) ”Cardiac myosin activation with 2-deoxy-ATP: A charged affair”. PNAS. *(In Press)*.

Aboelkassem Y, McCabe KJ, Huber G, Regnier M, McCammon JA, McCulloch AD (2019) ”A Coarse-Grained Multiscale Model of Thin Filament Activation using Brownian and Langevin Dynamics”. Biophysical Journal. *(Submitted)*.

McCabe KJ, Aboelkassem Y, Dewan S, Regnier M, and McCulloch AD. ”Predicting the effects of dATP on cardiac contraction using a Markov Chain model of the sarcomere”. J Physiol. *(Submitted)*.

McCabe KJ, Hirakis SP, Teitgen AE, Duclos A, Regnier M, Amaro RE, and McCulloch AD. ”A multiscale computational modeling study to determine the effects of 2-deoxy-ATP on SERCA pump function”. *(in preparation)*.

FIELDS OF STUDY

Major Field: Bioengineering with a Specialization in Multi-Scale Biology

ABSTRACT OF THE DISSERTATION

Multiscale Computational Approaches for the study of Dilated Cardiomyopathy Mechanisms and Therapy

by

Kimberly Joan McCabe

Doctor of Philosophy in Bioengineering with a Specialization in Multi-Scale Biology

University of California San Diego, 2019

Professor Andrew D McCulloch, Chair
Professor James A McCammon, Co-Chair

Dilated Cardiomyopathy (DCM) is a major cause of cardiac death which can arise via various mutations in the contractile proteins of the cardiomyocyte. In order to explore subcellular mechanisms of this disease and a potential treatment called 2-deoxy-ATP (dATP), we employ multiscale modeling from the atomistic to cellular level. We use molecular dynamics (MD) and Brownian dynamics (BD) studies to explore the effects of 3 major DCM-associated mutations (D75Y,E59D, and G159D) on cardiac troponin C, and integrate simulation-gathered transition rates into a Markov State model (MSM) of the sarcomere to predict cellular contractile effects. We employ BD simulations to probe the electrostatic affinity of tropomyosin as it

rotates about the actin thin filament, developing a multi-well energy landscape which can be used in higher-order stochastic models of sarcomere activation. Using BD, we discover that dATP-bound myosin has increased affinity to an actin dimer compared to ATP-myosin, indicating that dATP treatment enhances crossbridge (XB) attachment rates. Integrating this information into a Monte Carlo MSM of crossbridge cycling, we quantify the effect of dATP treatment on XB attachment, powerstroke and detachment rates which explain augmented force development and magnitude in both steady-state and twitch simulations. Finally, we investigate the effects of dATP on calcium handling through Gaussian accelerated MD on apo, Mg.ATP-bound, and Mg.dATP-bound SR-ATPase (SERCA 2A) to determine effects of the drug on protein conformation. BD is employed to measure ATP- vs dATP- association rates as well as Ca^{2+} binding rates. We found that dATP has higher affinity for SERCA 2A than ATP, and when dATP is bound Ca^{2+} prefers to bind calcium Site II rather than Site I, in direct opposition to the ATP case. We found that these two rate differences can partially explain experimentally noted effects of dATP on the calcium transient when scaled up to an ODE model of calcium handling, but we can fully explain the effects by altering other rates in the SERCA cycle and analyzing other Ca^{2+}-ATPases. These studies provide pipelines for the integration of computational technologies at multiple spatial and temporal scales to answer biophysical questions about DCM mechanisms and treatments.

Introduction

0.1 Genetic underpinnings of Dilated Cardiomyopathy

Dilated Cardiomyopathy (DCM) is one of the four classified forms of cardiomyopathy besides hypertrophic cardiomyopathy (HCM), restrictive cardiomyopathy (RCM), and arrythmogenic right ventricular dysplasia/cardiomyopathy (ARVD/C) [1, 2]. DCM, one of the major causes of cardiac death, is characterized by impaired systolic function and dilatation of one or both ventricles [1, 3]. Hemodynamically, contractility is depressed and Pressure-Volume (PV) loops are right-shifted in DCM. In 30-50% of cases DCM is linked to familial etiology, including mutations in the regulatory thick and thin myofilament proteins - myosin, actin, the Troponin (Tn) complex, Tropomyosin (Tm), and Titin (Ttn) [3, 4]. Many times DCM presents with conduction defects and sequelae of other cardiac defects. This is more common with cytoskeletal and z-disc mutations [2, 5]. Genome Wide Association Studies (GWAS) have helped identify many of the sarcomeric mutations associated with the phenotype of DCM [6, 7, 8, 9, 10, 11, 12, 13, 14]. Despite the identification of sarcomeric mutations associated with DCM, it is still difficult to predict the exact functional consequences of the mutation at the cellular level based on its molecular structure and function. Identified sarcomeric mutations may represent a gain of function or loss of function at the cellular level, as assessed by myofilament mechanics [6, 15, 16]. Furthermore, a spatial and temporal translation of the cellular level mechanical phenotype to an organ level DCM phenotype has not been seamlessly achieved. These patho-physiological translative events from genetic to molecular to cellular to organ level, underscore the need for investigation at and across all biological scales to fully

comprehend the development of DCM and potential treatments [17].

Experimental studies, using the skinned muscle preparation or intact cardiomyocytes from gene-targeted mouse models [18], adenoviral-mediated transfection [19, 20, 21, 22], in-vitro protein exchange experiments [23] for in-vitro protein motility assays [21, 24], mammalian two-hybrid luciferase assay system [9, 10], steady-state force-calcium assays [19, 20], and contractility assays [25, 22, 23], have reported alterations in key mechanical properties of myofilaments in DCM. These include changes in calcium sensitivity [26, 21, 18, 22, 23, 24, 27], thick and thin myofilament cooperativity and cross-bridge (XB) cycling rates [28], as a functional outcome of many identified sarcomeric DCM mutations. Most studies have reported a decrease in calcium sensitivity of myofilaments as a consistent functional phenotype for DCM identified sarcomere mutations [10, 21, 18, 29, 24]. Interestingly, I61Q cTnC mutant in mice (neither found nor associated with DCM clinically), that has decreased calcium myofilament binding affinity, recapitulates DCM phenotype cellularly and *in vivo* [30]. However, exceptions to this have been reported wherein both an increase and no change in calcium sensitivity were reported in DCM [31, 24]. Dweck et al. reported that there is a decrease in calcium sensitivity of tension development in G159D cTnC mutant only when it is incorporated in regulated actomyosin filaments and not in isolated cTnC [31], highlighting the effect of protein interactions as the hierarchy of structural organization becomes more physiological and complex in the contractile apparatus. Furthermore, Memo et al. reported a decrease in calcium sensitivity of myofilaments for four DCM associated mutants (K36Q TnI, R141W TnT, ΔK210 TnT, E40K Tm), no change in calcium sensitivity of one mutant (E54K Tm) and increase in calcium sensitivity in another (D230N Tm) [24]. These observations suggest that decreased calcium sensitivity is a dominant stimulus sufficient to cause DCM, but is neither necessary, nor the only cellular mechanism triggering the remodeling observed in DCM. A recent study postulated that the blunting of the relationship between calcium sensitivity of myofilaments and PKA mediated beta-adrenergic stimulation via cTnI phosphorylation [24] in sarcomeric

DCM mutants might be the defining cellular phenotype for DCM regardless of the directional shift in calcium sensitivity. It should be noted that aside from DCM mutations in contractile sarcomere proteins that lead to diminished force production, mutations in other key cytoskeletal and sarcomere proteins like the z-disc proteins and Titin can lead to disruptions in transmission of force, sensing of force and mechano-transduction which are also causative toward DCM [5]. These observations suggest that molecular interactions and effects of various DCM mutants converge to a depressed contractile phenotype at the cellular level due to alterations in (a) calcium sensitivity of myofilaments, (b) thin-filament activation, (c) maximal ATPase activity, (d) in-vitro motility (e) calcium affinity of Tn and (f) mechano-transduction, thereby triggering the signaling mechanism leading to DCM [5, 32]. Further studies are warranted to establish the key converging cellular mechanisms and signaling pathways in DCM.

Clinically, mutations are prevalent from birth in familial DCM. However, the temporal transition to DCM is not yet understood [33]. A recent study using tissue Doppler and strain echocardiography, showed that even early on there are subtle indications [32]. In subclinical DCM mutation carriers, reduced systolic myocardial velocity, strain and strain-rate were reported despite normal LV geometry, ejection fraction and diastolic function [32]. Early diagnosis in such cases can provide with much needed time [32]. It is also important to note that some HCM patients develop dilated ventricles at later stages for example in patients with mutations E180V in Tm and R92W in cTnT [5]. Studies have shown this to be distinct from DCM phenotype [34]. So in familial DCM at the whole heart level there is subtle manifestation of DCM from birth and transition to late stage DCM eventually. Mechanical and pathway driven changes lead to this cardiac remodeling [35, 30]. Investigations on the effects of DCM mutations quantitatively and qualitatively, in animal model studies, linking genotype to muscle phenotype i.e., from molecular level changes to myofilament level changes to intact tissue level changes to whole heart level changes are scarce [36, 37]. This is due to the technical challenges and expense of carrying out such an expansive study to experimentally measure data on a single

DCM mutation. Additionally, as studies report cellular data, isolating the singular effect of the genetic mutation becomes difficult due to downstream effects of the mutation that also contribute to the systemic perturbations leading to the phenotype.

A potential way to study the mechanical effects of genetic mutations comprehensively is by multi-scale computational modeling. Cardiac muscle biomechanics has been experimentally and computationally investigated in molecular machineries of sarcomeric protein complexes [38, 39, 40], in thick and thin myofilaments [41, 42, 43], in isolated cardiomyocytes under steady-state and dynamic conditions [44, 45], in myocardium, and in the whole heart [46, 47, 48, 49, 50]. An integrative mathematical formulation to scale from protein level changes to the cardiomyocyte function is yet to be implemented. Parameterization of computational models requires collating data from various studies for a single mutation at various spatial and temporal scales. This results in data from variable experimental conditions and requires standardization in terms of (a) temperature, (b) species, and (c) bridging of spatial and temporal scales, in order to input model parameters [51, 43]. In this review we discuss various *in silico* approaches and the challenges thereof, by examining previously identified and experimentally studied DCM mutations in thin filament proteins Tn and Tm, with the goal of elucidating the mechanical effects of sarcomeric mutations from molecular level to the cellular scales.

0.2 Mechanisms of cardiac muscle contraction

Cardiac muscle contraction is triggered following calcium induced calcium release (CICR) from the sarcoplasmic reticulum (SR) [52]. In 1954, two groundbreaking studies proposed the sliding filament theory of muscle contraction describing the molecular basis of muscle contraction [53, 54]. According to the sliding filament theory, thin (actin) and thick (myosin) filaments slide past each other, while maintaining absolute lengths, during contraction to generate contractile force. Cardiac TnC (cTnC), a 18 kDa thin filament protein within the Tn complex, is a key regulator of muscle contraction. Calcium binding to cTnC triggers the

biomechanical cascade of contraction events within the sarcomere [55]. Calcium binding to cTnC induces a conformational change within the Tn complex, thereby displacing Tropomyosin (Tm) from actin filaments to expose myosin binding sites and increasing the probability of cross-bridges cycling. In the resting state of the myofilaments when Ca^{2+} is not bound to cTnC, cTn complex anchors Tm in a Blocked position, thereby, sterically hindering access to sites on the thin filament where Myosin S1 heads can bind to actin to form XBs [55]. Upon Ca^{2+} binding cTnC undergoes a conformational change, which exposes a hydrophobic patch within cTnC and allows cTnC to bind to the switch peptide subunit of cardiac Troponin I (cTnI). Once the cTnC has bound to the cTnI switch peptide, cTn complex releases the anchoring Tm, allowing the Tm molecule to slide around the actin filament. Tm molecules overlap by 7-10 residues, which leads to cooperative interactions between nearest-neighbor thick-thin myofilament proteins that can be affected by the stiffness of the Tm molecule. Tm moves from the Blocked (*B*) state to a Closed (*C*), a 25° state of rotation in which myosin binding sites are partially exposed [56, 55, 57].

When Tm enters the *C* state and partially uncovers the binding site on actin, myosin S1 heads, which make up the bulk of the thick filament, are able to attach and form force-producing crossbridges in an ATP-driven cycle. The detached myosin head binds ATP, which hydrolyzes to ADP and inorganic phosphate (Pi). The myosin S1 head can then bind the actin thin filament with a weak attachment leading to a stronger attachment. The binding event pushes Tm a further 10 ° into the Open (*M*) state, exposing myosin binding sites on the thin filament fully[56, 55]. The myosin head releases Pi as it undergoes a powerstroke, transitioning the formed crossbridge into a force producing strained state [55, 58]. ADP is then released from myosin, which can detach from the thin filament in order to bind another ATP molecule and restart the cycle. Another form of cooperativity is present during crossbridge cycling, known as XB-XB cooperativity, where a bound crossbridge can lead to nearby crossbridges binding due to a change in the angle between the myosin S1 head and the thick filament [59, 55, 60]. A third

form of cooperativity has been coined XB-RU cooperativity, and refers to the phenomenon of crossbridge formation contributing to higher Ca^{2+} affinity of nearby binding sites on actin. Cooperative mechanisms in the thick and thin filaments allow for large increases in overall force production over a relatively small physiological range of [Ca^{2+}].

During the relaxation phase of the cardiac cycle, Ca^{2+} is rapidly removed from the cytosol in order to allow calcium to unbind the Tn complex so XB cycling can cease. The SR Ca^{2+}-ATPase, also known as SERCA, is the workhorse as this process, removing 70% of Ca^{2+} in rats and up to 92% of Ca^{2+} in rabbits and humans [61, 62, 63]. The remaining cytosolic Ca^{2+} is removed using the Na^{2+}/Ca^{2+} exchanger, the sarcolemmal $^{2+}$-ATPase and the mitochondrial $^{2+}$ uniporter [62]. Large stores of Ca^{2+} are now trapped in the sarcoplasmic reticulum, ready for fast release during CICR after the next depolarization event.

0.3 2-deoxy-ATP as a therapeutic in cardiomyocytes

Cardiac contraction and Ca2+ removal mechanisms in the cardiomyocyte are largely driven by adenosine triphosphate (ATP). A similar molecule, 2-deoxy-ATP (dATP), also exists in small amounts in the cytosol and only differs from ATP by the removal of an oxygen atom from the 2' carbon of the ribose ring. In normal cell conditions, dATP concentrations are incredibly low compared to [ATP]. In fact, a study averaging nucleotide concentration data from various mammalian cells found that on average, [ATP] is 3152 $\pm$ 1698 μM, whereas [dATP] is 24 $\pm$ 22 μM, placing dATP concentration at $<$ 1% of the ATP pool [64]. dATP synthesis occurs within the cytosol via the enzyme ribonucleotide reductase [65].

The main role of dATP is to become a component of DNA structures in preparation for cell replication. However, it has also been shown to activate ATP-driven processes such as those in cardiac muscle contraction. In 2000, Regnier et. al. discovered that after replacing ATP with dATP in rat cardiac trabeculae, a 37% increase in maximal force (F_{max}) and a 55% increase in rate of tension redevelopment (k_{tr}) was observed at pCa = 4.5 [66]. Filament sliding

speed was also increased more than two-fold, leading to the hypothesis that dATP acts as a myosin activator to increase crossbridge (XB) cycling speed by increasing attachment rate f and detachment rate g (to a smaller extent) in order to increase overall cardiac force production [66]. Further study of the system showed that steady state force at all calcium concentrations, as well as tension development rates, increased in demembranated rat trabeculae both expressing the α-myosin isoform predominant in rats as well as the β-myosin isoform more heavily expressed in humans [67]. This finding further demonstrated the need to explore dATP as a therapeutic for activation of cardiac contractility [68].

A study of skinned porcine papillary muscle strips next tested the functionality of different dATP/ATP ratios on cardiac force production. At high concentrations of Ca^{2+} (pCa = 4.5), steady state force was found to increase linearly as a function of percent dATP, but a clear positive nonlinear relationship between steady-state force and percent dATP emerged at physiological [Ca^{2+}] (pCa = 5.5) [69]. This analysis suggested that dATP may have four times higher affinity for myosin than ATP, and that even modest increases to the dATP pool (10%) in cardiomyocytes has a significant impact on contractility [69]. A similar percentage study conducted in monolayers of embryonic chick cardiomyocytes found that very high levels of dATP ($> 70\ \mu$M) was associated with adverse effects such as loss of spontaneous contraction and apoptosis, but lower levels ($< 60\ \mu$M) allowed for more powerful contractions without affecting beat frequency [70]. In a later study, mechanical testing was performed on demembranated left ventricular cardiac tissue from adult humans with end-stage heart failure, where a 100% dATP solution allowed for an 35% increase in maximal isometric force at pCa 5.6 [71]. at 10% dATP, the study found a 14% increase in force, again demonstrating a positive nonlinear effect of the molecule in a new species [71]. In another heart failure study, left ventricular myofibrils from dogs with naturally-occuring DCM were treated with dATP [72]. dATP-treated tissue was found to have higher Ca^{2+}-sensitivity than untreated DCM myofibrils, and replacing ATP with dATP recovered contractility function of the muscle [72].

The method of treatment most widely explored for increasing cytosolic [dATP] in cardiomyocytes is upregulation of ribonucleotide reductase (R1R2 or TgRR). Rat cardiomyocytes overexpressing R1R2 were found to increase shortening by 40% and shortening speed by 80% at 0.5 Hz stimulation, despite the fact that the overexpression only increased [dATP] to 2% of the ATP pool [73]. Relaxation kinetics were also found to improve, with time to 50% relaxation halved in R1R2 overexpressed cells [73]. Interestingly, maximal and minimal [Ca^{2+}] were unaffected between the R1R2 and wild-type cells, but the Ca^{2+} transient decay occurred more quickly in the R1R2 cells indicating the potential for dATP to affect Ca^{2+}-handling ATPases [73]. Healthy transgenic mice overexpressing TgRR exhibited improved systolic function, and extracted cells from these mice were observed to display increased contraction ((maximal shortening increased by 21.5%, maximal rate of shortening increased by 15.4%)and relaxation , (rate of relaxation increased by 28.4%) [74]. This study found no major differences in Ca^{2+} transient of the trangenic cardiomyocytes and demonstrated that long-term treatment (5 months) can sustain enhanced function without major side effects in mice [74]. R1R2 overexpressing human pluripotent stem cell-derived cardiomyocytes (hPSC-CMs) were cocultured with wild-type cells in order to test the ability for dATP to affect untreated cells near a treatment region [75]. Wild-type cells were found to exhibit identical contractile behaviors to R1R2 overexpressed cells, indicating that dATP can freely diffuse through gap junctions and affect nearby cells due to its small size even if the drug is not delivered to every cell in the treatment region [75].

Adeno-associated viral (AAV) vector transfection has been explored as a treatment option to deliver R1R2 to cardiac cells [76]. An AAV vector was designed to overexpress R1R2 with a cardiac troponin T promoter in order to localize expression to the heart [77]. The vector was administered to healthy mice as well as infarcted rats, which resulted in increases to fractional shortening without alterations in heart rate [77]. Post-MI investigations on rat tissue indicated that treated rats recover fractional shortening and resemble sham hearts within an 8 week time period [77]. Large animal studies have also been performed to test AAV-mediated

dATP gene therapy. A study of 17 Yucatan minipigs began with induced myocardial infarction (MI) followed by coronary infusion of the R1R2 AAV vector BB-12 [78]. Treated pigs showed improved +dP/dt and -dP/dt 56 days after treatment indicating enhanced systolic and diastolic function compared to the untreated group, as well as improved left ventricular ejection fraction (LVEF) [78].

Recently, computational molecular modeling has been employed to determine specific biophysical mechanisms of dATP on the sarcomere. A 50 ns MD study was performed on myosin S1, testing the differences between ADP-Mg^{2+}- and dADP-Mg^{2+}-bound myosin. dADP was found to orient differently within the nucleotide binding pocket, demonstrating altered contacts with key nucleotide binding residues such as PHE 129 and overall maintaining less contacts with the protein [79]. These effects cascaded through the protein to the actin binding surface, allowing more positive residues to be exposed to the solvent, which likely increases electrostatic affinity for the negatively-charged actin thin filament [79]. This study provided atomic level detail regarding the effects of dADP on myosin S1.

dATP has shown promise as a therapeutic in mice, rats, dogs, minipig, and human studies. The small molecule has been seen as an effective method for recovering cardiac mechanical function in DCM patients as well as MI. However, the mechanisms of dATP on contractile proteins in the cardiomyocyte, as well as effects on Ca^{2+}-handling ATPases, are incompletely understood. Multiscale modeling can be an effective tool toward answering biophysical euqations about the differences between ATP and dATP in their interactions with cardiac tissue. The potential of scaling from atomic to molecular, subcellular, and cellular biophysics to add detail without extending beyond the bounds of computational feasibility also comes with a variety of challenges which we outline below.

0.4 Modeling approaches and bridging the gaps - a DCM case study

0.4.1 Effects of DCM mutants in regulatory thin filament proteins cTn and Tm

Mutations in regulatory thin filament sarcomeric proteins Tn and α-Tm have been associated with DCM (Figure 1). A clinical study of idiopathic DCM patients found mutations in the Tn complex in 7% of patients, with severe prognosis for patients with mutations in cTnC [5, 4]. cTnC D75Y/E59D missense mutation was detected in an adult male who suffered sudden cardiac death as a result of idiopathic DCM [22]. D75Y and E59D are point mutations located in the low affinity Ca^{2+} binding site on cTnC near the N-terminus. Studies in skinned and intact cardiomyocytes have reported a marked decrease in calcium sensitivity, cell shortening and force production for the double mutant (D75Y/E59D) and D75Y alone in spite of the fact that the mutations do not influence the intracellular calcium homeostasis [22, 23]. However, both D75Y and E59D are required to reduce the actomyosin ATPase activity and maximal force in muscle fibers, indicating that E59D enhances the effects of D75Y [23]. In addition to D75Y and E59D, the G159D cTnC mutation has been found in human DCM patients and has been shown to impair cTnC-cTnI interaction and decrease Ca^{2+} binding affinity [9, 25, 29, 80]. G159D cTnC mutant exhibits reduced opening and closing rates of N-terminus of cTnC post-calcium binding and dissociating respectively [81]. Additionally, G159D cTnC mutant abolishes the accelerated closing rate of the N-terminus of cTnC triggered by PKA mediated phosphorylation of cTnI [81]. Four rare clinical variates (Y5H, M103I, D145E, and I148V) of TnnC1 have been reported in association with DCM [82], of which Y5H cTnC mutation was reported in a pediatric patient with idiopathic DCM concomitant with a mutation in Myosin [83]. Three of these (Y5H, M103I, and I148V) showed decreased calcium sensitivity of myofilaments and impaired response of the myofilament to undergo Ca^{2+} desensitization upon PKA phosphorylation [84]. The fourth variant D145E presented with a MyBP-C rare

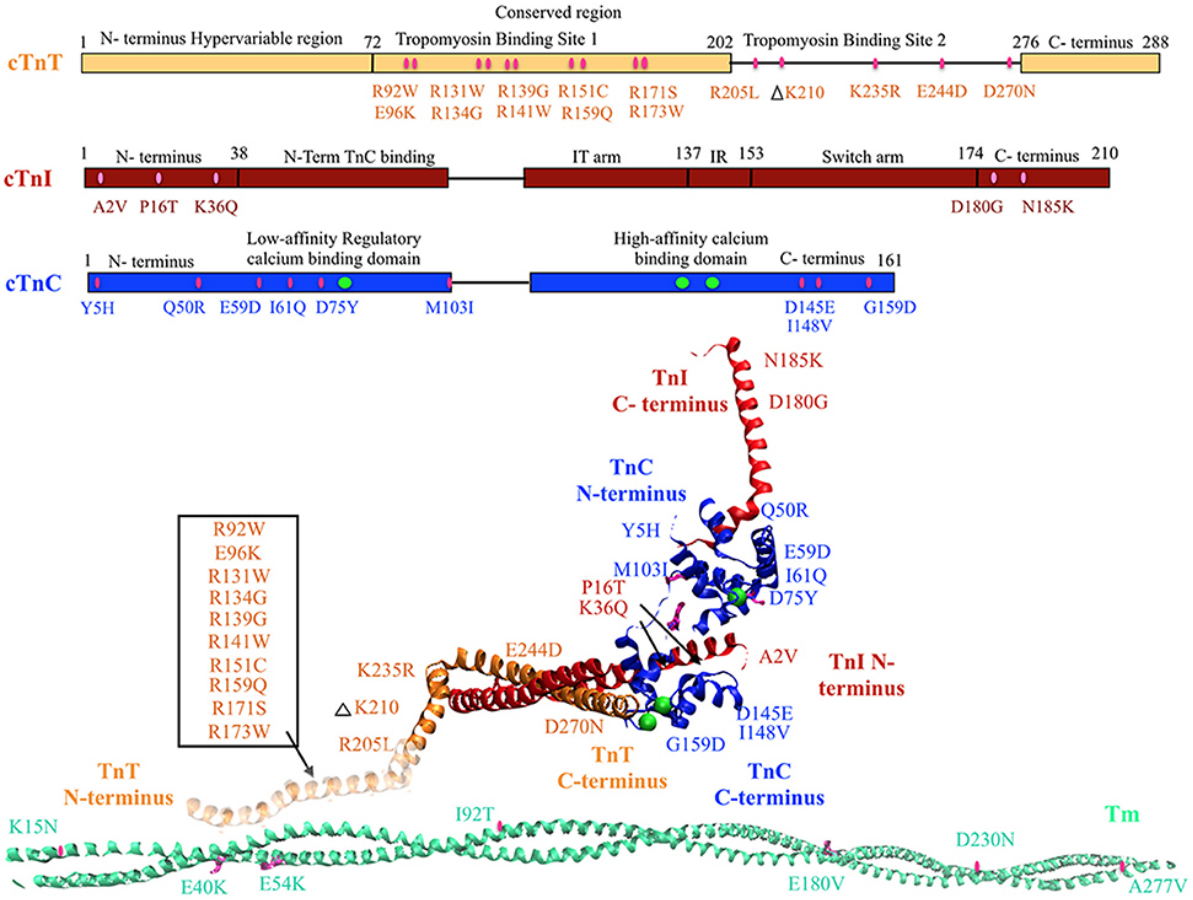

Figure 1. DCM associated mutations shown in regulatory thin filament proteins cTn and Tm. DCM mutations for cTn are shown in the cartoon representing primary amino acid sequence of cTnC, cTnI, and cTnT and in the cTnC crystal structure of the 52 kDa domain of human cTn (PDB: 1J1E) in the calcium saturated form (cTnC in blue, cTnI in red, cTnT in orange, calcium in green, mutations in pink). Residues 1-182 are missing in the crystal structure of cTnTthe mutations in that region have been enclosed within an open box and point to a cartoon rendering of residues 1-182 of cTnT (faded orange ribbon structure juxtaposing Tm). DCM mutations in Tm are shown in crystal structure for Tm (PDB: 1C1G) (Tm in teal, mutations in pink).

variant. Given that D145E mutation shows increased calcium sensitivity and is associated with HCM, it is quite plausible that the concomitantly present MyBP-C mutation mediated the observed DCM response [85, 84]. Additionally, cTnC mutant Q50R has been identified in a DCM family with a member with the rare disease of peripartum dilated cardiomyopathy [86].

A DCM associated mutation in cTnI, A2V, was found to hinder cTnC-cTnI interaction

via mammalian two-hybrid luciferase assay [10]. Two other cTnI mutants, K36Q and N185K, were reported in 2009 and found to decrease calcium sensitivity of actin-myosin S1 ATPase, maximal ATPase activity and reduce calcium binding affinity of cTnC [87, 4]. Two more cTnI mutants P16T and D180G were reported recently [88, 83].

An earlier study employing two-hybrid assays to investigate cTnT mutations R131W, R205L, and D270N, all of which have been found in human DCM patients, impaired cTnC-cTnI/cTnC-cTnT interaction [9]. A contractility study in rabbit muscle fibers reported that these mutations and TnT R141W decrease Ca^{2+} sensitivity of force generation, maximal ATPase activity and myofilament sliding speed [21]. Additionally, Robinson et al. reported a decrease in calcium sensitivity of these cTnT mutants as well, with the exception of cTnT mutation D270N. D270N cTnT led to a decrease cooperativity of Ca^{2+} binding but not overall Ca^{2+} affinity of cTn as measured by pCa50 in reconstituted thin filaments [29]. The ΔK210 cTnT mutation has been shown to decrease Ca^{2+} sensitivity of force generation and hinder cTnT-cTnI interaction without affecting maximum force generation [19, 9, 18, 29]. There are conflicting reports on the effect of ΔK210 on cooperativity of force generation [89, 18, 29]. Four missense mutations, R134G, R151C, R159Q, and R205W, in cTnT were identified in probands with familial DCM [90], of which two (R134G, and R205W) were also reported in pediatric patients with familial DCM [83]. Functional analysis of these mutations in reconstituted myocytes showed decreased calcium sensitivity of force development [90]. Additionally, a HCM associated mutant E244D, was identified in a DCM associated proband [90] and in a pediatric patient with familial DCM [83]. Further, a cTnT mutation R139H showed decreased calcium sensitivity and was reported in late onset DCM in a 70 year old woman (Morales et al., 2010). This is interesting as usually cTnT mutations are associated with early onset and aggressive form of DCM. Lastly, E96K cTnT mutation was reported in a 5 month patient with idiopathic DCM [83].

Tm mutations E40K and E54K were identified in a Genome-Wide Association Study (GWAS), and when reconstituted in rabbit muscle fibers were found to decrease Ca^{2+} sensitivity

[8, 21]. Interestingly, the E40K mutation was found to decrease myofilament sliding speed while the E54K mutation had no effect on sliding speed [21]. Both mutations caused localized destabilization of the Tm dimers and affect interactions with actin which would then directly affect ATPase activity [91]. In addition, D230N Tm mutation showed decreased calcium sensitivity of myofilaments, and dissociation between calcium sensitivity and PKA mediated beta adrenergic response to TnI phosphorylation [11, 24]. Lastly, multiple Tm mutations (K15N, I92T, A277V) have been reported in pediatric cases with idiopathic or familial DCM [83].

The above-mentioned familial mutations in the regulatory proteins cTn and α-Tm, that have been identified in human patients over the course of years, display some wide-ranging molecular effects that mainly converge to few cellular mechanisms such as altered calcium sensitivity and decreased ATPase activity ultimately leading to depressed contractile force observed in DCM. A recent innovative motility assay study proposed that the varying experimental findings of DCM-associated thin filament mutations in α-Tm and cTn can be explained by a decoupling of Ca^{2+} sensitivity from cTnI phosphorylation by PKA [24]. This finding, along with the wide variety of mutations in thin filament proteins that have been connected to the development of DCM, underscores the urgency of studying the complicated cascade of contraction events as a whole in order to create a cohesive picture of DCM causes and progression. Genetically engineered animal models provide an opportunity to understand the sequelae of molecular and cellular events as they translate to the whole heart level. Notably, genetically engineered mice with sarcomeric mutations ΔK210 [18, 36] and R141W [37] in cTnT have been generated. These studies showed a gene-dosage effect on the cardiac phenotype and recapitulated the human phenotype. Despite the key genotype-to-phenotype insights gleaned from animal model studies, most experimental studies have so far been conducted in reconstituted in vitro systems. Majority of experimental studies have measured the effects of thin filament protein mutations on cell-level function, but have not looked more

closely into molecular mechanisms or expression of dysfunction on the whole heart level. Multi-scale computational modeling offers a complementary set of tools that can help us understand the spatial and temporal transition to clinical DCM.

0.4.2 Molecular modeling of regulatory thin filament protein mutations

Structural determination from x-ray crystallography and NMR studies has helped provide key insights into molecular basis of cTnC function [92]. Previously published experimental and theoretical studies have used these structural data to probe rapid, nanosecond and microsecond timescale conformational dynamics, by using Brownian Dynamics (BD) and Molecular Dynamics (MD) simulations, that are correlated with calcium binding [93, 27]. MD and BD simulations are useful *in-silico* approaches that have been employed to understand the molecular basis of altered structural and functional dynamics of regulatory myofilament proteins such as cTnC in varied states. For example, Varughese and Li investigated, with MD, changes in the structural dynamics of cardiac Tn, including TnC, upon binding bepridil, a known inotropic agent [38, 39] combined long time-scale MD simulations and BD simulations to understand the dynamics of wild-type TnC in its calcium-free, calcium-bound, and TnI-bound states, as well as V44Q [94].

Intra-molecular dynamic changes in cTn can cause alterations in: (a) the calcium binding affinity of cTnC; (b) the rate of calcium dissociation from cTnC; (c) the forward rate of cTnC conformation transition; (d) the reverse rate of cTnC conformation transition; and (e) the structure of cTnC such that there are differences in charge within the exposed hydrophobic patch [43]. Additionally, cTn mutations can affect interactions between cTnC, cTnI, and cTnT as well as downstream contractile proteins such as Tm and actin [9, 29]. A recent *in silico* study [43] employed MD and BD simulations to postulate the decreased calcium binding affinity of cTnC and the altered rate of hydrophobic patch opening within cTnC as the molecular basis of the reported changes in calcium sensitivity and force production in the D75Y cTnC DCM

mutant. An MD study on residues 70-110 of cTnT found that familial HCM -linked mutations R92L and R92W, located near the Tm binding domain, lead to increased hinge movement downstream on the cTnT molecule as well as decreased helical stability [95]. Importantly, the study found that divergent phenotypes emerge in a live mouse model of these mutations, which demonstrates a limitation to modeling isolated proteins [95].

MD simulations have the potential to uncover biophysical effects of DCM associated mutations in cardiac Tm. Recent MD studies have explored the properties of Tm in healthy cases as well as patho-physiological cases, noting that Tm stiffness may impact downstream contractility events greatly [96, 97, 98, 99]. A 2012 study used MD to study familial HCM associated Tm mutations D175N and E180G and found that both mutations lead to increased flexibility of Tm and therefore, decreased persistence length of the molecule [100]. Another MD study has also been performed on HCM Tm mutations E62Q, A63V, K70T, V95A, D175N, E180G, L185R, E192K in order to explore the effects of point mutations on Tm flexibility and Tm-actin interactions [101]. In the case of DCM, a time-independent electrostatic snapshot of the DCM associated Tm mutation showed that E54K and E40K mutations alter the surface charge of Tm, which may affect Tm-actin interaction [8, 91]. A time-dependent MD study was also performed on the E54K Tm mutant in combination with 7 actin monomers and showed that this mutation causes increased stiffness and decreased curvature in the Tm molecule overall while stabilizing and destabilizing the coiled coil structure in different regions of the molecule and greatly weakening Tm-actin binding [101]. More MD studies are needed in the area of Tm DCM mutations in order to visualize effects of other mutations, such as E40K, that may affect Tm-actin and Tm-cTn interactions.

In-silico investigation of sarcomere protein structure-function dynamics by MD and BD simulations provides key insights toward understanding molecular effects of genetic mutations and post-translational modifications [40, 43]. However, these structure-function dynamics can change significantly when myofilament proteins interact with one another in an integrated

physiological system. It has been reported that kinetic rates of a given state transition vary in isolated molecular states and integrated myofilament states [102]. This was well demonstrated in a previous study where the off-rates of calcium binding were studied in depth from isolated cTnC molecule to a structurally integrated myofilament preparation [102]. The whole cTn complex has been modeled using MD, both with and without Ca^{2+} bound [103, 104]. A 2014 study proved the value of modeling the complex as a whole, because removing Ca^{2+} from the regulatory binding pocket on cTnC affected cTnC hydrophobic patch opening as well as the folding and flexibility of the cTnI switch region [104]. Moving further up in scale, an integrated MD study of a whole thin filament including cTn, 14 actin monomers, and two overlapping Tm molecules illustrates the importance of modeling inter-protein interactions along the thin filament [105]. The MD simulation performed was only 1 ns in length, but was able to accurately capture the rotation of the I-T arm in the Tn complex as a direct consequence of Ca^{2+} binding [105]. The model was used to study cTnT mutations R92W and R92L associated with familial HCM and found that both mutations decrease bending forces in the hinge region of cTnT which affects Tm interaction, a downstream effect that may not have been captured if the study were performed on isolated cTnT [106].

Integration of molecular level state-transition kinetic data into the sarcomere level is a key challenge yet to be solved for using *in-silico* methods. At the molecular level it takes about 510 s for calcium to bind to cTnC [94, 39]. With state-of-the-art supercomputers we are now able to simulate molecular events such as calcium-binding events and conformational state-transitions within cTnC (a relatively small protein18 kDa), events that occur in the microseconds range. At the myofilament level it takes about 700 ms for a contraction-relaxation cycle to take place in a sarcomere [107, 51]. Recording the kinetics of all inter-molecular and intra-molecular state transitions for every myofilament protein during one contraction-relaxation cycle in a sarcomere is a tremendous task, as illustrated by the 1 ns upper limit of an MD simulation incorporating the full thin filament [105]. This is due to the enormous computational

power and speed that would be needed to solve for longer time scale simulations and bulky proteins, such as Titin (3.9 MDa), Myosin (220 kDa), and Tropomyosin (37 kDa), that form the backbone of the sarcomeric thin and thick myofilament protein complexes. Nevertheless, key insights into molecular behavior of bulky proteins like Titin that are commonly known to be mutated in DCM have been achieved by MD simulations [108]. An earlier MD study of Titin wherein single Ig domains of Titin were stretched reported sequential unfolding of Ig domains corroborating experiments [109, 110, 111]. A recent study of Titin examined the hydrophobic core region of the protein associated with a DCM mutation V54M and reported destabilization of transition from bend to coil in secondary structure of Titin and reduced affinity to Z-disc protein T-cap/telethonin [112]. Given that Titin mutations are commonly associated with DCM, molecular modeling of Titin domains associated with DCM is mandated. While we have much to gain from MD simulation studies, gaps in our experimental knowledge toward understanding dynamics of molecular level interactions and kinetics of state transitions between thick and thin myofilament proteins compound the challenges in standardizing conditions and validating results from the molecular simulation studies.

0.4.3 *In-silico* translation of molecular level changes to thin filament mechanics

The mathematical formulation of cardiac myofilament models that explicitly incorporate spatio-temporal acto-myosin interactions and stochastic XB formation to compute contractile force have lagged behind electrophysiological models of the heart [41, 50]. This is largely due to the (a) paucity of kinetic data on thick-thin myofilament interactions and molecular state-transitions, (b) requirement of partial-differential equations (PDEs) to solve for explicit spatio-temporal acto-myosin interactions, (c) lack of complete understanding of translation of steady-state contractile force into a length and load-dependent dynamic contractile force response via XB cycling, (d) difficulty in solving for computationally expensive stochastic interactions, (e) partial understanding of cooperative mechanisms involved in myofilament

activation, and (f) technical gaps in our knowledge due to species differences and varied experimental conditions in scientific studies. Nonetheless, ordinary differential equation (ODE) and Monte Carlo Markov models of regulated co-operative myofilament activation with nearest neighbor interactions, wherein some molecular states are lumped together empirically and model parameters are optimized such that the best-fit of the base model to the experimentally measured steady-state force-calcium data-sets is achieved, have been formulated [113, 114, 45, 115, 41, 44, 42, 116, 117]. These relatively simplified mean-field Markov models of cooperative myofilament activation and contraction have helped provide deeper insights as to how changes in inter-molecular and intra-molecular interactions in myofilament proteins can alter steady-state myofilament properties (myofilament calcium sensitivity and cooperativity of myofilament activation) and function (maximal force generation), which can then translate to cardiac pump dysfunction as reported in DCM.

Arguably the most logical type of sarcomere-level model to begin with, when testing the effects of point mutations on thin filament proteins, is a Markov model of thin filament activation. One such model, originally developed in 2010 and since expanded for a variety of applications, consists of 26 spatially explicit regulatory units (RUs), each RU including 7 actin monomers, one Tm molecule, and cTn [42]. The model captures cooperativity of thin filament activation by relying on the Tm position (blocked, closed, or open) of each RU's nearest neighbor in order to determine rates governing state transitions. Using this model as a starting point, further studies have been able to test a variety of contractility protein mutations at a larger spatial and temporal scale than MD simulation can reasonably accomplish. A relevant example is a recent study that simulated Tm mutations E180G and D175N, which have been found in HCM patients, using a Monte Carlo framework extension of the Campbell model [117]. MD simulations indicated that both Tm mutation increase Tm flexibility while lowering persistence length of the molecule [100]. The thin filament model was able to simulate experimentally gathered wildtype and mutant contraction data by altering Tm persistence length, transition

rates between the blocked and closed Tm states, and percentage of the XB cycle spent in the attached force-producing state [117]. MD simulation data of isolated Tm can offer information on persistence length but not on Tm-actin interaction or XB cycling, which were discovered to be possible downstream effects of these mutations.

A previously published multi-scale modeling study from our group was one of the first studies to directly incorporate the molecular changes computed from BD and MD simulations, in the DCM mutant D75Y cTnC, into a six-state Markov model of steady-state myofilament contraction (Figure 2) [43]. The key results from the study reported that the intra-molecular changes (decreased calcium binding affinity of cTnC and depressed rate of hydrophobic patch opening during cTnC conformational change) in D75Y cTnC mutant are sufficient to explain the observed decrease in myofilament calcium sensitivity under steady-state experimental conditions in skinned cardiomyocytes. Additionally, the study highlighted how DCM mutants like E59D cTnC which appear to have healthy myofilament response in skinned myofilament experiments, can in fact be harboring molecular modifications which can potentially turn deleterious under stressful conditions for the myocardium. A weakness of this study was that they did not model the effects of the double mutant D75Y/E59D. This would have been more appropriate as both mutations, D75Y, and E59D are needed for a reduction in maximum myofibrillar ATPase and maximum force of contraction in skinned fibers. Additionally, The D75Y mutant is important for the effect seen in calcium binding affinity, however the cellular phenotype may not be explained solely by a single mutation based on the in vitro data. This study was instrumental in its scope, as it bridged the genotypic defects at sarcomeric protein level to myofilament phenotype *in silico*, by directly incorporating molecular parameters from BD and MD simulations into appropriate markov states of cTnC activation. The study again displays the numerous challenges for the mathematical modeler in scaling from molecular level to myofilament levels to compute steady-state contractile force, as MD data was insufficient to fully capture cellular mutant contractility changes which may be due to cTnC-cTnI interaction

or other protein interactions in the sarcomere as shown in case of G159D cTnC mutant. It is important to note that prediction of steady-state force-calcium data is not predictive of cellular phenotype by itself. For example, a reduction in calcium sensitivity of myofilaments can be compensated for by an increase in calcium transient. In such a case there will be no apparent change in contractile function at the cellular level. Similarly, an increase in calcium sensitivity of myofilaments can be offset by defects in mechano-sensing. In fact these compensatory changes are integral to the process of cardiac remodeling leading to DCM. Further, as is evident in many DCM mutants (see Table Table1),1), change in calcium sensitivity is not the only predisposing factor in DCM and the acto-myosin ATPase activity should also be modeled in. Therefore, it is important to factor in the contractile phenotype from an intact cell and incorporate dynamic coupling in a model between thin-thick myofilaments, passive tension, calcium homeostasis, and mechano-transduction, at the least to be considered a cellular level model.

Given the gaps in our knowledge of kinetic rates during molecular transitions and variations in experimental data collated from numerous studies, the mathematical modeler is required to carefully choose explicit Markov states within an appropriate framework, and to standardize technical variates of species, temperature, and molecular state in order to glean meaningful insights from any multi-scale computational study. It is known that various rodent species (mouse, rat, guinea pig) express variable isoforms of key myofilament proteins under normal conditions, for e.g., mouse and rat express α-myosin heavy chain (MHC) isoform [118], whereas, guinea pigs express β-MHC under basal conditions [119]. Given that α-MHC is at least three times faster than β-MHC, this difference in basal conditions in rodents is sufficient to alter the rate of XB cycling significantly [118]. Isoform switches in myofilament proteins are known to occur in patho-physiological conditions as well [120]. Similar changes in protein isoform expression and kinetics have been reported for other myofilament proteins [121]. These changes impact the myofilament properties of calcium sensitivity, cooperativity and maximal

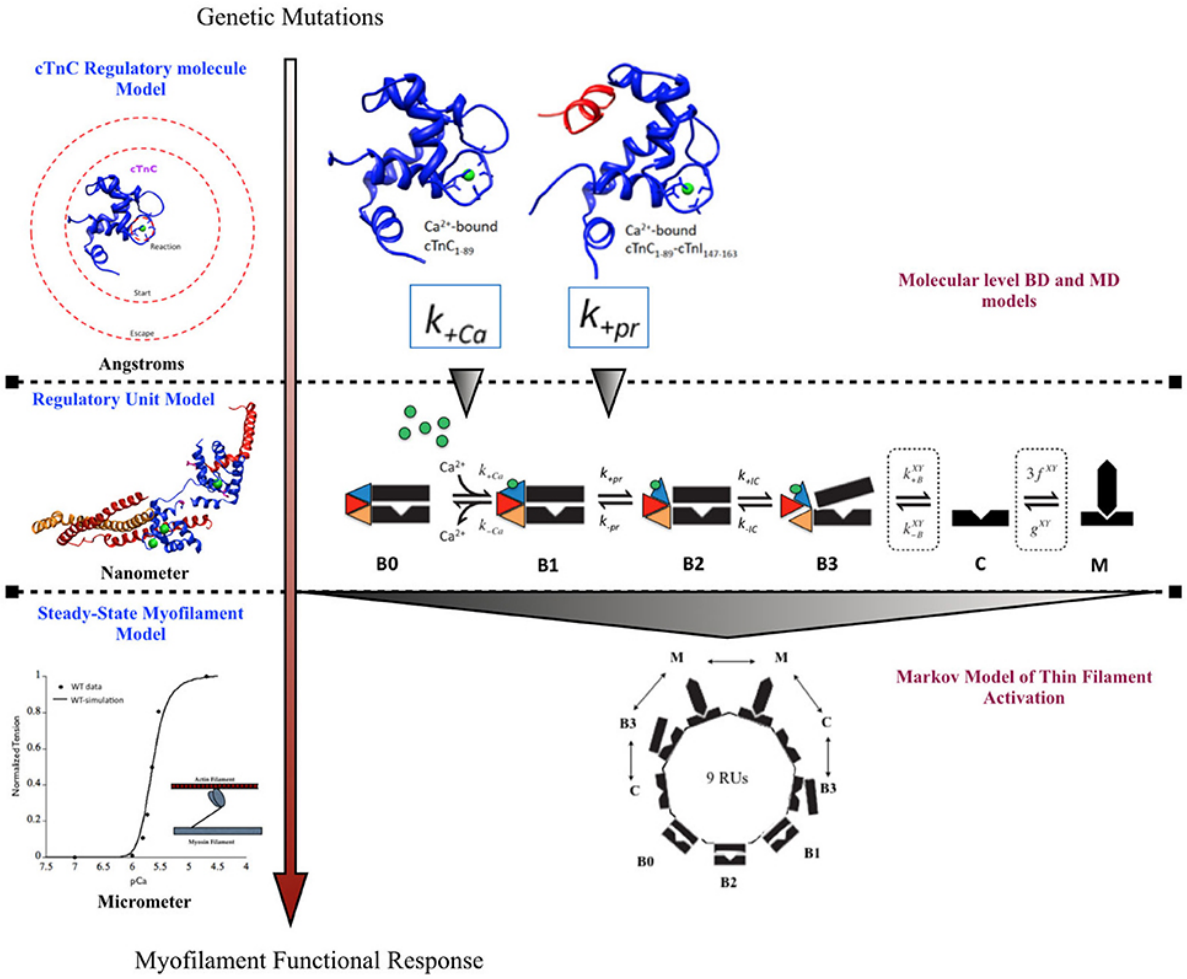

Figure 2. Schematic showing incorporation of molecular data of cTnC activation obtained from BD and MD simulations into a six-state Markov model of myofilament activation at steady-state conditions, as an example of bridging molecular to cellular scales in a modeling study by Dewan et al. [43]

force output significantly. Additionally, increased temperature is known to have a significant effect on increasing calcium sensitivity of myofilaments and increasing the maximal developed contractile force under steady-state conditions in intact and skinned ventricular tissue/cells from various species [122, 123, 124]. This is likely due to alterations in molecular kinetics of state transitions of myofilament proteins with temperature. Also, kinetics of state-transitions can vary significantly in isolated molecular states vs. integrated systems, as elucidated in an earlier study where the off-rates of calcium binding were studied in depth from isolated cTnC

molecule to a structurally integrated myofilament preparation [102]. These biophysical variates must be accounted for during longitudinal scaling from molecular states to myofilament states, as failing to do so can potentially exaggerate or mask the magnitude of, and can even potentially alter the direction of, steady-state myofilament properties as reported for a mutation. It is imperative to note that this is not always possible due to paucity of experimental data, still, careful consideration must be given to these variates in order to arrive at meaningful analysis from *in-silico* studies and to achieve good quantitative agreement with experimental data.

0.4.4 Scaling from thin filament mechanics to thick filament mechanics

Results of Markov models of cooperative myofilament activation with nearest neighbor interactions just described suggest that a meaningful prediction toward patho-physiological outcome of genetic mutations is possible *in-silico* [43, 117]. While this, of course, does not mean that the models are entirely correct in their predictions, as the whole system is not explicitly represented; it does suggest that the key myofilament properties are adequately represented to recapitulate fairly complex phenomena. These Markov models adequately describe the process of thin filament activation, such that the myofilament contractile response is mediated by a prescribed length-clamp and/or calcium-clamp at any given point of time. However, under physiological conditions, myofilament activation and XB cycling are temporally modulated by cyclical variation in length, calcium, and loading conditions during a contraction-relaxation cycle [125]. Modeling thick-thin myofilament effects into a dynamic model of contraction, wherein length-dependence and load-dependence of the myofilaments have been incorporated, will allow us to further gain quantitative insights in the shortening response of the contractile machinery and the work done by myofilaments. This is imperative to scaling the effects of the identified DCM mutant from genotype to phenotype.

The length-dependence of myofilament activation and the load-dependence of the rate of myofilament shortening, are tightly regulated and complex properties of the healthy

myocardium that are highly dependent on the spatio-temporal arrangement of the myofilaments. In a simplistic view of our understanding of cardiac biomechanics, length dependence of myofilament activation is modulated by the degree of overlap between thick and thin filaments and calcium sensitivity of myofilaments [53, 54, 126, 57]. On the other hand, load-dependence of rate of myofilament shortening is modulated by number of XBs in the strongly bound state, distance between the thick and thin filaments, myosin isoform, degree of thick-thin filament cooperativity, rate of XB cycling, and stiffness of XBs [127, 128, 129, 130, 131, 132]. Ultimately, the twitch dynamics of the myofilaments are the key determinants of the cardiac pump output during various phases of the cardiac cycle [133]. In reality, we are yet to fully comprehend the molecular basis of these dynamic emergent myofilament properties and their modulators. An explicit PDE model that simulates the myofilament contraction-relaxation cycle while recapitulating length-dependent myofilament activation and force-velocity relationships is yet to be described to the best of our knowledge. However, phenomenological models based on empirical relationships have been described to quantitatively recapitulate these myofilament properties [128, 134, 107]. Phenomenological vs. explicit Huxley-type muscle models of XB cycling have been discussed before [135].

Computational models of XB cycling dynamics are key toward scaling-up and integrating length dependence and dynamic muscle activation into studies of thin filament DCM proteins. For example, the Rice ODE model of XB cycling accurately mimics length dependence of active/passive forces and Ca^{2+} binding, while simplifying a complex myofilament geometry by keeping track of the overlap fraction between thick and thin filaments [45]. This model has been expanded in more recent studies to include more complex geometries and metabolic intermediates, and has been incorporated into organ-scale finite element models through solving the sarcomere model at different points in a finite element mesh [136, 137, 138, 139]. Although the model traditionally calculates force from a half sarcomere and extrapolates to cell-level force values, it may be possible to explicitly model a full cell with 32 sarcomeres using a

Blue Gene supercomputer in order to capture cooperativity of the whole cell [44]. Another XB modeling approach more explicitly models the sarcomere geometry by including 3 half thick filaments surrounded hexagonally by 13 half thin filaments, mathematically modeled by a 3D spring array using finite element analysis and governed by Monte Carlo processes [140]. This model importantly includes filament compliance in its calculations, creating a more biophysically accurate window into the individual proteins making up the myofilament. The Chase model has been used to study specific familial HCM-associated cTnI mutations by converting experimentally gathered Ca^{2+} transient information into altered probability of XB activation [141]. However, this study assumes that altered Ca^{2+} binding kinetics are the sole contributor to altered contractility without considering the interaction of mutated cTnI with other thin filament proteins. When searching for XB models that will be able to accurately model DCM sarcomere mutations, mechanistic models are more promising as they allow for direct input of protein-level changes into a larger scale model.

Phenomenological computational models of twitch tension, which do not explicitly translate the molecular behavior of myofilament proteins to the myofilament properties, can still provide invaluable insight in the workings of the myocardium. Therefore, it is critical to underscore the key considerations and challenges to take into account when formulating dynamic models of cardiac twitch. Temperature dependence of myofilament dynamics, loading conditions (preload and afterload), frequency of electrical pacing which determines the calcium load, and biological species, are biophysical experimental variates that significantly alter twitch dynamics [142]. Previous studies have reported frequency and temperature dependent changes in contraction-relaxation dynamics and maximal twitch force, based on phase-plane analysis of dynamic force-calcium relationships from intact rat myocardium [131]. Briefly, increasing frequency of stimulation resulted in a increased developed force, enhanced myofilament responsiveness to calcium and abbreviated twitch duration; increasing temperature from (22 to 37°C), while maintaining stimulation frequency and preload, resulted in biphasic effects

- between 22 and 3°C, developed force did not decrease despite abbreviated twitch duration; between 30 and 37°C, a steep decline in developed twitch force was observed. This would suggest independent temperature dependence on myofilament activation and relaxation kinetics. An earlier study elegantly measured the relationship between cardiac work output and external load in single rat cardiomyocytes [143]. They reported work output of cardiomyocytes under a range of loading conditions ranging from isometric, unloaded and physiologically loaded conditions. Alterations in loading conditions affect XB cycling rates and force-velocity relations. Factoring in the effect of loading conditions, imposed on the myocyte during experimental study from which parameters are being collated, is crucial to correct interpretation of modeling results and for scaling the results to the organ level. Lastly, different experimental studies report data from different biological species, each of which expresses different myofilament protein isoforms that can independently alter twitch dynamics [144, 51]. It is important that careful consideration be given to these variables as models are parameterized.

0.4.5 Summary and perspectives

An important aspect that requires careful consideration and work in modeling studies is coupling of calcium homeostasis and mechano-transduction mechanisms to myofilament mechanics. Sarcomere generated force cannot predict the organ level phenotype in entirety if upstream and downstream regulatory mechanisms in the cell are not coupled to it. In order to comprehensively translate to the cellular scale, coupling of models of active tension to models of (a) passive tension mediated by Titin, (b) upstream calcium homeostasis mechanisms mediating CICR, (c) cytoskeletal proteins and z-disc proteins that sense and transmit force signals, (d) ATP, ROS and energy regulation by mitochondria, (e) insulin signaling, (f) beta-adrenergic signaling pathways, and (g) signaling networks mediating nuclear transcription response toward sarcomere addition should be considered. However, with added complexity in models the degree of ambiguity in results also increases which may prove futile. It is

important to note that DCM is a disease characterized by an organ level phenotype, so in order to understand the complex cascade that can cause a point mutation in a contractile protein to lead to growth and remodeling of the heart as a whole it is necessary to scale current molecular and cellular level models to finite element models of the heart with realistic geometries. For more information on whole heart modeling and its potential, detailed reviews and modeling frameworks exist [47, 48, 138, 50]. Of note is the recent study reporting phenomenological modeling of the tension integral of the cardiomyocyte twitch as the predictor for DCM and HCM phenotype in cardiomyopathies [30]. Furthermore, given that familial DCM manifests clinically over-time it is pertinent to simulate pathological cardiac remodeling leading to DCM. Growth modeling frameworks utilizing stress or strain as the growth stimulus for sarcomere addition at the whole-heart level coupled with cardiac mechanics have been recently reviewed and present with a promising avenue to scale-up [46, 49]. In addition, mechanistic frameworks for modeling biochemical signaling networks that have previously been formulated [145], such as for PKA mediated beta-adrenergic signaling [146], will be useful tools as cardiac signaling in DCM is being studied based on RNAseq and phosphoprotemics [35, 147]. Formulating explicit models of molecular behavior and scaling them longitudinally to cellular levels is an extremely challenging task and perhaps not without its own pitfalls. Nonetheless, *in-silico* modeling of cardiac biomechanics, in parallel with the experimental studies, is a powerful set of tools that can be applied toward integrative and quantitative understanding of DCM.

0.5 Conclusion

This dissertation is focused toward demonstrating the feasibility and applicability of multiscale modeling to gain mechanistic insights into role of known genetic DCM mutations in contractile proteins, as well as the potential for dATP to treat contractile cardiac defects (Figure 3). We discuss some of the insights that can be gained from computational models of cardiac biomechanics when scaling from the molecular to cellular level. We have so far described the

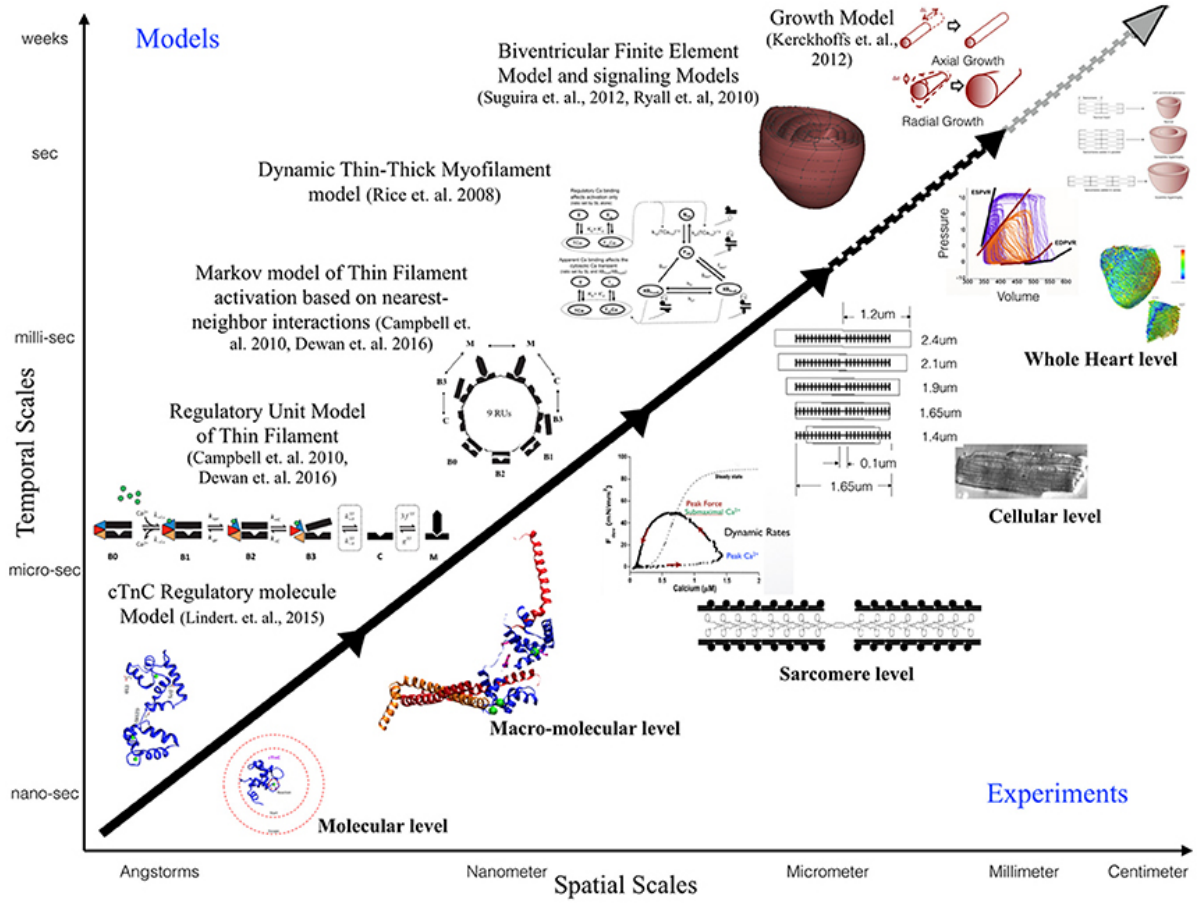

Figure 3. Schematic illustrating the scope of multi-scale modeling techniques, panning spatial and temporal scales, to complement experimental data at all biological scales. Representative examples of modeling frameworks from molecular to cellular (solid black arrow-focus of this review) to whole heart level (dotted black arrow) and growth modeling (dotted gray arrow) are shown.

considerations and challenges that must to be accounted for when computationally modeling the mechanical effects of sarcomeric mutations of DCM from genotype to cellular phenotype. In particular, we discussed the difficulties in standardizing parameters for a multi-scale modeling study from varied experimental data sets. We have also provided an introduction to cellular mechanisms of force production, and a review of previous experimental and computational studies of dATP treatment.

We will next apply computational modeling techniques across scales in an effort to answer two major questions about cardiac health: (1) How can disparate genetic mutations lead

to similar disease phenotypes in DCM patients? and (2) How does dATP act on contractile and calcium handling proteins in order to augment cardiac function? Methods such as Molecular Dynamics (MD), Brownian dynamics (BD), electrostatic analysis, and Markov State Models (MSMs) of subcellular function are interwoven to minimize gaps in knowledge that may result from using one method independently. We investigate three DCM-associated genotypes - E59D, D75Y, and G159D - to determine how mutating one residue in troponin C can change the Ca^{2+} binding affinity and folding pattern of the protein, cascading upward to alter calcium sensitivity of cardiomyocytes and, eventually, present as DCM. BD and electrostatics analysis of tropomyosin (Tm)-actin interactions provide us with a realistic multi-well energy landscape of Tm as it moves about the thin filament, adding molecular detail to well-established theories of Tm movement which can be used to populate energy-based models of thin filament activation.

To investigate the second guiding question of the dissertation, we focus both on mechanical impacts of dATP and the effects of the drug on the calcium handling pump SERCA. Mechanically, we build on MD analysis of ADP- and dADP bound myosin S1 [79] to study the electrostatic impact of dATP treatment on myosin-actin affinity. Differential crossbridge affinity, combined with predicted changes to powerstroke rate and XB detachment, allow us to quantify the effects of dATP on all stages of the XB cycle and, in turn, cardiac force production. Our analysis also provides explanations for the noted fact that appreciable increases in force production develop even at low levels of dATP upregulation [69]. Gaussian accelerated MD of apo, MgATP-bound, and dATP-bound SERCA is employed to calculate low-energy structures of the protein in normal and drug-treated conditions. BD simulations explore differing association rates of ATP/dATP and Ca^{2+} ions to these structures, which can then be integrated into a cellular calcium-handling model to determine their impact on cellular relaxation. Taken together, these analyses of dATP treatment provide compelling evidence of molecular mechanisms behind the global impacts of dATP treatment on cardiomyocytes.

0.6 Acknowledgements

The Introduction contains excerpts of the material as it appears in: Dewan, S*, McCabe, KJ*, Regnier, M, McCulloch, AD (2017). ”Insights and Challenges of Multi-scale Modeling of Sarcomere Mechanics in cTn and Tm DCM mutants-Genotype to Cellular Phenotype”. Frontiers in Physiology, 8, p 151. The dissertation author was the co-first author of this review article.

Chapter 1

Molecular Effects of cTnC DCM Mutations on Calcium Sensitivity and Myofilament Activation: An Integrated Multi-scale Modeling Study

1.1 Abstract

Mutations in cardiac troponin C (D75Y, E59D, and G159D), a key regulatory protein of myofilament contraction, have been associated with dilated cardiomyopathy (DCM). Despite reports of altered myofilament function in these mutants, the underlying molecular alterations caused by these mutations remain elusive. Here we investigate *in silico* the intramolecular mechanisms by which these mutations affect myofilament contraction. On the basis of the location of cardiac troponin C (cTnC) mutations, we tested the hypothesis that intramolecular effects can explain the altered myofilament calcium sensitivity of force development for D75Y and E59D cTnC, whereas altered cardiac troponin Ctroponin I (cTnCcTnI) interaction contributes to the reported contractile effects of the G159D mutation. We employed a multiscale approach combining molecular dynamics (MD) and Brownian dynamics (BD) simulations to estimate cTnC calcium association and hydrophobic patch opening. We then integrated these parameters into a Markov model of myofilament activation to compute the steady-state forcepCa relationship. The analysis showed that myofilament calcium sensitivity with D75Y and E59D can be explained by changes in calcium binding affinity of cTnC and the rate of hydrophobic patch opening, if a partial cTnC interhelical opening angle (110 degrees) is sufficient for cTnI switch peptide association to cTnC. In contrast, interactions between cTnC and cTnI within the cardiac troponin complex must also be accounted for to explain contractile alterations due to G159D. In conclusion, this is the first multiscale *in silico* study to elucidate how direct molecular effects of genetic mutations in cTnC translate to altered myofilament contractile function.

1.2 Introduction

Dilated cardiomyopathy (DCM), a widely prevalent acquired cardiac muscle disease, is characterized by dilatation of the heart and impaired contractile function of the ventricles [3]. DCM is the most common reason for heart transplantation, occurring in approximately 58 people per 100,000 and causing approximately 10,000 deaths and 46,000 hospitalizations each year in the United States. It is estimated that 30-35% of DCM cases are linked to mutations in the genes encoding contractile proteins [148, 9], including titin, actin, myosin, tropomyosin, and all three subunits of cardiac troponin (cTn) [6]. By altering key myofilament properties such as calcium sensitivity of myofilaments, mutations in cTn may directly contribute to the development of DCM. A key motivation of this study is to understand how the intramolecular dynamics underlying known DCM mutations in the calcium binding domain of cTnC translate to altered myofilament contractile response. Cardiac troponin (cTn), a macromolecular protein in the thin filament complex of the sarcomere in cardiomyocytes, is a key regulator of contractile mechanics. Structurally, cTn consists of three subunits: troponin C (cTnC), troponin I (cTnI), and troponin T (cTnT) [149]. Binding of the signaling ion Ca^{2+} to the N-terminal regulatory domain of cTnC results in structural and dynamic changes that trigger contraction [150, 102]. As a consequence of calcium binding to the regulatory domain of cTnC, there is an increased exposure of hydrophobic residues on the surface of cTnC (between helices A and B). This precipitates stronger association with the switch peptide region of cTnI and reduced inhibitory peptide interaction of cTnI with actin, allowing increased tropomyosin mobility that allows strong myosin binding and contraction [150, 151]. Structurally, TnC is one of the best studied regulatory proteins in the sarcomere. Numerous structures of the TnC regulatory domain [152, 153, 154, 155] as well as the full-length, two-lobed molecule exist [156, 157]. The regulatory domain, a highly α-helical molecule that constitutes the first 89 N-terminal residues of the troponin C protein, consists of five α-helices (N, AD). Previous computational studies have addressed modeling many cTn-related processes on a molecular scale [93, 94, 39, 22, 38,

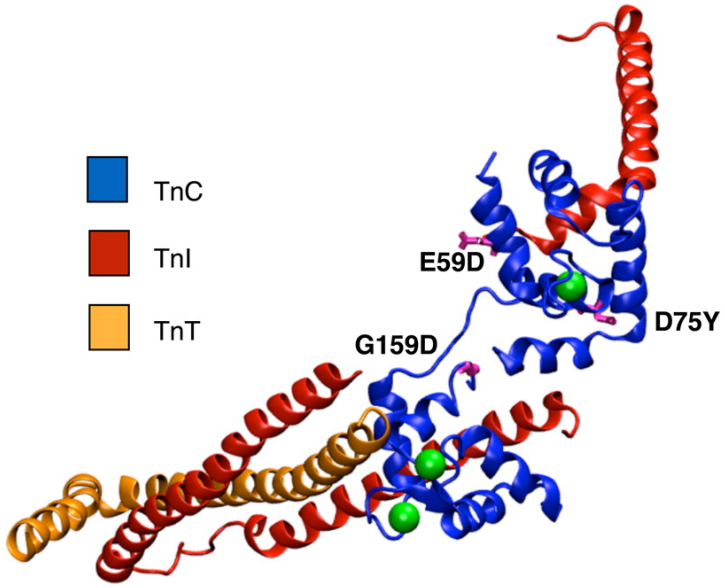

Figure 1.1. Crystal structure of cTn (cTnC in blue, cTnI in red, cTnT in orange, calcium in green) complex showing the location of the DCM mutations D75Y, E59D, and G159D (in pink).

158, 103, 159, 104]. At least three clinically observed mutations in cTnC have been proposed to be associated with DCM 1.1. Two of these mutations, D75Y and E59D, are located in or near the Ca^{2+}-binding site II in the regulatory domain of cTnC. Studies in skinned cardiomyocytes have reported a marked decrease in calcium sensitivity for the double mutant (D75Y/E59D) and D75Y alone, in spite of the fact that the mutations do not influence the intracellular calcium homeostasis [22, 23]. Interestingly, the E59D mutation alone was phenotypically comparable to wild-type cTnC in its effects on myofilament function [22, 23]. Another cTnC DCM mutation, G159D, is located in the C-terminus of cTnC, distal to site II, in close proximity to the I-T arm interaction region of cTnI and cTnC. Experimental reports for the G159D mutation have suggested contrasting phenotypes, with increased myofilament Ca^{2+} sensitivity in humans [148] and unaltered contractility in rats [25].

The molecular mechanisms by which these cTnC mutations cause contractile alterations remain unclear. Intramolecular dynamic changes in cTnC can cause alterations in (a) the calcium binding affinity of cTnC; (b) the rate of calcium dissociation from cTnC; (c) the

forward rate of cTnC conformation transition; (d) the reverse rate of cTnC conformation transition; and (e) the structure of cTnC such that there are differences in charge within the exposed hydrophobic patch. Additionally, cTnC mutations can affect its interactions with cTnI and downstream contractile proteins. D75Y and E59D are closer to the regulatory calcium binding site of cTnC, while G159D lies distal to site II in the C-terminus of cTnC and is closer to the cTnCcTnI IT arm binding site. On the basis of the locations of these mutations, we hypothesized that, for the D75Y and E59D mutations, the intramolecular effects within cTnC are sufficient to explain reported contractile defects, whereas altered cTnCcTnI interaction is required to explain the effects of G159D on contraction. To understand how molecular level changes precipitated by these mutations manifest at the level of myofilament contraction, we employed multiscale computational models, combining molecular dynamics, Brownian dynamics, and Markov models of myofilament activation. To address our hypotheses, we used a modified, previously described model [42] that includes Markov states representing the molecular events of calcium binding to cTnC and conformational changes in cTnC. We derived state transition rates from BD and MD simulations and compared computed steady-state forcepCa curves with experimental measurements from protein exchange experiments in rat cardiac myofilaments. This novel approach of coupling molecular-level effects to models of myofilament contraction can elucidate whether the observed molecular processes are sufficient to explain experimentally measured myofilament properties.

1.3 Materials and Methods

1.3.1 System Preparation

Four different human N-terminal or full length cardiac troponin C ((N)cTnC) Ca^{2+}-bound systems were investigated: wild-type cTnC, G159D cTnC (both based on PDB ID 1J1E), D75Y NcTnC, and E59D NcTnC (both based on PDB ID 1AP4). The initial preparation of the systems, including introduction of mutations, is described in refs [93] and [39]. The

Ca^{2+}-bound cTnC and cTnCG159D systems contained three bound Ca^{2+} ions (one in the N-terminal lobe and two in the C-terminal lobe). The Ca^{2+}-bound NcTnCD75Y and NcTnCE59D systems contained one bound Ca^{2+} ion (in the N-terminal lobe). No free unbound Ca^{2+} ions were present. Well-equilibrated structures after 150 ns of NAMD MD were used as input for the Anton system preparation. The scripts convertNAMDtoMaestro.2.5.py, viparr.py, and build_constraints.py were used to generate cms system files. An in-house perl script was used to fix the atomic number of potassium ions to 19 before running viparr. The script mae2dms converted the cms files into dms format. Subsequently guess_chem, refinesigma, and subboxer were used to prepare all the input files for the actual simulations.

1.3.2 Anton MD Simulations

All Anton simulations were performed under the NPT ensemble at 300 K using a Berendsen thermostat and barostat. Bonds involving hydrogen atoms were constrained using the SHAKE algorithm,(27) allowing for a time step of 2 fs. Structures were saved every 100.002 ps. Production runs were carried out on the 512-node Anton machine, running 75 jobsteps for wild-type Ca^{2+}-bound cTnC, 40 jobsteps for Ca^{2+}-bound cTnC-G159D, 40 jobsteps for Ca^{2+}-bound NcTnC-D75Y, and 40 jobsteps for Ca^{2+}-bound NcTnC-E59D. This corresponds to a total simulation time of 8.76 μs for wild-type Ca^{2+}-bound cTnC, 4.67 μs for Ca^{2+}-bound cTnCG159D, 7.16 μs for Ca^{2+}-bound NcTnCD75Y, and 7.16 μs for Ca^{2+}-bound NcTnCE59D.

1.3.3 Interhelical Angle Analysis and Estimation of Free Energy Cost of Opening the Hydrophobic Patch

The degree of opening of the hydrophobic patch can best be described by the interhelical angle between helices A and B [160]. For the analysis of interhelical angles, angles were calculated using interhlx (K. Yap, University of Toronto). Using interhelical angle analysis, the degree of openness for every frame of the trajectory was determined. The analysis was performed equivalent to what was described in ref [94]. Defining a cutoff angle below which

a state will be characterized as open and above which a state will be characterized as closed, the Boltzmann distribution of states was used to derive the free energy difference ΔG from the occupancies of the open and closed states. , where k_B is the Boltzmann constant, T is the temperature of the system, and N_{closed} and N_{open} are the number of systems found in the closed and open states, respectively, during the simulation. An A/B interhelical angle of 90° is generally considered the most accurate criterion for defining a structure to be open, since experimentally determined cTnI-bound structures of cTnC exhibit interhelical angles of around 90°. However, in the absence of cTnI, both apo and Ca^{2+}-bound cTnC are found in the closed conformation, with an interhelical AB angle of 135°. For the analysis, several different cutoff angles were used. Assuming that, for example, structures with interhelical angles below equally spaced values between 90 and 130° are considered open, free energy differences for the system transitioning into these semi-open conformations can be computed. This allowed extrapolation of the free energy even if the trajectory did not contain any opening event to 90°. We assumed a linear extrapolation to be valid, since previously a linear ΔG vs cutoff angle behavior was observed for a NcTnC mutant that opened all the way in the simulations [94] and there was nothing obvious about the systems used in this analysis that should prevent them from opening the entire way.

1.3.4 Clustering

For clustering, frames every 8 ps were extracted from the MD trajectories. Alignment was based on all C and D helix Cα atoms (cTnC residues 54-87) within 7 Åof the site II Ca^{2+}. Subsequent clustering was performed by RMSD using GROMOS++ conformational clustering [161]. A RMSD cutoff of 0.4 Å(wild-type cTnC), 0.5 Å(cTnC-G159D), 0.5 Å(NcTnC-D75Y), and 0.4 Å(NcTnC-E59D) was chosen, respectively. These cutoffs resulted in six (wild-type cTnC), six (cTnC-G159D), six (NcTnC-D75Y), and four (NcTnC-E59D) clusters that represented at least 90% of the respective trajectories. The central members of each of these clusters

were chosen to represent the calcium binding loop conformations within the cluster and thereby the conformations sampled by the trajectory.

1.3.5 Brownian Dynamics Simulations

Similar to studies presented in ref [39], Brownian dynamics simulations were performed with BrownDye [162] to estimate calcium association rates. PQR files for representative protein structures determined by a cluster analysis were generated using PDB 2pqr [163]. There were six (wild-type cTnC), six (cTnC-G159D), six (NcTnC-D75Y), and four (NcTnC-E59D) representative structures which were used in the BrownDye simulations. Since RMSD cutoffs between 0.4 and 0.5 Åhave been chosen, these structures are similar. The calcium pqr file was generated using a charge of +2 and an ionic radius of 1.14 Å. APBS [164] was used to generate the electrostatic fields for the protein and the calcium ion in openDX format. bd_top was used to generate all necessary input files for the BrownDye runs. A phantom atom of zero charge and negative radius (1.14 A) was introduced after the first execution of bd_top. The phantom atom was placed at the position of the calcium ion from the trajectory frame. It has no influence on the association rate constant calculation and serves solely to be able to define a reaction criterion that is spherically symmetric around the expected binding position of the calcium. The reaction criterion was chosen to be 1.2 Åwithin the calcium binding site for all structures in the analysis. 200,000 single trajectory simulations were performed on eight parallel processors using nam_simulation. The reaction rate constants were calculated using compute_rate_constant from the BrownDye package [162]. A weighted average of the rate constants of each of the representative cluster centers yielded an estimate of the overall rate constant for the system. The weight for each representative conformation was determined by the number of structures in the cluster.

1.3.6 Markov State Model of Myofilament Activation

Calcium binding to cTnC triggers a conformational change in cTnC (Figure 1.2A). This structural change exposes a hydrophobic patch within cTnC that facilitates the binding of cTnC to cTnI and triggers downstream intermolecular events leading to contraction.

To test the ability of the BD and MD simulations to predict behavior at larger scales, we modified a Markov model of thin filament regulation [42]. The four defined states in the original computational model are B0, blocked myofilament state where myosin S1 head binding to actin is blocked by Tm with no calcium bound to TnC; B, blocked state with calcium bound to cTnC; C, closed state where conformational changes in Tn are observed and Tm moves allowing weak binding of S1; and M, open state where strongly bound cross-bridges cycle. This model was expanded to a six-state model to accommodate myofilament states corresponding to intramolecular cTnC states probed by BD and MD simulations (Figure 1.2A). Thus, the current model incorporated the following additional states: B2, blocked calcium-bound state with conformational change of TnC exposing a hydrophobic patch, thereby allowing binding to TnI, and B3, blocked state with TnC bound to TnI (Figure 1.2B). By adding states B2 and B3 to the model, it was possible to use rates derived from BD/MD simulation in the Markov model. All simulations were done in terms of relative steady-state force as computed from the fraction of cross-bridges in state M. The model is a system of coupled differential equations guided by the following rate equations:

$$\frac{dP[B0]}{dt} = k_{Ca-}[B1] + k_{pr-}[B2] - k_{Ca+}[Ca^{2+}](t)[B_0] \tag{1.1}$$

$$\frac{dP[B1]}{dt} = k_{Ca+}[Ca^{2+}](t)[B0] + k_{pr-}[B2] - (k_{Ca-} + k_{pr+})[B1] \tag{1.2}$$

$$\frac{dP[B2]}{dt} = k_{pr+}[B1] + k_{IC-}[B3] - (k_{IC+} + k_{pr-})[B2] \tag{1.3}$$

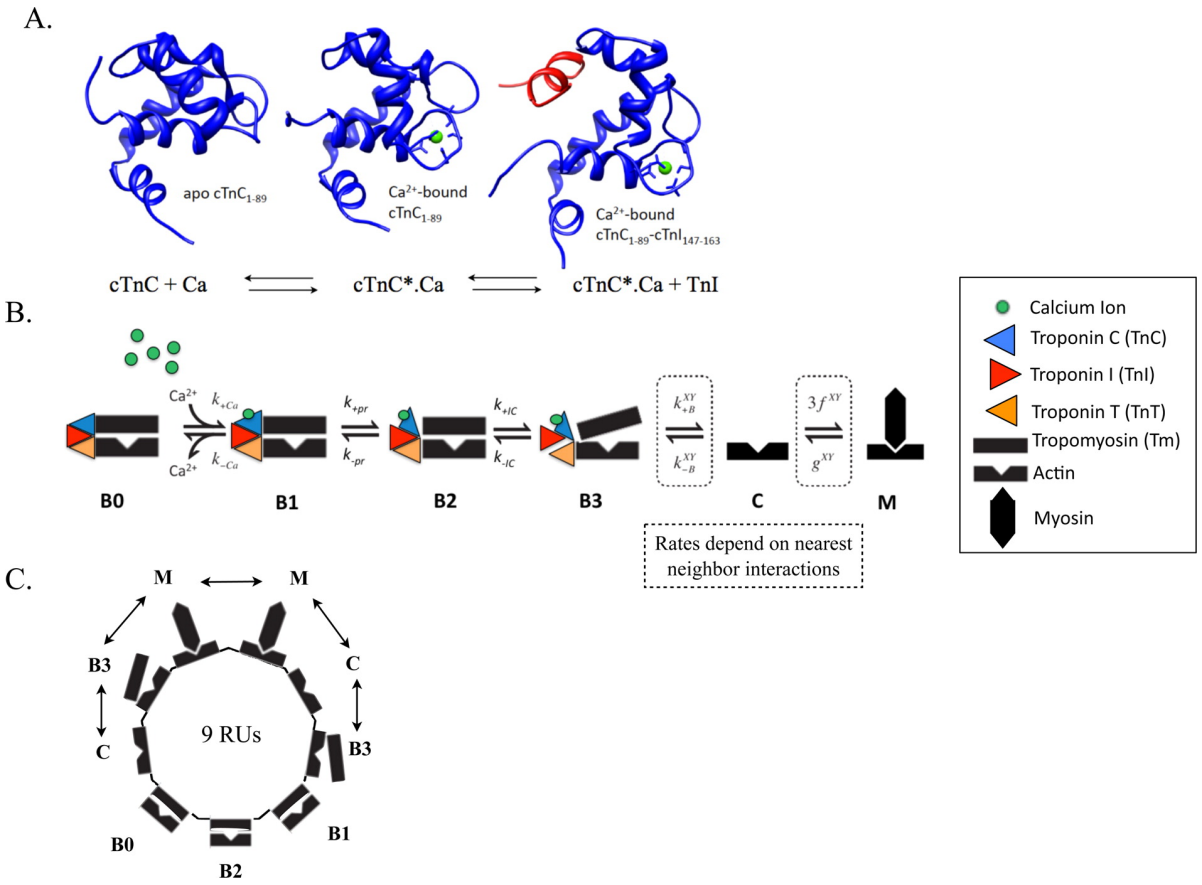

Figure 1.2. (A) Molecular state of cTnC (in blue) in apo state (B0 in the Markov model), calcium (in green) bound state (B1 in the Markov model), and calcium-bound state with exposed hydrophobic patch allowing for cTnI (in red) to bind to cTnC (B2 in the Markov model). (B) Schematic of one regulatory unit (RU) sequence of the six-state (B0, B1, B2, B3, C, M) Markov model of co-operative myofilament activation with nearest neighbor interactions. (C) Schematic of ring structure mathematical formulation used to solve the Markov model that incorporates looping of short segments of RUs to allow elimination of redundant states due to symmetry, resulting from the tight co-operative coupling of nine adjacent RUs, linked by tropomyosins, depicted in one possible configuration of nearest neighbor interactions (the double-headed arrow) (see Methods and ref [42] for more details). The nearest neighbor interactions of one RU with two adjacent RUs, X and Y, which could be in either Markov state B3, C, or M (as in ref [42]), determine the degree of co-operativity of myofilament activation in the Markov model.

$$\frac{dP[B3]}{dt} = k_{IC+}[B1] + k_{off-}[C] - (k_{on} + k_{IC-})[B3] \tag{1.4}$$

As in the earlier model [42], actin regulatory units (RUs), are comprised of seven actin

monomers, TnC, TnI (the inhibitory subunit of Tn), and Tm, together with the S1 region of myosin. Each regulatory unit can bind to one myosin, and there is cooperativity in activation of RUs based on nearest neighbor interactions in state B3, C, or M (Figure 1.2C). We solved for nine coupled RUs in the current model. Our model requires an updated calculation of the ϕ, a number reflecting the probability of blocked RUs where cTnI does not inhibit movement into the closed (C) state. The quantity must now reflect the addition of states B1 and B2:

$$\phi = \frac{P(B) - P(B0) - P(B1) - P(B2)}{P(B)} \tag{1.5}$$

Steady-state simulations were performed to generate force-pCa curves as determined experimentally. Therefore, all rates with respect to time reduced to zero and the system of equations was simplified considerably into a linear problem that is solved using eigenvalues. State transitions and model parameterization: For each state transition, we needed to parameterize the forward and reverse rates of transition. For the transition B0 to B1, the calcium binding k_{Ca+} on-rate and k_{Ca-} off-rate were obtained from literature values for rat myofilaments at 27°C [165, 166]. For state transition B1 and B2, k_{pr+} values were plugged in directly from MD simulation results and k_{pr-} was fitted to a standardized wild-type curve at 27 °C in rat cardiac myofilaments. The forward and reverse rates (k_{IC+} and k_{IC}; k_{B+} and k_B) for state transitions, B2 to B3 and B3 to M, respectively, were optimized to fit the wild-type steady-state forcepCa relationship in rat myofilaments at 27 °C. The apparent forward (f^{xy}) and reverse (g^{xy}) rates of cross-bridge cycling for state transition C to M were calculated on the basis of K_{tr} ($K_{tr} = f^{xy} + g^{xy}$) and ATPase Q10 values from ref [124] with the formula:

$$Q_{10} = (R_1/R_2)^{10/(T2-T1)} \tag{1.6}$$

where R_1 and R_2 are reaction rates at temperatures T1 and T2. The wild-type steady-state forcepCa curve was standardized to 27 °C for rat myofilaments by calculating the T_{max},

EC_{50}, and Hill coefficient n_H to 27 °C based on the Q_{10} values from the literature [124] and fitted using the Hill equation:

$$P(Ca^{2+}) = P_{max}[Ca^{2+}]^{n_H}/([Ca^{2+}]^{n_H} + EC_{50}^{n_H}) \tag{1.7}$$

where P(Ca^{2+}) is the calcium-dependent force, P_{max} is the maximum myofilament force, EC_{50} is the calcium concentration at 50% force, and n_H is the Hill coefficient. In order to optimize the WT steady state forcepCa curve simulation, parameters k_{IC+}, k_{IC}, μ_M, and μ_B were varied in combination to minimize RMSD between simulated and experimental WT data. For all mutations, k_{Ca+} and k_{pr+} rates were altered on the basis of MD data but all other rates and co-operativity coefficients in the model were assumed to remain constant in the mutated state. The matlab code for the Markov model has been provided as part of the Supporting Information. The cTnC alignment BLAST tool was used to perform protein sequence alignment corresponding to the cTnC FASTA sequence for rat (Rattus Novergicus, gi 66969456) and human (Homo sapiens; gi 2460249).

1.4 Results and Discussion

1.4.1 Full Atom, Explicit Solvent Simulations of Full Length cTnC Show Straightening of the Linker Region

First, we investigated the molecular behavior of wild-type Ca^{2+}-bound cTnC. The N-terminal cTnC EF-hands (helices A-D), which are known to be metal-binding sites, are labeled sites I and II [167]. The C-terminal domain is linked to the regulatory domain by a short flexible linker (approximately residues 89-93). Four more helices (E-H) comprise two more EF-hands with calcium binding sites III and IV. Site II, the low-affinity, Ca^{2+}-specific Ca^{2+}-binding site, is generally considered the only site directly involved in calcium regulation of cardiac muscle contraction [168]. Previous simulations focused only on NcTnC and not the relative dynamics of NcTnC and CcTnC. To account for changes in the interdomain arrangement of

cTnC, we monitored the pairwise distances between calcium binding sites II, III, and IV as a measure of the relative distances between the domains. Pairwise distances between the three calcium ions in the 1J1E crystal structure are 41 Å(Ca^{2+}II-Ca^{2+}III), 32 Å(Ca^{2+}II-Ca^{2+}IV), and 12 Å(Ca^{2+}III-Ca^{2+}IV), respectively. The distance between site III and IV Ca^{2+} remained around its crystallographic value throughout the entire 9 μs simulation (Figure 1.3A). This distance confirms structural integrity within CcTnC over the course of the simulation but is not a measure of interdomain arrangement. The distances between site II Ca^{2+} and site III/IV Ca^{2+}, respectively, were sensitive to the NcTnC-CcTnC interdomain arrangement. Over the first 800 ns, they remained around their crystallographic values (with the exception of a short-lived extension within the first 100 ns). After about 800 ns of simulation, both distances increased by about 10 Åand remained in that state stably for the rest of the simulation, as shown in Figure 1.3A. This increase in intercalcium distance was caused by a straightening of the central cTnC helix, leading to an increased distance between NcTnC and CcTnC (see Figure 1.3B). Experimentally, it has been demonstrated that isolated cTnC takes on a more extended form than cTnC anchored in the cTn complex [169]. Similar trends are observed for the homologous calmodulin protein, for which the Ca^{2+}-bound state assumes an elongated conformation that maximally separates the N- and C-terminal globular domains in the absence of a target protein but subsequently collapses when a target protein is presented [170]. These simulation results are therefore consistent with experimental observations.

1.4.2 Effects of cTnC DCM Mutations on the Calcium Binding Affinity of cTnC

Brownian dynamics (BD) simulations of the effects of the mutations on calcium association gave estimated association rate constants for calcium binding to the wild-type cTnC, NcTnC-D75Y, cTnC-E59D, and cTnC-G159D systems (Table 1.1). The average calcium association rate constant of wild-type cTnC was determined from Brownian dynamics simulations on representative structures from the MD simulations of wild-type Ca^{2+}-bound cTnC to be

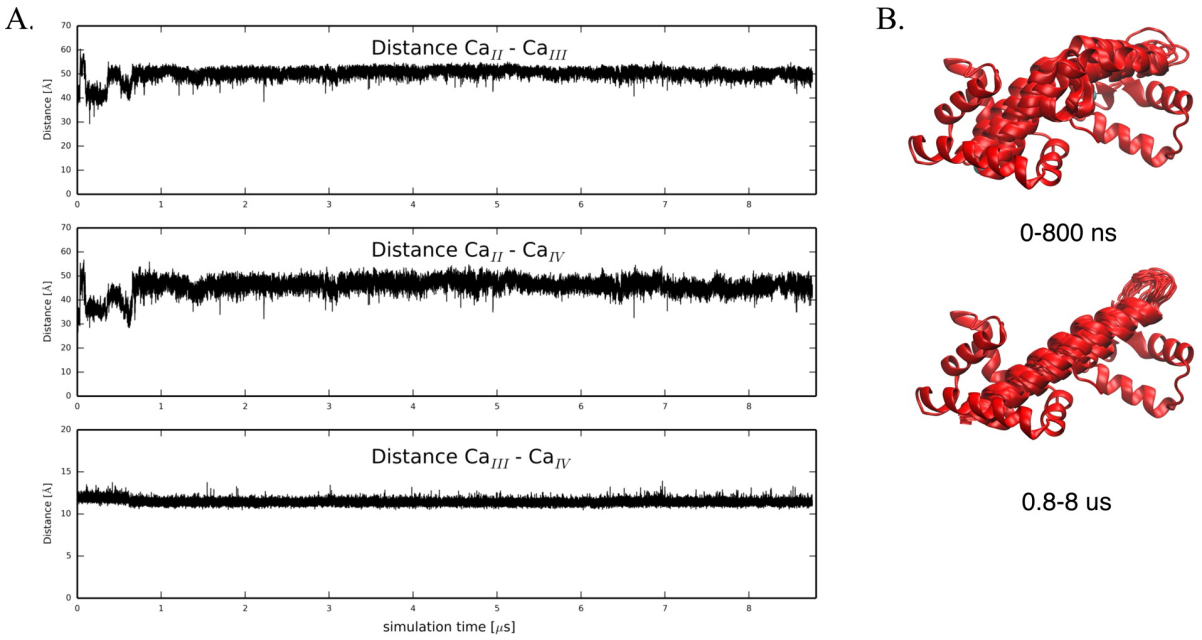

Figure 1.3. (A) Pairwise distances between Ca^{2+} in binding sites II, III, and IV, respectively. Distance between Ca^{2+}_{II}-Ca^{2+}_{III}, Ca^{2+}_{II}-Ca^{2+}_{IV}, and Ca^{2+}_{III}-Ca^{2+}_{IV} over the course of an 8.76 μs MD simulation for wild-type Ca^{2+}-bound cTnC. (B) The simulation starts with a bent central helix and remains in a kink for about 800 ns. After about 800 ns, the central helix in cTnC straightens and remains straight until the end of the simulation (0.88.8 μs).

$1.5 * 10^8 1/(M*s)$ (Table 1.1). This is in good agreement with the association rate determined for wild-type NcTnC ($3.1 * 10^8 1/(M*s)$(16)). Additionally, these rates are in excellent agreement with experimentally determined values of $(2-4) * 10^8 1/(M*s)$ for wild-type isolated cTnC [165, 171, 172], while Ogawa reported a diffusion limited association ($> 4 * 10^7 1/(M*s)$) [173]. The idea behind our approach was to adjust the BD parameters so that we can reproduce values for the wild-type systems and then make predictions for mutant systems for which no published data is available. The average calcium association rate constant of NcTnC-D75Y was determined to be $5.0 * 10^6 1/(M*s)$, a 50-fold reduction from its wild-type value. This is in agreement with experimental data suggesting a decrease in calcium affinity in NcTnC-D75Y [22]. The direct effect of D75Y causing decreased Ca^{2+} binding affinity is not surprising given the proximity of the mutation to one of the Ca^{2+} coordination sites (E76) in the regulatory calcium-binding site. BD simulations for E59D performed on a set of structures representing

the conformations of the calcium-binding site most commonly observed during the 7.16 μs MD simulation predicted an average calcium association rate constant for NcTnC-E59D of $1.2 * 10^7 1/(M * s)$, a 10-fold reduction from the wild-type value. Since there is no effect in myofilaments, this suggests that the cTnC-E59D calcium dissociation rate may also differ in counteraction to the reduced association rate [22, 171]. The BD simulations for G159D predicted an average calcium association rate constant of cTnC-G159D of $1.0 * 10^6 1/(M * s)$, about a 100-fold reduction from its wild-type value. Interestingly, these results suggest the mutation G159D may have direct allosteric effects on the N-terminus of cTnC affecting calcium binding to cTnC. The finding of a lower calcium association rate was unexpected, since cTnC-G159D has been associated with an unaltered or increased Ca^{2+} sensitivity in skinned myofilaments from rat and human, respectively [148, 25]. Thus, we speculated that cTnC-cTnI interaction effects will be required to explain the steady-state contractile effects of G159D.

1.4.3 Effects of cTnC DCM Mutations on Rates of cTnC Conformational Change on Calcium Binding

Exposure of a hydrophobic patch between cTnC helices A and B is facilitated by calcium binding at site II and can be significantly modulated by mutations [94]. It is crucial for binding of the cTnI switch peptide in the context of regulating muscle contraction. Since the hydrophobic patch opening frequency is in the high nanosecond to low microsecond regime, long time-scale simulations have the potential to quantitatively investigate the kinetics of the opening and closing of the cTnC hydrophobic patch. Here we elucidated the hydrophobic patch opening behavior of all three systems under investigation using microsecond Anton [174] simulations. The degree of opening of the hydrophobic patch can best be described by the interhelical angle between helices A and B [160]. Both apo and Ca^{2+}-bound cTnC are found in the closed conformation [152, 175], with an interhelical A-B angle of 135° [152]. The cTnI switch peptide must be present to stabilize the open conformation of the Ca^{2+}-bound regulatory domain of cTnC (interhelical A-B angle of 90°) [153, 176], since the

open conformation is only a transient state that is sampled by cTnC after Ca^{2+} binding [94, 39]. Kinetics and the free energy difference of the opening-closing process were extracted from the simulations, shedding light on the different ways that the mutations affect the process of contraction. The intramolecular conformational changes induced by Ca^{2+} binding and the subsequent association of the cTnI switch peptide have been measured experimentally to be significantly slower than the actual Ca^{2+} binding [165, 172]. Unfortunately there is no direct experimental observable that can confirm the simulations in terms of frequency and degree of hydrophobic patch opening. However, simulated data for gain-of-function and loss-of-function mutations agreed with expected opening behavior [94]. Additionally, by simulating the force-pCa curves from the BD and MD results, we obtain indirect experimental verification. The A/B interhelical angle as a function of simulation time is a measure of the average degree of openness of cTnC. Qualitatively, NcTnC-D75Y (Figure 1.4A) had a similar behavior to wild-type NcTnC (see ref [94]), in that it remained closed most of the time but occasionally ventured to transiently open conformations (105°). A more quantitative analysis of the opening of the hydrophobic patch in cTnC can be gleaned using a set of incremental cutoff angles dividing structures into respective open and closed conformations, as shown in Figure 1.4B. While the experimentally determined cTnI-bound structures of cTnC all exhibit A/B interhelical angles of around 90° (which will be considered the most stringent criterion of defining a structure to be open), we chose angles between 135 and 90° as cutoff angles. For each of these cutoff angles, the Boltzmann distribution of states was used to derive the free energy difference ΔG based on the occupancies of the open ($\leq$ cutoff angle) and closed ($>$cutoff angle) states, . In a related analysis, we also evaluated the average time between open conformations as a function of the same cutoff angles (Figure 1.4B). Compared with wild-type NcTnC, NcTnC-D75Y had a slightly opened equilibrium A/B interhelical angle of 130°. This causes opening to A/B interhelical angles between 110 and 130° to be related with a slightly lower free energy cost than the wild-type system. The frequency of the most opened sampled conformations

Table 1.1. Summary of Calcium Association Rates (from BD Simulations), Computed Free Energy Differences between Open and Closed States (from MD Simulations), and Average Simulation Time between Opening Events (from MD Simulations) for a Cutoff Angle of 110°

System	k_{on} [1/(M*s)]	Δ G (kcal/mol)	Δ t
wild-type Ca^{2+}-bound NcTnC	3.1 * 10^8	4.0	130 ns
NcTnC-D75Y	5.0 * 10^6	3.3	30 ns
NcTnC-E59D	1.2 * 10^7	2.7	40 ns
cTnC-G159D	1.0 * 10^6	5.2	700 ns

(A/B interhelical angle 105°) was identical in NcTnC-D75Y and NcTnC. Sampling of even further opened conformations would require simulations beyond the low microsecond time scale and was not feasible. Nonetheless, we are estimating that the free energy difference between a fully closed and fully open state is slightly larger for NcTnC-D75Y compared to wild-type NcTnC, even though it is hard to make accurate predictions, since the shape of the NcTnC-D75Y ΔG curve deviates somewhat from a linear relationship. We also evaluated the average time between open conformations as a function of the same cutoff angles (Figure 1.4B). The opening frequency of fully opened conformations (A/B interhelical angle of 90°) was extrapolated to be in the 100 μs to 1 ms range. This would correspond to a 2-20-fold decrease in the opening frequency compared to wild-type. We found that a semiopen configuration (A/B interhelical angle of 110°) was sufficient to model changes to myofilament mechanics (see below). Table 1.1 summarizes those values for a cutoff angle of 110°.

The cTnC-E59D mutation is interesting, since experimentally it has been found to reduce calcium affinity and sensitivity of myofilaments in a cTnC-D75Y/E59D system. cTnC-E59D however was functionally benign and did not impact calcium sensitivity of myofilaments in experiments [22]. Here we investigated the molecular effects of cTnC-E59D on hydrophobic patch opening using microsecond MD simulations, as shown in Figure 1.4A (A/B interhelical

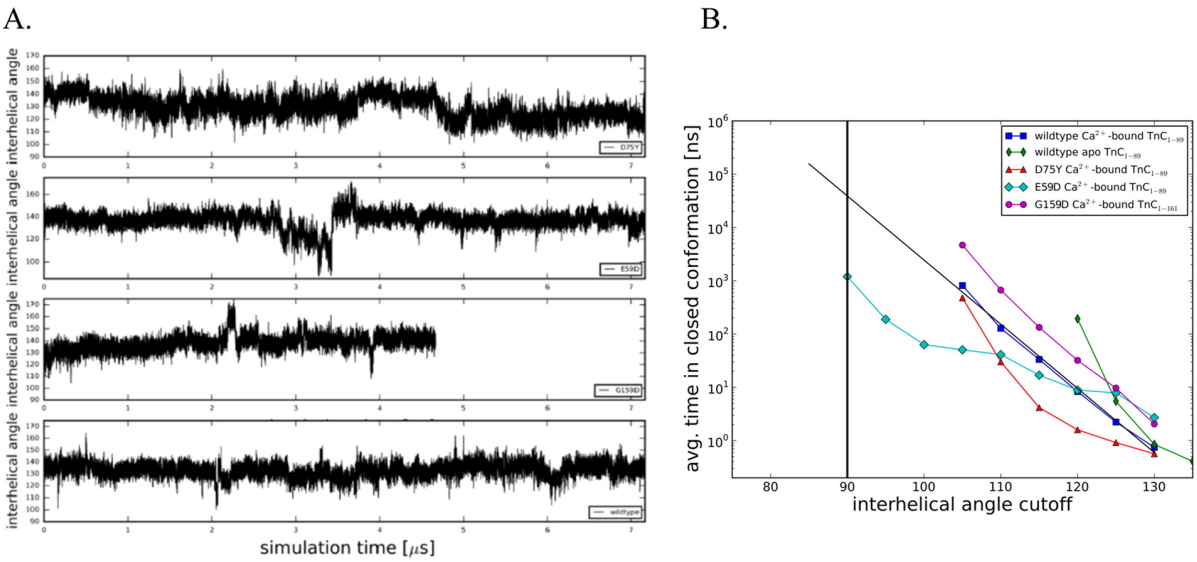

Figure 1.4. (A) Interhelical angles over the course of the simulations for Ca^{2+}-bound wild-type NcTnC, Ca^{2+}-bound NcTnC-D75Y, Ca^{2+}-bound NcTnC-E59D, and Ca^{2+}-bound cTnC-G159D. Interhelical angles are a measure of the openness of the hydrophobic patch between cTnC helices A and B. An interhelical angle of 135° corresponds to a closed conformation, while an angle of 90° corresponds to a fully open conformation. (B) Average simulation time between opening events in dependence on the cutoff angle. Values for the Anton wild-type Ca^{2+}-bound TnC simulation, the Anton wild-type apo TnC simulation (both from ref [94]), and the three Ca^{2+}-bound DMC mutation (NcTnC-D75Y, NcTnC-E59D, cTnC-G159D) simulations are shown. The widely accepted openclose cutoff criterion of 90° is marked by a vertical black line.

angle as a function of simulation time for NcTnC-E59D). While still being in the closed conformation on average, for about 500 ns, the system was in a semiopen conformation opening up all the way to 87.4°. This is reflected in a free energy difference between the open and closed conformations of 6 kcal/mol compared to 8 kcal/mol for wild-type NcTnC (Figure 1.4, Table 1.1). Similarly, the time between full opening events (A/B interhelical angle of 90°) drops to 1 μs compared to 50 μs for wild-type NcTnC (Figure 1.4). Again, Table 1.1 summarizes those values for a cutoff angle of 110°. For cTnC-G159D, we also computationally determined the molecular effects on hydrophobic patch opening. Experimentally this mutation has been associated with an increased [148] or unchanged [25] Ca^{2+} sensitivity. The hydrophobic patch remains closed through all of the 4.67 μs of MD simulation and never opens beyond 107.3°.

This is reflected in a free energy difference between the open and closed conformations of 9.5 kcal/mol compared to 8 kcal/mol for wild-type NcTnC (Figure 1.4). Similarly the time between full opening events (A/B interhelical angle of 90°) increases to 800 μs compared to 50 μs for wild-type NcTnC (Figure 1.4). Table 1.1 summarizes those values for a cutoff angle of 110°.

1.4.4 *In Silico* Translation of Molecular Level Changes to Myofilament Mechanics

The primary sequence of cTnC is identical between rat and human with the exception of one amino acid in the linker region and one in the C-terminus domain of cTnC (Figure 1.5A). Also, there are no other known isoforms of TnC in the heart. Thus, the MD and BD simulation results for human cTnC can be applied to a Markov model standardized to rat parameters.

The current six-state Markov model describes cTnC activation by calcium and co-operative myofilament activation (Figure 1.2B,C). Thin filament regulation is similar to the myofilaments in that the calcium binding to cTnC (Markov state B1) triggers a conformational change in cTnC (Markov state B2) which leads to conformational changes in cTnI and cTnT (lumped Markov state B3) such that Tm moves allowing for weak binding of cross-bridges to bind to actin (Markov state C). The weakly bound cross-bridges then cycle to load-bearing strongly bound cross-bridges that generate force (Markov state M). Thus, the Markov model explicitly defines the physiological states of calcium binding to cTnC and the conformational changes that result in cTnC as a consequence. Also, the downstream conformational changes that occur in myofilament activation are implicitly defined in the lumped Markov states B3 and C. Lastly, in the model only one cross-bridge binds per RU; however, physiologically at least seven cross-bridges can bind per RU. The model computes the co-operative nature of thin filament activation of myofilaments by nearest neighbor interactions. By adding states B2 and B3 to the model, it was possible to use rates derived from BD/MD simulation in the Markov model.

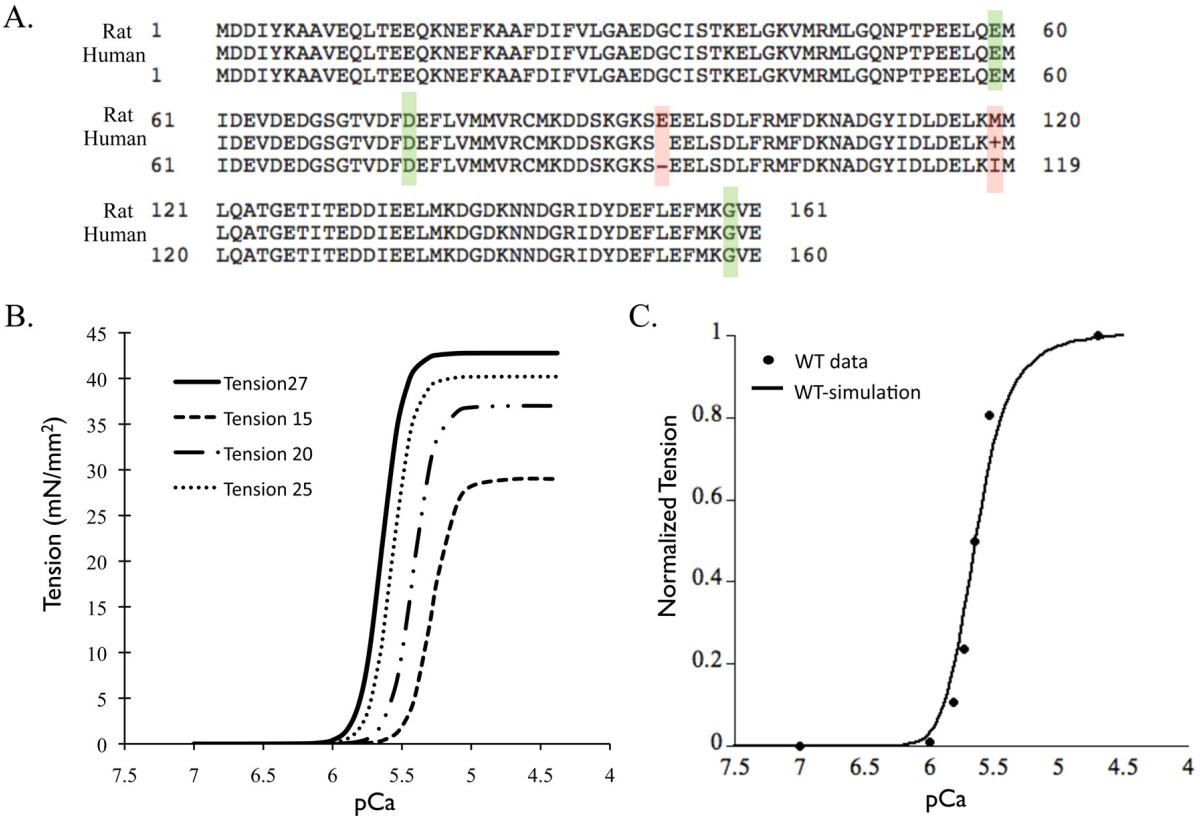

Figure 1.5. (A) Sequence alignment of cTnC for protein sequences from rat and human, highlighting the conserved DCM mutations (green box) and two residue difference (red box) in the N-terminus lobe of cTnC. (B) Standardized steady-state forcepCa relationship at 27, 25, 20, and 15 °C (data extracted from ref [124]). (C) Steady-state force-pCa curve simulation (solid black trace) fit to the standardized force-pCa relationship (solid black dots) for rat myofilaments at 27 °C (300 K).

In order to maintain uniformity of parametric conditions (temperature and species) when scaling up longitudinally from molecular state to myofilament state, we computed the wild-type myofilament properties for rat myocardium at 300 K. The resultant steady-state forcepCa relationship at 300 K (Figure 1.5B) had a pCa value of 5.64, a Hill coefficient of 5.7, and a maximal tension of 42.78 mN/mm2, computed using Q10 values that were experimentally derived for steady-state forcepCa in skinned rat myofilaments [124]. The simulation result from the Markov model fit to the steady-state wild-type forcepCa curve for rat myofilaments at 300 K within less than 5% error range (Figure 1.5C). It is known that kinetic rates of a given state transition vary in isolated molecular states of cTnC and integrated myofilament states [166].

This was very well elucidated in a previous study [166] where the off-rates of calcium binding were studied in depth from isolated cTnC molecule to a structurally integrated myofilament preparation. Thus, here we describe the choice of transitional kinetic rate parameters for each Markov state transition. The rate of calcium binding to cTnC has been measured experimentally for rat to be $1.4 * 10^8 (M * s)^1$ [165]. This rate is not reported to change in isolated cTnC in solution vs in integrated myofilaments. However, the off-rate of calcium binding to cTnC is highly sensitive to its corresponding system state (isolated or integrated). Accordingly, we chose the off-rate of calcium as measured in the rigor state of myofilaments at 25 °C.(34) For the conformational state transition of cTnC in myofilaments, we assumed that these kinetic rates are largely insensitive to system state. Thus, we directly input the values from the MD simulations. Further, the transition Markov states B2 to B3 and B3 to C are lumped states, as they implicitly integrate intermolecular associations between TnC-TnI-TnT-Tm-actin and thin filament co-operativity. Thus, the parameters for these state transitions were scaled to fit the standardized wild-type steady-state force-pCa relationship. Lastly, for the state transition C to M, the apparent forward (f_{app}) and reverse (g_{app}) rates of cross-bridge cycling were derived from reported Q10 of K_{tr} and tension cost [124]. Input parameters for each state transition are summarized in Table 1.2 (Figure 1.2).

1.4.5 Myofilament Effects of DCM cTnC Mutations

The parameters for the optimized best-fit wild-type steady-state force-pCa curve were determined (Figure 1.5C, Table 1.2). For each cTnC mutation, all parameters in the Markov model were kept constant, except for the intramolecular values for calcium binding to cTnC and forward rate of conformational change of cTnC such that the hydrophobic patch is exposed within cTnC (see Table 1.3). The values of these intramolecular cTnC state transitions were input directly as reported by MD and BD simulations for all three DCM mutations.

The Markov model simulation for the D75Y-cTnC system resulted in a decrease in

Table 1.2. Best-Fit Parameters in the Six-State Markov Model of Myofilament Activation for WT Rat Cardiac Myofilaments at 300 K Steady-State Force-pCa Relationship

Parameter	WT
k_{Ca+} [1/(μ M * ms)]	0.14
k_{Ca-} [1/(ms)]	0.25
k_{pr+} [1/(ms)]	5699.43
k_{pr-} [1/(ms)]	19500
k_{IC+} [1/(μ M * ms)]	0.01
k_{IC-} [1/(ms)]	0.08
k_{B+} [1/(ms)]	18
k_{B-} [1/(ms)]	0.04
f^{XY} [1/(ms)]	0.04184
g^{XY} [1/(ms)]	0.01892
γB	80
γM	75
μM	46

calcium sensitivity of myofilaments, as seen by a rightward shifted steady state force-pCa curve (Figure 1.6A). This decrease in calcium sensitivity is consistent in direction with experimental recordings in skinned cTnC-D75Y mutant myofilaments [22, 23]. However, the magnitude of the decrease in calcium sensitivity of myofilaments was significantly exaggerated by the Markov model prediction compared to experimental data. This could be because of either the (a) likely changes in the rate of hydrophobic patch closing which we assume to not change in mutations or (b) rather unlikely allosteric effects of cTnC-D75Y mutation in the CcTnC domain that may change the rate of calcium binding to cTnC and rate of hydrophobic patch exposure. This result suggests that the decrease in calcium binding affinity of cTnC coupled with the decrease in ΔG can explain the directional shift in the steady-state force-pCa relationship showing a decrease in calcium sensitivity of tension in skinned myofilaments for cTnC-D75Y.

The Markov model of E59D-cTnC did not shift the force-pCa relationship relative to the wild-type steady state force-pCa curve (Figure 1.6B), consistent with experimental observations in skinned myofilaments [22, 23]. This was interesting, as the calcium binding affinity of E59D-cTnC was decreased but the ΔG for the E59D-cTnC conformational change was increased.

Table 1.3. Parameters in the Six-State Markov Model of Myofilament Activation for WT, D75Y-cTnC, E59D-cTnC, and G159D- cTnC Rat Cardiac Myofilaments at 300 K Steady-State Force-pCa Relationship for a Cutoff Angle of 110°

Parameter	WT	D75Y	E59D	D159D	G159D (cTnC-cTnI Interactions)
k_{Ca+} [1/(μ M * ms)]	0.14	0.005	0.012	0.001	0.001
k_{Ca-} [1/(ms)]	0.25	0.25	0.25	0.25	0.25
k_{pr+} [1/(ms)]	5699.43	26435.49	27055.77	1337.31	1337.31
k_{pr-} [1/(ms)]	19500	19500	19500	19500	19500
k_{IC+} [1/(μ M * ms)]	0.01	0.01	0.01	0.01	0.01
k_{IC-} [1/(ms)]	0.08	0.08	0.08	0.08	3.87 X 10^{-4}
k_{B+} [1/(ms)]	18	18	18	18	18
k_{B-} [1/(ms)]	0.04	0.04	0.04	0.04	0.04
f^{XY} [1/(ms)]	0.04184	0.04184	0.04184	0.04184	0.04184
g^{XY} [1/(ms)]	0.01892	0.01892	0.01892	0.01892	0.01892
γB	80	80	80	80	80
γM	75	75	75	75	75
μM	46	46	46	46	46

While this did imply that the intramolecular alterations could offset the phenotype such that it may appear benign as observed experimentally, it is remarkable that the effects in and of themselves are sufficient to replicate the experimentally reported results when the cTnI switch peptide can bind to cTnC in the partially open conformation state. The experimentally determined cTnI-bound structures of cTnC exhibit A/B interhelical angles of around 90° (which will be considered the most stringent criterion of defining a structure to be open). It is probable that cTnI is able to associate with cTnC before this fully open conformation is achieved. We explored this possibility with the Markov model. The simulation results for cTnC-E59D showed that a partially opened conformation state of cTnC at an opening angle of 110° could explain the experimental observations. Interestingly, simulation results for a 90° opening angle for E59D-cTnC showed a significant leftward shift in force-pCa relationship unlike a modest leftward shift for D75Y-cTnC. This was explained by the smaller change in ΔG, with an increase in opening angle, for D75Y than E59D based on MD simulation results. These results would implicate that the switch peptide of cTnI must bind to cTnC in its partial open conformation state. To validate the prediction that cTnI can bind to a partially open conformation of cTnC would require more sophisticated MD simulations with the whole cTn structure and a more explicitly defined Markov model state for cTnC-cTnI interaction with experimentally derived parameters. Although these are beyond the scope of the current study, we can conclude that E59D-cTnC mutation intramolecular interactions could explain experimental observations if a more relaxed opening angle for cTnI binding is sufficient.

The Markov model simulation for the G159D-cTnC system predicted an extremely right shifted steady state forcepCa curve (Figure 1.7A). This is not meaningful, as the heart will likely fail under such extreme conditions and neither were such values reported from experimental observations. In fact, the tightly controlled experimental results in rats suggest that G159D is a benign mutation and has no apparent effect on myofilament contractile function [25, 177]. The calcium affinity values for cTnC from BD simulations and delta G values from

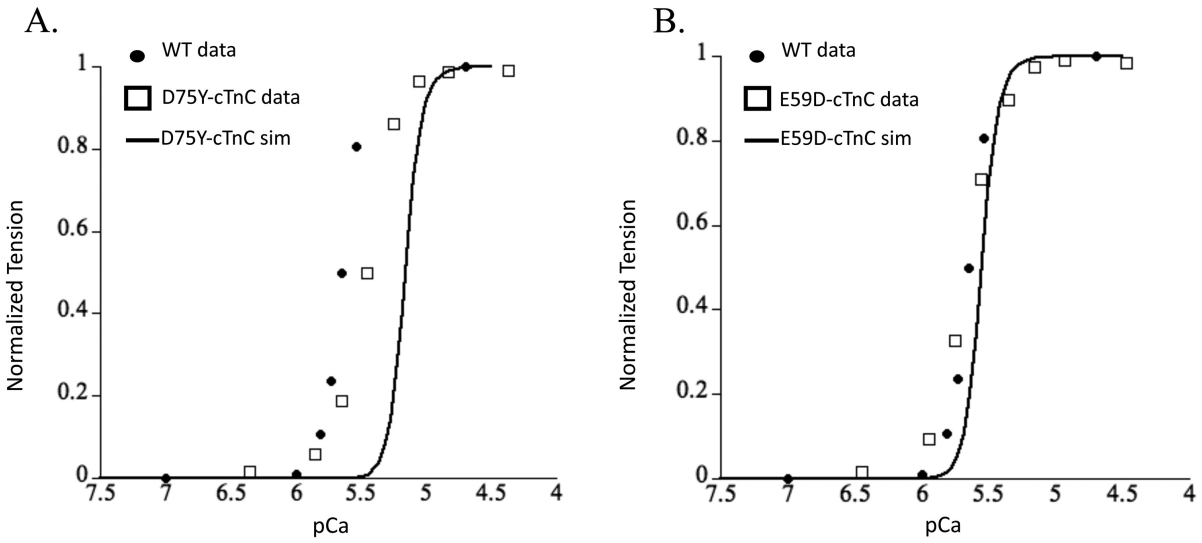

Figure 1.6. Steady-state force-pCa simulation (solid black trace) prediction for (A) cTnC-D75Y mutation and (B) cTnC-E59D mutation plotted with experimental measures of the same for WT (solid black dots) and DCM cTnC mutations (open squares) for (A) cTnC-D75Y and (B) cTnC-E59D from skinned myofilaments.

MD simulations suggest an offsetting intramolecular interaction, but clearly these effects are not sufficient to capture the experimentally reported benign phenotype. This would suggest that changes in cTnC-cTnI interactions potentially offset the resultant intramolecular effects. Such a scenario would not be surprising given that the G159D residue is in the cTnC-cTnI interaction region. In fact, when we hold all other parameters constant except for lumped state transition B2 to B3, simulation results can predict experimentally observed results (Figure 1.7B). It is important to note here that this fit was possible only when the KD (equilibrium constant) of the state transition between B2 and B3 was significantly lowered. Assuming that the change in this lumped state transition is only because of a change in cTnC-cTnI interaction, then this would suggest that the mutant G159D-cTnC leads to structural change in cTnC that increases its affinity for cTnI. The opening angle change to 110° was not enough to predict experimentally reported myofilament effects. These observations do suggest that cTnC-cTnI interaction is perturbed by G159D but are certainly not conclusive. Clearly, other factors within cTnC (such as calcium dissociation rate) and beyond (such as cTnC-cTnI affinity or PKA

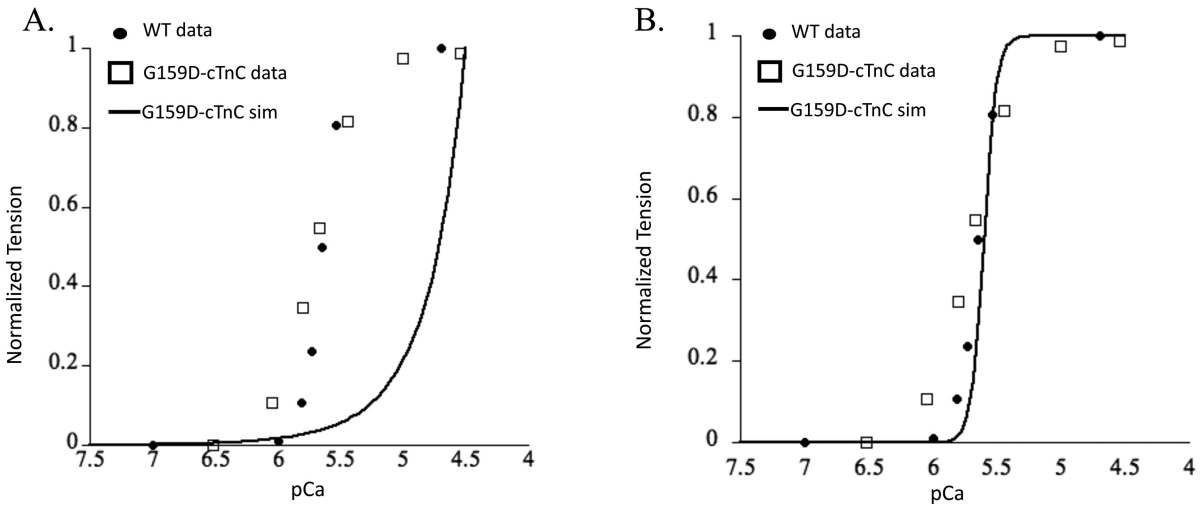

Figure 1.7. Steady-state force-pCa simulation (solid black trace) prediction for (A) cTnC-G159D mutation and (B) cTnC-G159D mutation fitted when accounting for cTnC-cTnI interaction effects (see text for details) plotted with experimental measures of the same for WT (solid black dots) and cTnC-G159D mutant (open squares) from skinned myofilaments.

phosphorylation of cTnI) also have a profound impact on myofilament Ca^{2+} sensitivity. These factors are still beyond the reach of our molecular scale and myofilament scale computational analysis. The current six-state model (Figure 1.2B) does not explicitly define the cTnC-cTnI interaction as a Markov state in itself but lumps it in the B3 state where cTnC-cTnI-cTnT-Tm-actin interactions take place. This is likely the reason that the Markov simulation results in an extremely right shifted contractile response. Incidentally, the cTnC-G159D mutation has been shown to interfere with the modulation of Ca^{2+} sensitivity through cTnI PKA phosphorylation at cTnI sites Ser 23 and Ser 24 [25, 81]. We speculate that this effect outweighs the reversed effects on hydrophobic patch opening and calcium association. Nonetheless, the multiscale *in silico* modeling approach described here is a robust way to study how molecular effects can longitudinally translate to myofilament contractile response.

1.5 Summary and Conclusions

We investigated alterations in calcium association rates to mutant cTnC using Brownian dynamics (BD) simulations and the opening frequency of the hydrophobic patch using μs time

scale MD simulations. All three mutations decreased the cTnC calcium association rate by 10-100-fold, but while D75Y and G159D caused a 10-fold decrease in the hydrophobic patch opening frequency, the E59D mutation increased the opening frequency by 50-fold compared with WT. Using these findings, we scaled the molecular state results from BD and MD simulations to myofilament state by solving a six-state Markov model of myofilament contraction. This multiscale approach enabled us to test and understand the intramolecular effects of cTnC DCM mutations on contractile function. Results from the myofilament simulations suggest that the intramolecular changes resulting from the cTnC mutation D75Y and E59D can explain experimentally observed directional changes in calcium sensitivity of myofilaments, provided the cTnI switch peptide can associate with the N-terminus of cTnC in a partially open state of cTnC. However, intramolecular changes observed in the G159D genotype of cTnC are not sufficient to explain the experimentally observed contractile effects. Importantly, they shed light on how the interaction of cTnC with cTnI can offset the intramolecular effects of G159D cTnC mutation observed in DCM. To summarize, we report the intramolecular changes and potential cTnC-cTnI interactions in cTnC DCM mutants that underlie experimentally observed contractile defects. This is important from a drug development standpoint, as it highlights how intramolecular cTnC changes and/or cTnC-cTnI interactions can be interactive and offsetting, to the extent that a known DCM mutation may appear to be benign functionally. To our knowledge, this is the first study to integrate and leverage *in silico* modeling approaches from molecular level (MD simulations) to myofilament level (Markov models of contractility). This is a promising step toward demonstrating the feasibility and applicability of multiscale modeling to gain mechanistic insights into the role of known genetic DCM mutations in contractile proteins.

1.6 Acknowledgements

Chapter 1, in full, is a reprint of the material as it appears in: Dewan S, McCabe KJ, Regnier M, McCulloch AD, Lindert S (2016) ”Molecular Effects of cTnC DCM Mutations on Calcium Sensitivity and Myofilament Activation - An Integrated Multi-Scale Modeling Study”. J. Phys. Chem. 120(33), pp 8264-8275. The dissertation author was the second author of this paper, and contributed the subcellular markov state ODE model to the work.

Chapter 2

Estimating the multi-well energy landscape of Tropomyosin on the actin thin filament using BrownDye

2.1 Abstract

In this study, we use Brownian dynamics to describe the activation process of the cardiac thin filament during contraction. The model is developed based on the fact that, when Ca^{2+} is available, tropomyosin (Tm) oscillates over the surface of actin filament in the azimuthal direction in order to regulate the access of myosin heads to actin binding sites. This dynamic motion is characterized by the existence of three distinct equilibrium positions, namely; blocked (B), closed (C), and open (M) regulatory states. The exact dynamics and energy landscape governing Tm motions between these B-C-M conformational states are not yet fully understood. The aim of this study is to use BrownDye simulations to estimate high and low energy positions for Tropomyosin (Tm) as it moves azithumally about the actin thin filament during sarcomere activation. The energy landscape calculated from these simulations can theoretically be used to inform the locations ϕ_{BC} and ϕ_{CM} in the stochastic ODE Tm simulations based on a multi-well energy landscape of Tm movement.

2.2 Introduction

Tropomyosin (Tm) is a coiled-coil regulatory protein that binds head-to-tail to the adjacent Tm molecules to form a continuous chain. This chain is constrained at a particular angular position (ϕ) slightly away from the surface of the actin filament by electrostatic forces. This setting allows Tm to oscillate in the azimuthal direction with respect to the actin's longitudinal axis. The dynamic motions of Tm over the surface of an actin filament are believed to play an important role in the process of striated thin filament activation and have been hypothesized to be a key effector in regulating muscle contraction [178, 179, 180, 181, 182, 183, 96, 184, 185, 186, 187, 188, 189, 190].

Two different hypothetical mechanisms have been proposed to describe Tm motions on the actin's surface. The sliding mechanism suggests that Tm translates over a relatively flat region and assumes that there are no major changes in the structural configurations of both Tm and actin [191, 192]. In contrast, the rolling hypothesis posits an axial rotation/deformation of the Tm-chain about its axis [193, 194]. In either motion scenario (sliding or rolling), the Tm chain undergoes distinct movements to uncover the myosin-S1 binding sites located on the surface of the actin filament. These motions are characterized by three equilibrium positions, namely: the blocked position "B" (binding sites are blocked), closed position "C" (weak binding is permissible), and the open position "M" (strong binding of S1). These maneuvers are set by a well-established mechanism, commonly known as the three-state- model (B-C-M) of McKillop and Geeves McKillop1993. While the three-state-model describes Tm's equilibrium regulatory states, the intrinsic mechanism by which the Tm chain oscillates between these states remains incompletely understood.

Tm is generally considered to be a flexible chain, as shown by several recent myofilament mechanistic models [195, 196, 197, 191, 198]. These models were developed based on the path-integral theory of a continuous flexible chain [199], which was used to derive a nonlinear elastic energy governing the Tm's azimuthal movements. In these models, a Monte

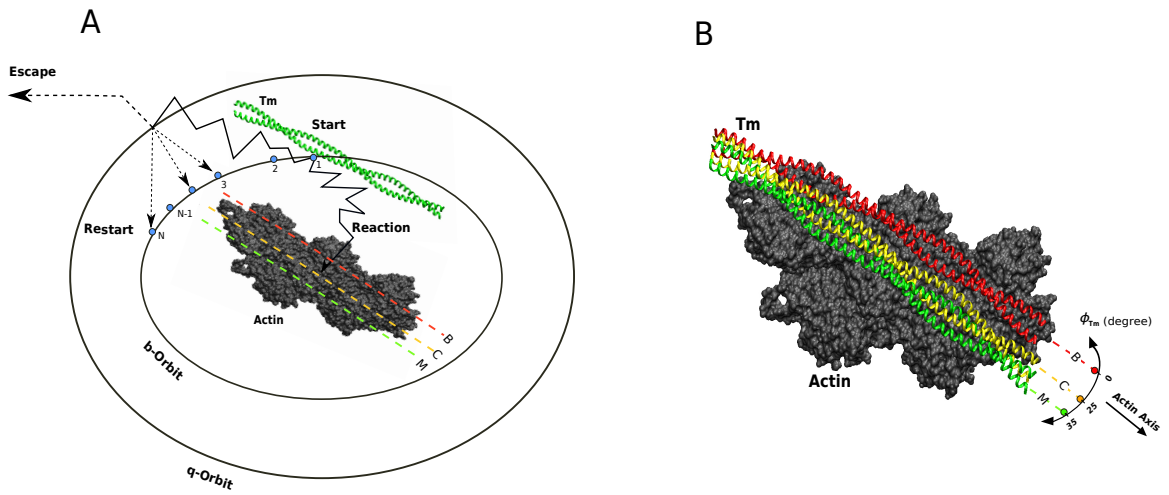

Figure 2.1. Brownian dynamics simulation setup to reconstruct the energy landscape profile of Tm azimuthal motions over actin surface. In panel A, we show our simulation setup with reaction (binding event) or escape of Tm-actin trajectories using the Browndye package developed by Huber and McCammon [162]. In panel B, we begin with PDB 4A7F structure positioned in the Tm open state (green ribbon) of approximately 35 degrees (using the closed Tm state as the 0 degree reference). The atomic structure of Tm was then rotated about the axis of the actin thin filament at -2 degree decrements up to the blocked state at 0 degrees (red ribbon). The actin structure is shown in grey, with an intermediate Tm structure shown at 25 degrees of rotation, corresponding to the closed state (yellow ribbon).

Carlo-based algorithm was used, and Tm was assumed to slide over actin, without rotating around its own axis, with an elastic energy dependent only on Tm's bending stiffness. These models have successfully predicted the angular positions spanned out by the Tm-chain and regulated by Ca^{+2} availability during the process of thin filament activation. However, their applicability in describing how Tm alternates between angular locations is limited, and they cannot be used to track the intrinsic Tm dynamic motions between regulatory positions.

2.3 Brownian dynamics methods

Brownian dynamics simulations using the BrownDye package [**?**] were used to calculate the second order association rate K_D $(1/M.s)$ between the Tm molecule and the actin filament as a function of the azimuthal angle ϕ. This is accomplished by generating one million

trajectories of interaction between a 272-residue Tm segment and a thin filament segment comprised of 5-actin monomers. The atomic structure used in the simulations was a crystallized actin-Tm-myosin complex in the rigor state (PDB: 4A7F), with myosins and ligands removed [192]. Using the visual molecular dynamics (VMD) tools [200], the Tm segment is rotated around the actin filament in the azimuthal direction at 2-degrees increments up to 36-degrees of rotation in order to cover the full range of Tm movements during thin filament activation. The initial configuration of the Tm-actin interactions that we used to run the Brownian dynamics simulations is shown in Figure 2.1A. We begin our simulation with the rigor state (PDB 4A7F) structure positioned nearby the Tm open state (M) at about 35-degrees. This atomic structure of the Tm is then rotated about the axis of the actin thin filament at -2 degree decrements up to the blocked (B) state, which is defined at an angle of about 0-degree. The actin structure is shown in grey, with an intermediate Tm structure given at 25-degrees of rotation, corresponding to the closed (C) state. The ribbon structures of the B-C-M states are rendered in red, yellow, and green respectively, as shown in Figure 2.1B.

The tropomyosin and actin structures were converted to PQR format using pdb2pqr and the Amber force field package [201, 202]. The APBS solver was then used to generate electrostatic potential grids for the structures at 300K [203]. A permittivity value of 4 was set for the solute, and 78.5 for the solvent, with a solvent ion concentration of 0.15 mM KCl corresponding to a Debye length of 7.86 . 1 million BrownDye trajectories were computed for each 2-degree rotation position.

2.4 Results: a multi-well energy landscape emerges from electrostatic studies

The electrostatic calculations for each actin-Tm configurations were obtained using ABPS software [164]. For instance, the electrostatic maps for both actin and Tm atomic structure in the open state is given in Figure 2.2. In particular, the electrostatic surface maps for

both actin and Tm atomic structures are given in panel A and B respectively. The green dotted line represents the locus of the Tm location over the actin surface with landmark points 1, 2, and 3 given to highlight the interaction locations of both actin and Tm in the open M-state.

In Figure 2.3A, using the Brownian dynamics simulations, we show the calculated second order association rate K_D for the Tm-actin complex as a function of the azimuthal angle ϕ at 5-different (12, 13.5, 15, 16.5, and 18) reaction distances that are measured from the actin surface. An association event was considered to occur when 3-polar contact pairs were within the reaction distance set. These reaction distances were considered in order to compare the K_D-ϕ profile at multiple distances, and because there is no experimental data available to provide exact rates of association between these molecules. Moreover, for each simulation, a set of contact atom pairs was generated to find likely hydrogen bonding pairs of atoms between the two molecules within 6 of each other. Between 1-2 million trajectories were performed for each Tm location. After completion of the trajectories, the ratio of association events to escape events was used to calculate a second order association rate. The results are then averaged and the standard errors of the mean are computed. The K_D-ϕ distribution has been found to exhibit multi extrema points that mimic the energetic barriers between the Tm transition states on the actin surface. The obtained rates are then used to reconstruct an approximate activation energy landscape $U_i^{a,BD}$ of the Tm-actin complex.

In Figure 2.3B, we show the reconstructed activation energy landscape of the Tm-actin complex as a function of the azimuthal angle (ϕ) using both Eyring's formulation and the association rate data computed using the Brownian dynamics simulation protocol mentioned previously. This energy profile is accomplished by estimating high and low energy barriers for Tm as it rotates around the actin thin filament during sarcomere activation. Clearly, the energy-angle distribution demonstrates a multi-well topology. For instance, there are two clear minima that are located roughly at angles ϕ = 3 and 26 degrees respectively. These two angles represent the stable Tm locations on the actin surface and correspond to the blocked (B) and

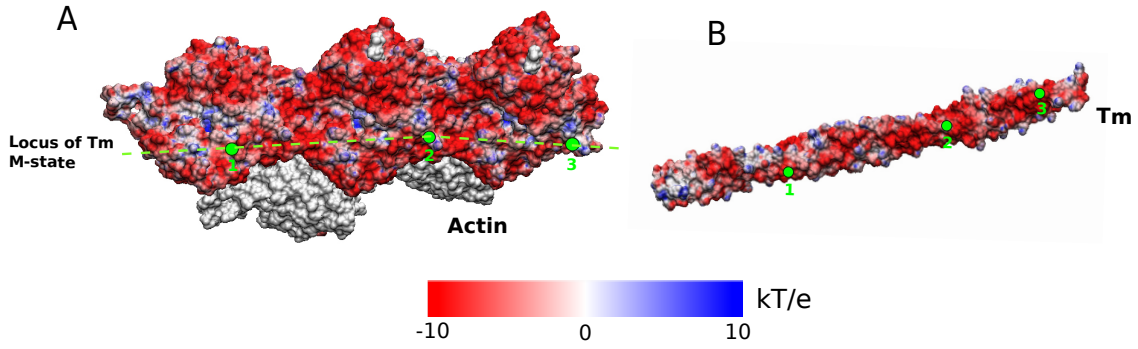

Figure 2.2. The electrostatic calculations that we initially used to run the Brownian dynamics simulations of the Tm motions on actin surface using the APBS package [203]. In panel A, we show the electrostatic surface map for the actin atomic structure. The surface coloring for the grey area is omitted for better visualization of the interacting side on the actin surface. In panel B, we show the electrostatic surface map for the Tm atomic structure. The green dotted line represents the locus of the Tm location over the actin surface with landmark points 1, 2, and 3 given to highlight the interaction locations of both actin and Tm in the open M-state corresponding to the original PDB crystal structure.

closed (C) states. The maxima points of the energy profile represent the unstable points and mark the transition barriers required for the Tm to undergo conformational changes. It should be noted that, although the crystal structure complex around the 35-degrees represents the rigor open state of Tm at full activation, this state is achieved through steric interactions with myosin-S1 heads in the physiological system. The computed energy profile does not show a clear minimum at this location. This is due to the lack of myosin-S1 head interactions considered in the Brownian dynamics simulations. However, the energy profile shows downward movement toward another stable point. The Brownian results of both the K_D and the $U_i^{a,BD}$ are then used to reconstruct activation energy profiles using both ϕ^4 and ϕ^6 polynomial functions to confirm the multi-well profile topology, as shown in Figure 2.3(B).

2.5 Discussion and future directions

This study reinforces the theory surrounding the multi-well energy landscape Tm navigates as it rotates about the actin thin filament. We are also offered insight about the

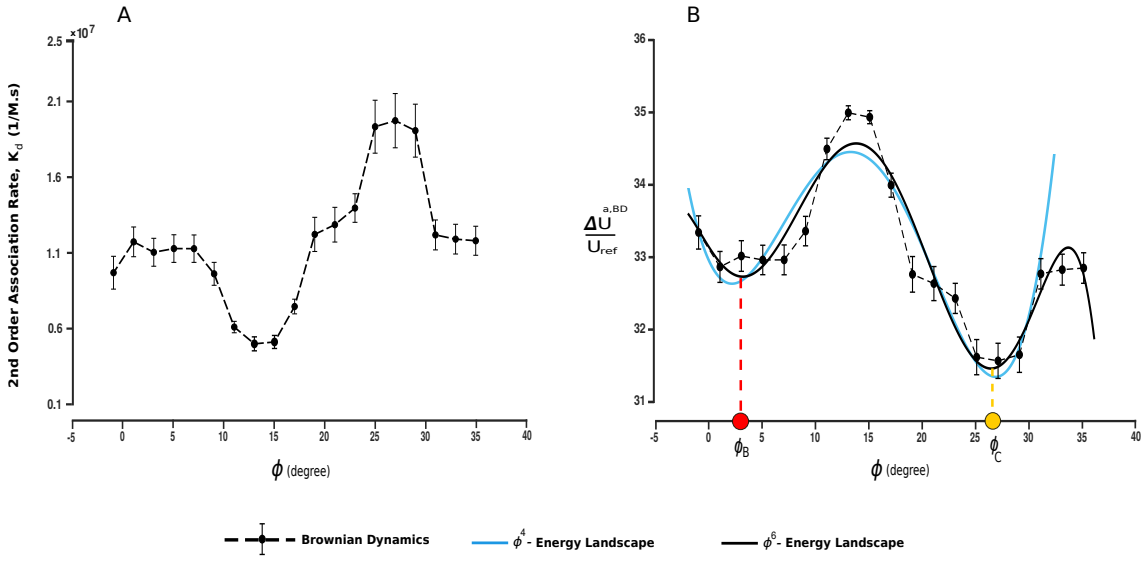

Figure 2.3. Estimating association rates and the multi-well energy landscape profile of Tm motion on the actin thin filament using BrownDye [162]. In panel A, we show the 2nd order association rates of Tm-actin complex at a 15 reaction distance as a function of the azimuthal positions of Tm on the actin filament. In panel B, we show the corresponding activation energy landscape profile calculated using Eyring formulation.

potential locations of high energy barrier points for the complex. The association rate landscape can be considered as the inverse of a general energy landscape for the Tm-actin complex in the absence of other associated sarcomeric molecules such as the troponin complex and the myosin S1 head. The angles associated with local maxima in the association rate landscape, 3 degrees and 26 degrees, closely match the documented positions of closed and blocked tropomyosin, respectively. At these positions, strong electrostatic interactions between Tm and actin lead to minima in the multi-well energy landscape for the system. The minima in the association rate landscape, corresponding with presumed maximum energy barriers, are observed at 35 degrees and 14 degrees. 35 degrees corresponds with the open Tm state, which has been found to be energetically unfavorable without a bound myosin S1 head to push Tm to this extreme angle [204]. The 14 degree position should correspond to ϕ_{BC}, the angle at which a high energy barrier exists between the blocked and closed states.

The use of Brownian dynamics to describe myofilament activation can potentially move the field of cardiac mechanics toward more detailed atomistic models of subcellular function, as we integrate Brownian ratchet theory into models of larger subcellular processes. Brownian motion is fundamental to current atomistic-level investigations in both coarse-graining and all-atom molecular dynamics simulations which have been used to provide biophysical detail of many thin filament proteins including Tm and the Tn complex [205, 94, 38, 206, 43, 96, 207, 208, 100, 101, 103, 104, 105]. In particular, Brownian dynamics models of the actual molecules, built up from structural information at the molecular level, would constitute the next level toward the molecular end of the hierarchy of models [209, 162]. Such models, even though more coarse-grained than a full molecular dynamics model which includes all atoms of the motor molecules and solvent, might be able to provide the shape of the energy landscape [210], the effective diffusivity along the reaction coordinate, and the degree of coupling among adjacent tropomyosin molecules. Furthermore, recent work on coupling Brownian dynamics with more detailed molecular dynamics simulations could be used to explore the activation due to the Ca^{+2} ions [211, 212].

The results offer insight about the potential locations of high energy barrier points for the complex. The association rate distribution as a function of the azimuthal angle is used to derive a generic energy landscape for the Tm-actin complex in the absence of other associated sarcomeric molecules such as the troponin complex and the myosin S1 head. The angles associated with the two local maxima in the association rate profile closely match the documented Tm positions in blocked and closed states, respectively. At these positions, strong electrostatic interactions between Tm and actin lead to minima in the multi-well energy landscape for the system. The locations of the minima in the association rate landscape mark the energy barriers between both states. The open Tm state has been found to be energetically unfavorable without a bound myosin S1 head to push Tm to this extreme angle [204]. The 12.5 degree position should correspond to ϕ_{BC}, the angle at which a high energy barrier exists

between the blocked and closed states.

It should be noted that, although the Brownian dynamics results show a multi-well energy profile, they don't demonstrate an energy minimum at the 35 degree Tm open state for the following reasons. Firstly, the myosin S1 is not included in the Brownian dynamics simulation and hence does not interact with the complex. We however hypothesize that bound myosin in the crossbridge binding site on the actin thin filament would greatly increase the energetic favorability of the open state, while minimizing association rates for all other positions. Secondly, we do not consider the case of low cytosolic Ca^{2+}, in which the troponin complex sterically hinders Tm from moving out of the blocked state. In this case, one can assume the lowest energy well would exist at around zero degrees, with all other states becoming less favorable. Finally, this model considers a portion of Tm which excludes the Tm-Tm overlap region, which makes it impossible to consider the documented effects of nearest-neighbor interactions on the energy landscape. A more generic multi-well energy landscape (ϕ_6-potential) is derived based on the results obtained from the Brownian dynamics simulations. The model accounted for the fact that Tm must move between B-C-M equilibrium angles and considered variations in Ca^{2+} and Tm-Tm coupling which impact the critical angles ϕ_{BC} and ϕ_{CM} that outline the energy barriers between the staple states.

2.6 Acknowledgements

Chapter 2 contains excerpts of material as it appears in Aboelkassem Y, McCabe KJ, Huber G, Regnier M, McCammon JA, McCulloch AD (2019) "A Coarse-Grained Multiscale Model of Thin Filament Activation using Brownian and Langevin Dynamics". Biophysical Journal. *(Submitted)*. The dissertation author was a contributing author on this publication, but her specific contributions are the only elements contained herein.

Chapter 3

Electrostatic Analysis of myosin-actin interactions in the presence of ADP or 2-deoxy-ADP

3.1 Abstract

The naturally occurring nucleotide 2-deoxy-ATP (dATP) can be used by cardiac muscle myosin as an alternative energy substrate. We, and others, have previously shown that dATP increases contractile force and myosin cycling rates in both failing and nonfailing hearts, but the structural basis of these effects has remained unresolved. In this work, we use computational approaches to investigate the structural basis of force augmentation by dATP in cardiac muscle, from the single-myosin level to the sarcomere level. Using Brownian dynamics simulation and computational structural analysis, we find that the deoxy-hydrolysis products (dADP and Pi) bound to pre-powerstroke myosin induce an allosteric effect that restructures the actin-binding surface on myosin and increases the rate of cross-bridge formation. We then show that this predicted effect translates into increased electrostatic interactions between actin and cardiac myosin. Thus, electrostatic restructuring of myosin by dATP actuates the resting sarcomere to potentiate cross-bridge formation upon activation, leading to force augmentation in cardiac muscle. The structural alterations in myosin induced by dATP may provide insight into the design or selection of small molecules to be developed as therapeutic agents to treat heart failure.

3.2 Introduction

Heart failure (HF) is a chronic progressive condition in which the heart is unable to efficiently pump blood throughout the body, and it is a significant and growing medical challenge. Current treatments only slow progression of HF and do not rescue cardiac muscle function. Consequently, there is a pressing need for novel therapeutic interventions that enhance cardiac contractility in failing hearts.

Cardiac muscle contraction is generated at the molecular level by cyclical, ATP-driven actin-myosin interactions, making myosin an appealing therapeutic target for treating ventricular systolic dysfunction. As such, there are several myosin-specific small molecule compounds currently being developed and tested to treat HF. One is the naturally occurring ATP analogue 2-deoxy-ATP (denoted dATP). We have previously demonstrated that dATP can be used by cardiac myosin in place of ATP as the substrate that fuels actin-myosin cross-bridge cycling [66]. Moreover, we have shown that dATP increases contractility in rat myocardium [66], improves left ventricular function in a porcine model of myocardial infarction [78], and increases contractility of ventricular muscle from patients in human end-stage heart failure [71].

Chemo-mechanical studies suggest that the dATP-mediated force augmentation occurs by increasing cross-bridge binding and cycling rates [67, 213, 214, 215], but a precise structural explanation for this is lacking. A recent computational study using molecular dynamics simulations suggests that dATP behaves as an allosteric effector of pre-powerstroke myosin, such that when dADP.Pi is in the nucleotide binding pocket, local structural changes lead to exposure of more positively charged residues on the actin binding surface of myosin compared with ADP.Pi [79]. This led us to hypothesize that dATP increases electrostatic interactions between cardiac myosin and actin, and that this should result in: (i) a destabilization of the resting conformation of myosin in the cardiac sarcomere, and (ii) prime myosin for binding to actin to increase cross-bridge formation during activation.

To test these hypotheses, we used a molecular computational approach. Atomically detailed structural models of pre-powerstroke myosin-ADP, myosin-dADP, and actin were used to investigate how each nucleotide affects the steric orientation of the actin-myosin binding surface and the energetics associated with the actin-myosin complex. Brownian dynamics (BD) simulations [using Browndye software [162]] of myosin binding to actin were then used to predict actin-myosin electrostatic contact pairs and binding kinetics. BD simulations suggested an increased number of electrostatic binding interactions between opposite charges on myosin and actin and predicted highly non-linearly increased rates of binding as the distance of myosin from actin is reduced. The computational approach used in this study suggests a molecular mechanism for enhanced myosin-actin cross-bridge binding with dATP in cardiac muscle that can explain the observed increased contraction of myofibrils, myocytes, and tissue and the enhanced ventricular function.

3.3 Methods

3.3.1 Brownian Dynamics simulations

Simulations were performed using Browndye software to determine the differences between ATP- and dATP-bound myosin in terms of actin association [162]. A previous Molecular Dynamics study on pre-powerstroke myosin (PDB: 1VOM) yielded the starting structures for our myosin rigid bodies [79]. PDB files for Run 1 of the MD simulations at the 50,000 ps timepoint with only protein present (no ligands) were used for both ADP-bound and dADP-bound myosin. An actin monomer (PDB: 2ZWH) with all ligands removed was used to represent the thin filament to avoid electrostatic interactions with other binding sites along the filament [216]. The actin and myosin-ADP structures were manually aligned using Visual Molecular Dynamics (VMD) to ensure that the myosin binding cleft on actin was appropriately oriented with the binding domain on myosin [200]. To ensure the accuracy of the bound conformation, the actin monomer was twice aligned with Chain B of PDB:5KG8 (rigor myosin

X co-complexed with actin) to create a dimer which more accurately represented the interaction between myosin and the thin filament, and the myosin structures were aligned with chain A of the same PDB structure [217]. The dADP-myosin and ADP-myosin structures were aligned to an identical structure using VMD to ensure that the simulations are fully comparable.

PQR files were generated for all structures using PDB2PQR [163]. Electrostatic potential grids were generated using APBS version 1.4 by solving the Poisson-Boltzmann equation using the Amber force field at 300K [164]. A relative permittivity of 4 was used for the solute, and 78.5 for the solvent, and a 150 mM concentration of KCl was assumed for the system. A list of polar complex pairs (defined as contact pairs) was generated by comparing the myosin and actin input coordinates and considering pairs of atoms within 3.5 Åof each other, and the complete list of contact pairs can be found in associated files. A total of 49 atom pairs met the criteria for the ADP case, and 66 atom pairs met the criteria for the dADP case. A simulation trajectory was considered successful when at least 3 polar contact pairs were within the prescribed reaction distance criterion, and association rates were determined by using the ratio of successful to unsuccessful trajectories together with the assumed diffusivity of the molecules [218]. Specifically, the association rate constant (kon) is calculated as

$$k_{on} = s * k_{db} * (a/n) \tag{3.1}$$

where s is a scaling factor, a is the number of binding events, n is the total number of trajectories, and k_{db} is the rate constant of diffusion as calculated using the Smoluchowski equation (i.e., the diffusion-limited case) using information about the molecule charges and solvent [218]. The reaction distance criterion was varied to examine a large range of possible rates since experimental association rate data for this system are unavailable. 500,000 trajectories were performed to calculate the average association rates for both the ADP and dADP case to decrease the width of the binomial rate distribution and increase confidence in the rate calculations.

3.3.2 Energetic calculations for an actin-myosin complex

Energies were calculated for the bound actin-myosin complex using Amber 18 [219]. From the PDB file containing both actin and myosin, parameter/topology (prmtop) and coordinate/restart (inpcrd) files were created using tleap (a program within the AMBER suite that generates topology files from predetermined coordinate files) and amber protein forcefield ff14SB [220]. Initially, the total energy was calculated in PMEMD (Particle Mesh Ewald Molecular Dynamics) using thermodynamic integration (ADP-Myosin: $-2.96 * 10^4 kcal * mol^{-1}$, dADP-Myosin: $-3.2075 * 10^4 kcal * mol^{-1}$). To ensure that atom overlap was not incorrectly affecting energy calculations, 20,000 minimization steps were performed on the system using PMEMD. Minimization had little effect on the energetic calculations - after minimization, energied were calculated as ADP-Myosin: $-3.05 * 10^4 kcal * mol^{-1}$ for ADP-myosin and $-3.25 * 10^4 kcal * mol^{-1}$ for dADP-Myosin.

3.4 Results - Electrostatic restructuring of the actin-myosin interface via dADP.Pi leads to increased binding kinetics

In pre-powerstroke myosin, dADP.Pi allosterically affects myosin, resulting in a structural rearrangement of the nucleotide binding pocket that translates to an altered actin-binding region of myosin [see Ref [79]]. However, the effects of the altered actin-binding region of myosin by dADP.Pi on the actin-myosin association kinetics and energetics remained unknown. Here, we used atomically detailed structural representations of actin and myosin to investigate how either dADP.Pi or ADP.Pi (represented as dADP or ADP hereafter) bound to pre-powerstroke myosin affects: (i) the steric orientation of the actin-myosin interface, (ii) the electrostatic potential of the actin-myosin complex, and (iii) the actin-myosin binding kinetics. Figure 3.1A shows the bound conformation of the actin-myosin complex, with myosin-ADP in red, myosin-dADP in blue, and an actin monomer in green. With dADP bound to myosin, there

is a significant increase in the number of residue "contact pairs (defined as being < 3.5 Åapart) compared to myosin-ADP (66 pairs for dADP compared to 49 for the ADP case). Figure 3.1B depicts the various residue interactions for actin and the actin-binding surface of myosin-ADP (black lines) or myosin-dADP (blue lines), where the thickness of the lines corresponds to the number of atoms in contact between the two residues. The diagram highlights the increased actin-myosin interactions in the dADP case via the myosin polar residues ASN 541, LYS 546, HIS 548 and 550, and SER 549 and 552. Moreover, for myosin-dADP, more atomic contact pairs are associated with Serine, Lysine, and Histidine (Fig. 3.1C).

Bringing more polar residues on myosin into the actin-myosin interaction likely increases the number of hydrogen bonds between myosin and actin, leading to a more stable complex formation. Consistent with this, upon calculating the electrostatic potential (free energy) of the actin-myosin complex for each nucleotide case, we found that the electrostatic potential associated with the actin-myosin protein complex is approximately 8% lower with dADP bound to myosin compared to ADP ($-3.21 * 10^4 kcal * mol^{-1}$ versus $-2.96 * 10^4 kcal * mol^{-1}$, respectively). Thus, our computational structural analysis [combined with our previous study [79]] predicts that dADP acts as an allosteric myosin effector to directly increase the number of polar interactions between actin and myosin, thereby increasing the electrostatic affinity of myosin for actin. Specifically, we propose that interactions formed by ADP and dADP within the nucleotide binding pocket allosterically result in distinct actin-binding site conformations by altering the dynamics of the switch 1 loop [79].

Based on these results, we hypothesized that increased electrostatic interactions between actin and myosin-dADP will increase the actin-myosin association kinetics. However, given the extremely rapid kinetics of weak cross-bridge binding, it is very difficult to measure the association rates experimentally. Thus, we employed a robust set of Brownian dynamics (BD) simulations to estimate 2nd order bi-molecular association rates for actin-myosin complex with either dADP or ADP bound in the nucleotide binding pocket of myosin. Association

Table 3.1. Second-order bi-molecular association rate constants for myosin-ADP or myosin-dADP binding with an actin dimer. Rate constants were determined by Brownian dynamics simulations. For each nucleotide, as the reaction distance criteria decreases, the on-rate increases nonlinearly. However, the on-rate for dADP-myosin to the actin dimer is consistently greater compared to ADP-myosin for all reaction distance criteria, with the greatest fold change in the 1.2-2.5 nm range. This strongly supports the notion of an increased electrostatic affinity between actin and myosin induced by dADP.

	Actin-Myosin on-rates ($\mu M^{-1} * s^{-1}$)		
Reaction distance criteria (nm)	Myosin-ADP	Myosin-dADP	Fold Change
0.7	0.42	0.82	1.9
0.8	1.66	4.18	2.5
1.0	8.02	22.02	2.7
1.2	21.37	76.84	3.6
2.5	403.10	1431.73	3.6
5.0	3198.05	4460.93	1.4

rates between actin and ADP-bound or dADP-bound myosin were determined for a wide range of "reaction distance criteria, defined as the minimum separation distance between specified atomic contact pairs (as defined above) in the actin- myosin complex required to reach before a reaction was considered to have occurred. We simulated binding of myosin to an actin dimer (500,000 independent trajectories) rather than an actin monomer (as shown in Fig. 3.1A) to provide a more realistic landscape of myosin binding with F-actin while maintaining computational efficiency. Intuitively, association rates are predicted to increase with increased reaction distance criteria for either nucleotide (Table 3.1). Furthermore, as we hypothesized, myosin-dADP is predicted to have a higher association rate with actin compared to myosin-ADP, with the greatest fold-change occurring in the range of reaction distance criteria of 1.2 to 2.5 nm (Table 3.1). This is likely due to the allosteric response of pre-powerstroke myosin to dADP [Ref [79]] that leads to a more positively charged binding surface of myosin-dADP in the loop 2 region [79] and increased polar hydrogen bonding interactions (Fig. 3.1), which together contribute to a greater electrostatic affinity between actin and myosin and faster association kinetics.

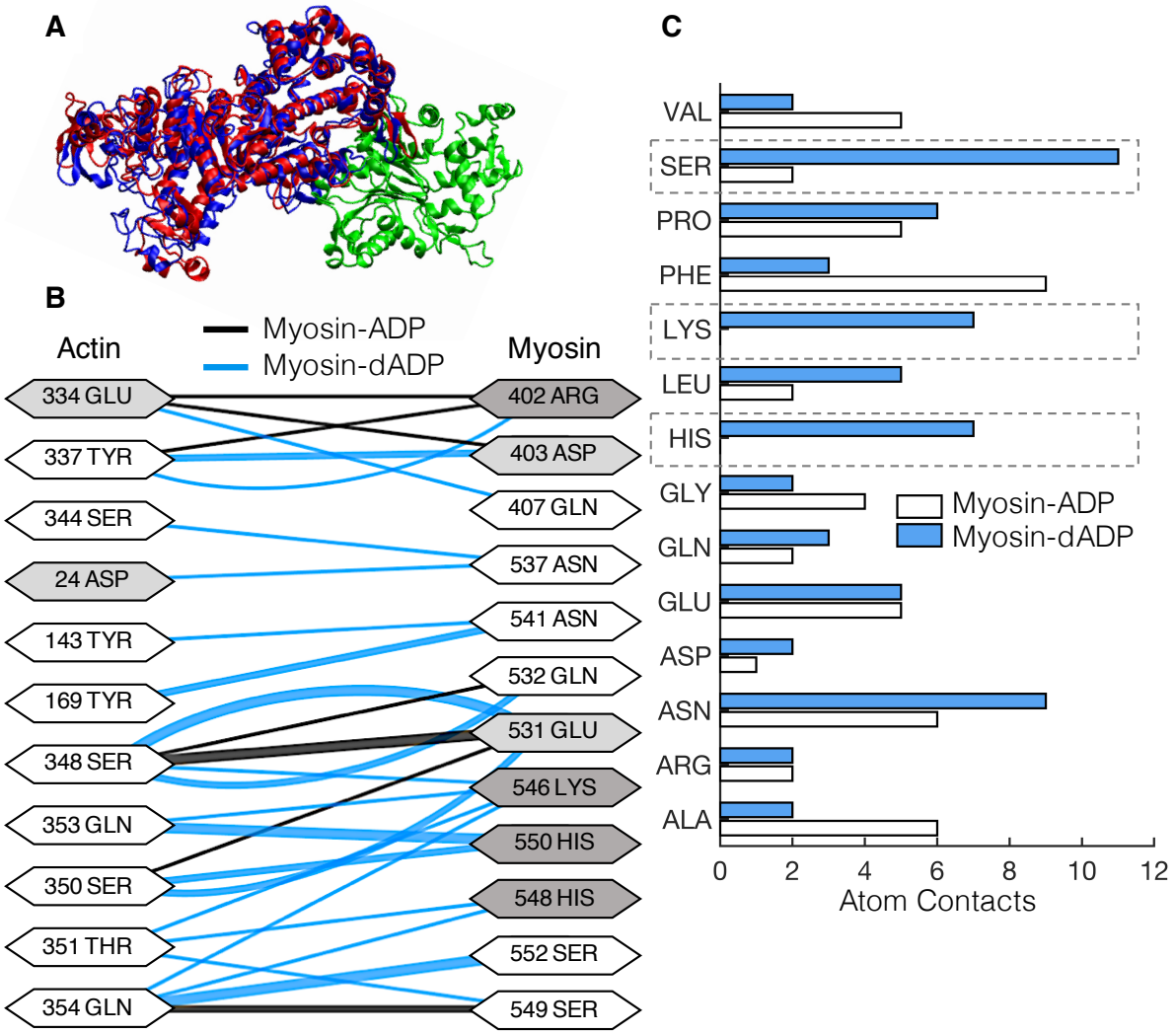

Figure 3.1. dADP acts as an allosteric myosin effector to promote polar interactions between actin and pre-powerstroke myosin. (A) An actin monomer (green) and either ADP-bound (red) or dADP-bound (blue) myosin S1 segments. (B) Contact pairs of residues between actin and ADP-bound myosin (black lines) and dADP-bound myosin (blue lines) for an actin-myosin complex. The thickness of the line connecting the interacting residues corresponds to the number of atoms in contact between the residues, and the shading of the residue indicates whether it is polar (white), acidic (light gray), or basic (dark gray). (C) Number of atoms in contact (see main text) between actin and myosin-ADP (white bars) and myosin-dADP (blue bars) in a pre-powerstroke actin-myosin protein complex. There are significant increases in atom contacts that consist of polar residues (SER, LYS, and HIS; highlighted by dashed boxes) between actin and myosin-dADP compared to actin and myosin-ADP.

3.5 Discussion

A structural basis of dATP-mediated force augmentation in cardiac musclefrom single molecules to the sarcomere. Previous work by our group and others has demonstrated that the naturally occurring nucleotide 2-deoxy-ATP (dATP) can serve as an alternative energy substrate by cardiac myosin, that promotes cross-bridge formation and increases cycling rates [66, 67, 221]. Our goal in this study was to understand the structural basis of the effects of dATP on myosin molecules and myofilament ultrastructure in resting and activated cardiac muscle that underlie changes in actin-myosin cycling and cardiac function. Our approach included single-molecule and protein biochemistry. Our combined results suggest that the augmentation of force by dATP is precipitated by a dATP-induced allosteric effect that disrupts the resting conformation of myosin motors and increases its electrostatic interactions with actin in the sarcomere. Our BD simulations of the bi-molecular association of an actin monomer with either ADP- or dADP-bound myosin predict that dADP significantly increases the association rate compared with ADP. We attribute this to a dADP-induced conformational change of the actin-binding surface of myosin that exposes more positively charged and polar residues (Fig. 3.1), effectively increasing its electrostatic affinity for actin. This type of structural analysis provides a unique picture of the functional mechanisms of small molecule-based force augmentation in cardiac muscle in the context of potential systolic heart failure treatments.

It is important to note that there are limitations to the simplified BD studies performed here. Firstly, the system was assumed to consist of a free-floating myosin S1 head diffusing near a free-floating actin dimer. In the sarcomere, however, the myosin S1 head is tethered to the thick filament and actin is polymerized into F-actin to form the thin filament, restricting the mobility of each protein relative to one another. The simplifications of the model were chosen to optimize computational efficiency while still elucidating nucleotide-based effects on binding rates. Additionally, enthalpic force calculations included multipole information up to the dipole level as calculated from electrostatic grids using the Adaptive Poisson-Boltzmann

Solver (APBS), but the software uses an implicit solvent to maintain computational feasibility which affects the overall calculation of electrostatic energies. Therefore, the rates we report here should be considered evidence of qualitative (or pseudo-quantitative) increases in actin-myosin binding due to the presence of dATP rather than exact calculations, and actual rates are likely to be lower.

3.6 Acknowledgements

Chapter 3 contains excerpts of material as it appears in: Powers JD, Yuan C, McCabe KJ, Murray JD, Childers MC, Flint GV, Moussavi-Harami F, Mohran S, Castillo R, Zuzek C, Ma W, Daggett V, McCulloch AD, Irving TC, Regnier M. (2019) "Cardiac myosin activation with 2-deoxy-ATP: A charged affair". PNAS. *(In Press).* The dissertation author was a contributing author on this publication, but her specific contributions are the only elements contained herein.

Chapter 4

Predicting the effects of dATP on cardiac contraction using a Monte Carlo Markov State Model of the sarcomere

4.1 Abstract

2-deoxy-ATP (dATP) is a naturally occurring homolog of ATP that has shown promise as a therapeutic because it significantly increases cardiac myocyte force development even at low dATP/ATP ratios. To investigate mechanisms by which dATP alters myosin crossbridge dynamics, we used Brownian dynamics simulations to calculate association rates between actin and ADP- or dADP-bound myosin that were then incorporated in a mechanistic Monte Carlo Markov State model of cooperative sarcomere contraction. A unique combination of increases to myosin attachment, powerstroke, and detachment rates was required to match experimental steady-state and kinetic data for dATP force production in rat cardiac myocytes when the model was constrained by the Brownian dynamics model of myosin binding to an actin dimer. We also discovered that nearest-neighbor cooperativity contributes to, but does not fully explain, the nonlinear relationship between dATP/ATP ratio on the steady-state force-[Ca^{2+}] relation. Dynamic twitch simulations performed using experimental calcium transients as inputs suggest that myofilament effects of dATP alone are not sufficient to explain experimental observations of improved relaxation kinetics during dATP treatment, suggesting that dATP may also affect sarcoendoplasmic reticulum Ca^{2+}-ATPase activity even at low concentrations. By enabling the effects of dATP on sarcomere mechanics to be quantified, this novel multi-scale model may serve as a new platform for understanding the mechanisms of molecular therapeutics for cardiac contractile dysfunction.

4.2 Introduction

2-deoxy-ATP (dATP) is a small molecule which is present in most cell types due to its primary role as a building block of DNA. When dATP replaces ATP in cardiomyocytes, it has been shown to increase force production, enhance crossbridge cycling speed, and accelerate the removal of Ca^{2+} from the cytosol during cell relaxation [66, 73, 74]. It has also been found that, at low ratios of dATP to ATP, large nonlinear increases in force are observed at physiological Ca^{2+} concentrations [69]. Therefore, upregulation of dATP in cardiac cells *via* adenoviral-mediated gene transfection of Ribonucleotide Reductase (R1R2) has been studied as a potential treatment for heart failure [76, 78]. A variety of *in-vitro* and animal studies have demonstrated efficacy and safety of modest increases of dATP as a treatment, but further study is needed to resolve the specific molecular mechanics by which dATP augments cardiac myocyte contraction [222].

dATP has been studied experimentally in skinned myofibrils, cells, and mouse models, but the specific combination of mechanisms by which dATP improves contractility is not yet known. Hypothesized mechanisms of deoxy-ADP and -ATP include altered: (1) nucleoside triphosphate-myosin affinity; (2) acto-myosin affinity; (3) phosphate release from myosin; and (4) nucleoside disphosphate release from post-powerstroke myosin [74, 79]. Current experimental methods do not allow each of these mechanisms to be probed individually owing to their small spatial and temporal scales and coupled reactions. Multiscale computational models are needed to integrate heterogeneous experimental data. A variety of model paradigms have been used to simulate the contractile biophysics of the sarcomere [42, 223, 45]. There are three properties that we consider to be important for understanding the effects of dATP on force development that should be integrated into a model: spatial thin filament cooperativity; explicit tracking of ATP throughout the crossbridge cycle; and competitive binding of ATP and dATP at different ratios.

Here we present a novel model of thin filament activation and crossbridge cycling to

address three mechanistic questions about the effects of dATP on cardiac contractility: (1) To what degree are crossbridge cycling rates altered when myosin binds dATP rather than ATP? (2) Is the significant effect of dATP on steady-state force development at surprisingly low ratios of dATP:ATP a result of nearest-neighbor cooperativity, or other factors? (3) How do altered crossbridge cycling rates with dATP treatment result in faster twitch relaxation kinetics? To constrain and inform parameter estimation, atomistic Brownian dynamics simulations were used to estimate attachment rates of myosin binding to actin. These predictions permitted a unique combination of powerstroke and detachment rate parameters to be found that best match published steady-state and dynamic experimental measurements. The analysis shows that nearest-neighbor interactions between regulatory units along the thin filament likely contributed to the significant increases in steady-state force outputs at low fractions of dATP, but did not fully explain experimental measurements. We also concluded that observed alterations in twitch kinetics during dATP treatment are likely to depend, in part, on additional effects of dATP on the intracellular calcium transient.

4.3 Methods

4.3.1 Model Description

We constructed a Monte Carlo Markov Chain (MCMC) model of thin filament activation and crossbridge cycling which are based on the integration of two existing Monte Carlo models of the sarcomere [42, 224]. The model has a total of five states at each of 26 regulatory units (RUs) spaced evenly in one spatial dimension over time. Each RU consists of seven actin monomers, the troponin (Tn) complex, one tropomyosin (Tm) molecule, and the nearest available myosin S1 head. We assume that only one crossbridge (XB) may bind a single thin filament RU at a time as in earlier iterations of the model [116, 42].

The model assumes five possible conformational states an RU may occupy: State 1 (*B0*) in which the Tm molecule is fully covering the myosin binding site on the actin thin filament,

constituting the "Blocked" state. Rates k_{Ca}^{+} and k_{Ca}^{-} govern the transition to state 2 (*B1*) in which Ca^{2+} has bound to the Tn complex on the thin filament, allowing for a conformational change in Tn that allows Tm more flexibility. Rates k_{B}^{+} and k_{B}^{-} govern the transition to state 3 (*C*) in which Tm moves 25 degrees azithumally into the "Closed" position on the thin filament, partially exposing the myosin binding site. The nearest myosin S1 head is detached from the thin filament. Rates f^{+} and f^{-} govern the transition to state 4 (*Ma*) in which myosin is bound to the thin filament, sliding Tm an additional 10 degrees into the "Open" state. The XB is in the pre-powerstroke state and does not produce force. Myosin is bound to ADP and Pi. Rates k_{P}^{+} and k_{P}^{-} govern the transition to state 5 (*Mb*) in which the XB is bound and in the post-powerstroke, force producing state, after Pi release. Finally, rates g^{+} and g^{-} allow RUs to transition back to the *C* state concurrently with ADP release and either repeat the XB cycle or relax (Figure 4.1).

4.3.2 Thin filament activation kinetics and cooperativity

Thin filament cooperativity was introduced into the model in the same was as previously [42, 116]. Briefly, we begin with the Gibbs relation to calculate an equilibrium constant K_{BC}^{ref} between states *B* and *C*, in the case where both neighboring RUs are in the *C* state:

$$K_{BC}^{ref} = exp\frac{-\Delta G_{B\leftrightarrow C}^{ref}}{RT} \tag{4.1}$$

In the case where the nearest neighbors are in a state other than *C*, the transition to the *C* state will become less probable due to steric hindrance and Tm overlap. We represent the additional energy barriers due to the positions of nearest-neighbor Tm molecules, where *X* and *Y* represent the left and right neighbors, respectively, as:

$$\Delta G_{BC}^{XY} = \Delta G_{BC}^{ref} + \Delta G_{BC}^{X} + \Delta G_{BC}^{Y} \tag{4.2}$$

Therefore the equilibrium constant *K* for the transition from Blocked to Closed with

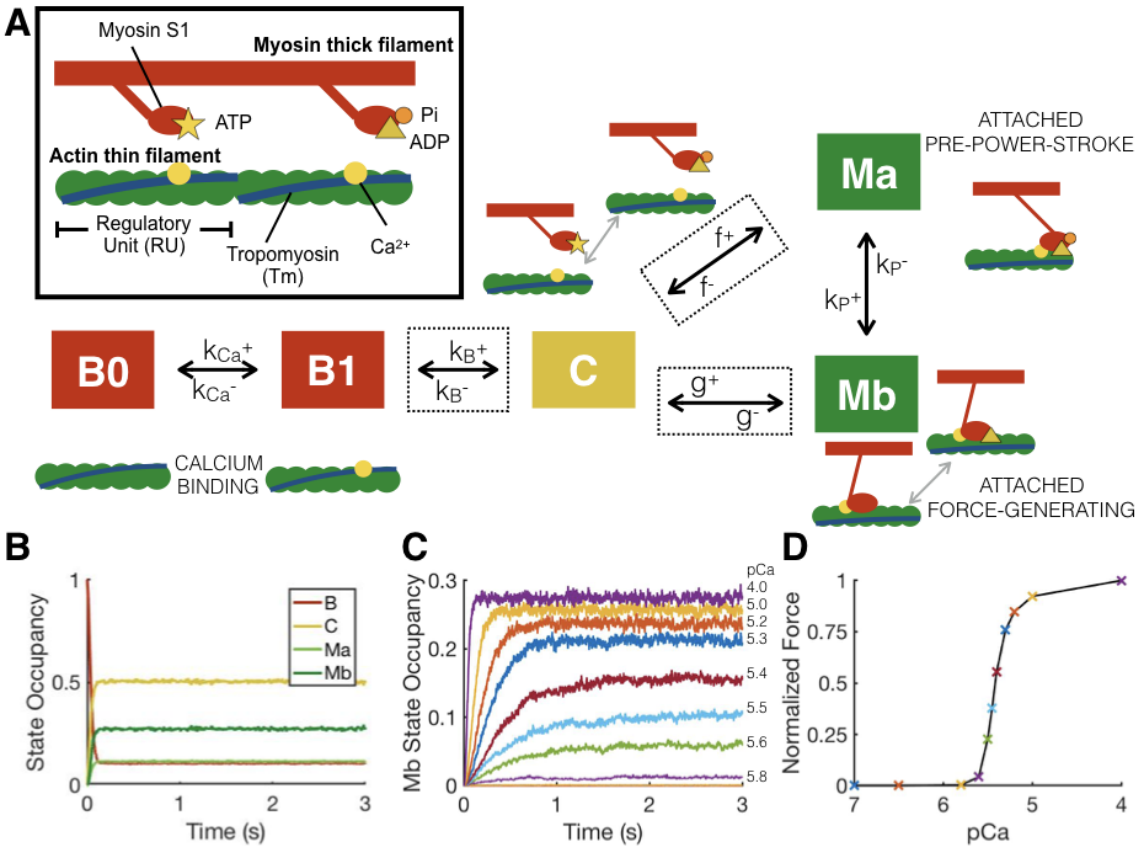

Figure 4.1. (A) Schematic outlining the 5 main states of the Monte Carlo Markov State model. States B0 and B1 (red boxes) represent the blocked state of Tm, where 0 represents no Ca^{2+} bound and 1 represents bound Ca^{2+}. The C state (yellow box) represents a 25 degree azithumal shift in Tm around the actin filament to comprise the closed state. The green boxes represent the two states where Tm is in the Open state, a 35 degree total shift from the blocked state. Ma represents the pre-powerstroke attached myosin position, and Mb represents the post-powerstroke force producing condition. Transitions from Blocked to Closed to Open states are affected by nearest-neighbor Tm interactions, which is signified by the dotted lines surrounding the transition arrows. (B) For a single steady-State simulation, 1032 3-second timecourses are run and averaged at each pCa value being tested and occupancy of each state is tracked. (C) Mb state occupancy is considered to be directly related to overall force production. The steady-state Mb occupancy at each pCa value is calculated by averaging the final 0.5 s of the simulation. (D) Steady state values of force are normalized to the pCa 4.0 force output and plotted as a function of pCa.

left and right neighbors in states X and Y, is calculated as

$$K_{BC}^{XY} = \gamma(XY)K_{BC}^{ref} \tag{4.3}$$

As we derived previously [42], the cooperativity coefficients for all possible combinations of neighbor states are:

$$\gamma(XY) = \gamma(YX) = \begin{cases} \gamma_B^{-2} & B,B \\ \gamma_B^{-1} & B,C \\ \gamma_B^{-1}\gamma_M & B,M \\ 1 & C,C \\ \gamma_M & C,M \\ \gamma_M^2 & M,M \end{cases} \tag{4.4}$$

where

$$\gamma_B = (exp\frac{-\Delta G_{B\to C}^{B}}{RT})^{-1} \tag{4.5}$$

and

$$\gamma_M = exp\frac{-\Delta G_{B\to C}^{M}}{RT} \tag{4.6}$$

Essentially, γ_B represents the cooperative impact of a neighboring blocked RU which tends to pull nearby RUs into the B state from the C state when γ_B ¿ 1. γ_M then represents the impact of neighboring RUs on the M state, which would facilitate the movement from B to C (and therefore toward the M state) if the value of γ_M ¿ 1.

Coefficient q, which determines the weight of cooperative coefficient γ toward forward and reverse rates were set to $q = 1$ for all simulations, where q factors into dynamic simulations

as:

$$k_{b+}^{XY} = k_{b+}^{ref} \gamma(XY)^{q} \tag{4.7}$$

$$k_{b-}^{XY} = k_{b-}^{ref} \gamma(XY)^{(q-1)} \tag{4.8}$$

The calcium binding step is not considered to be a cooperative process, and rates are calculated as:

$$k_{Ca}^{+} = k_{Ca}^{+ref} * [Ca^{2+}] \tag{4.9}$$

$$k_{Ca}^{-} = k_{Ca}^{-ref} \tag{4.10}$$

4.3.3 Crossbridge Cycling Kinetics

As described in previous studies [224, 58], the free energy of each crossbridge cycling state is defined as a function of XB distortion:

$$G_C = 0 \tag{4.11}$$

$$G_{Ma} = \alpha \Delta G + k_{XB,RT}(x - x_{b0})^2 \tag{4.12}$$

$$G_{Mb} = \eta \Delta G + k_{XB,RT} x^2 \tag{4.13}$$

Where constants $\alpha = 0.28$ and $\eta = 0.68$ as set in the original model [224]. XB distortion in the *Ma* state was considered to be 0, which simplifies the free energy profile for state *Ma* to $G_{Ma} = \alpha \Delta G$. Additionally, XB distortion in the *Mb* state was assumed to be 7.5 nm in all cases, an additional simplification from the original model. ΔG was determined as a function of concentrations of ATP, ADP, and Pi which were assumed to be constant for our

system:

$$\Delta G = \Delta G_{ATP} - ln(\frac{[ATP]}{[ADP][Pi]}) \tag{4.14}$$

where [ATP] and [Pi] = 3e3 uM, [ADP] = 30 uM, and ΔG_{ATP} = 13 RT.

In order to maintain detailed balance, reverse rates r_{ji} for XB transitions were calculated from forward rates r_{ij} through the following relationship :

$$\frac{r_{x,ij}(x)}{r_{x,ji}(x)} = e^{G_i(x) - G_j(x)} \tag{4.15}$$

where i is the initial state and j is the final state for a given transition. For example, to determine the reverse powerstroke rate, k_P^-, which represents the transition from the Mb state back to the Ma state,

$$k_P^- = \frac{k_P^+}{e^{G_{Ma}(x) - G_{Mb}(x)}} \tag{4.16}$$

As in the case of the B to C transition, the C to M transition is affected by nearest neighbor interactions due to the presence of myosin heads pushing the Tm molecule an additional 10 degrees around the filament. To represent the nearest neighbor interactions present in the C to Ma transition as well as the C to Mb transition, the equilibrium constant for the transition from Closed to Open is

$$K_C M^{XY} = \mu(XY) K_C M^{ref} \tag{4.17}$$

and the coefficients $\mu(XY)$ are:

$$\mu(XY) = \mu(YX) = \begin{cases} \mu_B^{-2} & \text{B,B} \\ \mu_B^{-1} & \text{B,C} \\ \mu_B^{-1}\mu_M & \text{B,M} \\ 1 & \text{C,C} \\ \mu_M & \text{C,M} \\ \mu_M^2 & \text{M,M} \end{cases} \tag{4.18}$$

The coefficients r that determines the weight of cooperative coefficient μ toward M or C states were set to 0.5 for all simulations, where r enters into dynamic simulations as:

$$f^{+XY} = f^{+ref}\mu(XY)^r \tag{4.19}$$

$$f^{-XY} = f^{-ref}\mu(XY)^{(r-1)} \tag{4.20}$$

$$g^{+XY} = g^{+ref}\mu(XY)^{(r-1)} \tag{4.21}$$

$$g^{-XY} = g^{-ref}\mu(XY)^r \tag{4.22}$$

4.3.4 Monte Carlo Methods and Optimization

The model was simulated in time using Monte Carlo methods and implemented for fast execution on a GPU in CUDA. The probability of a given transition p_{ij} at a given time step was calculated as:

$$p_{ij} = r_{ij}\Delta t \tag{4.23}$$

where r_{ij} is the reaction rate considering the state of the left and right neighboring RUs and Δt is the chosen time step. At each time step, for each RU, a random number R between 0 and 1 was generated, and transitional probabilities were calculated for the given RU considering its current state and the states of neighboring RUs. Potential transitions were calculated for each state based on Figure 4.1. For example, in the case where a given RU is in the *Ma* state, with a left neighbor in the *B0* state and right neighbor in the *C* state,

$$P1 = k_P^+ \Delta t \tag{4.24}$$

$$P2 = f^-(BC)\Delta t \tag{4.25}$$

The final state of the RU, $Z_{t+\Delta t}$, is determined by comparing R to P1 and P2. If $R < P1$, $Z_{t+\Delta t}$ = *Mb*. If $P1 < R < P2$, $Z_{t+\Delta t}$ = *C*. If $P2 < R$, $Z_{t+\Delta t}$ = *Ma*, in other words, the RU does not change states. $\Delta t = 5e^{-4}$ for all simulations in order to ensure that the sum of all possible transition probabilities will be less than 1 for our ranges of possible rates.

For steady state simulations, constant $[Ca^{2+}]$ was applied for all t. The initial condition for all 26 RUs is the *B0* state, and boundary conditions were set so that the 1st and 26th RU were clamped in the B0 state. The proportion of RUs in each state was recorded at each time step, and simulations were repeated 1024 times and state occupancy averaged due to the stochasticity of the system. Total force was considered to directly relate to the number of RUs in the *Mb* state at any time t. Therefore, to calculate steady state force F_{SS}, the number of RUs in the *Mb* state for all $2.5 < t < 3.0s$ were averaged, and normalized to the value at $pCa = 4.0$ (4.1.

To simulate slack-restretch experiments for the calculation of k_{tr}, a steady- state simulation is run for 2 s, at which point all RUs are reset to state B1 to simulate breaking of XBs. Then, the steady state simulation continues and k_{tr} is calculated as $k_{tr} = (1.264t_{1/2})^{-1}$ [225] in order to compare with experimental values which were calculated in the same manner [67].

Simulations were performed with varying ratios of dATP to ATP in order to test competitive binding of the nucleotide. The association rate of ATP and dATP to myosin were assumed to be identical due to earlier studies suggesting the same [66]. For each RU moving from the *C* state to the *M* state, an additional random number *P* was generated at each time point. This number was compared to the inputted percent dATP of the system. If P ¿ percent_{dATP}, the ATP rates were used to govern the transition. However, if $P \leq \text{percent}_{dATP}$, dATP was assumed to be near the binding pocket instead and dATP rates were used for the transition. A boolean was used to track the presence of ATP/ADP (0) or dATP/dADP (1) attached to myosin in both the Ma and Mb states depending on the nucleotide present during the transition from *C* to *M*.

4.3.5 Brownian dynamics

Methods for the Brownian dynamics studies drawn from herein are described in detail in [226]. PDB: 5KG8 was used as a template structure for the bound conformation of myosin and an actin monomer or dimer [217]. ADP- and dADP- bound myosin S1 structures were gathered from run 1 of molecular dynamics simulations from [79] at 50 ns. PQR files were created for all structures using the Amber18 forcefield with PDB2PQR [219, 227, 163]. Electrostatic fields were generated for both myosin and actin structures using APBS [203]. To determine association rates, Brownian dynamics (BD) simulations were performed using BrownDye software [162]. In the actin monomer case, 1 million BD trajectories were completed for both ADP-and dADP myosin, and for the actin dimer cases 500,000 trajectories were completed. For each trajectory, a binding event was considered to occur if 3 atom pairs (calculated as likely hydrogen bonding atoms within 3.5 Å of each other in the bound conformation) moved within the a certain reaction distance during the trajectory. Instead of prescribing a specific reaction distance for the simulation, the closest distance between the binding regions was recorded for each trajectory. This allowed for calculation of association rates for a wide range of reaction distances (6 Å to 100 Å) using the rates_of_distances function in BrownDye. For more detailed

information on BD methods and rate calculation, see [226].

4.4 Results

4.4.1 Wild type Steady state force-pCa curve optimization and model behavior

A wild type (WT) steady state force-pCa curve was optimized to experimental data from Regnier et al. [67], who measured steady-state force in skinned rat trabeculae with the α-myosin heavy chain (α-MHC) isoform and only ATP in the system. Optimization was further constrained by matching the experimental slack-restretch rate of tension redevelopment at pCa = 4.0, which was measured to be 13.8 s^{-1}. It was also assumed that $\gamma_B > \gamma_M > \mu_M$ because the energy required to move Tm 25 degrees from the B to C state is assumed to be higher than the smaller 10-degree *C* to *M* transition [42]. Optimized parameters are displayed on the first line of Table **??**, and optimized curves are displayed as black lines in 4.2. The experimental data indicated a WT k_{tr} of 13.8 s^{-1}, compared with a simulated k_{tr} of 13.64 s^{-1} in the optimized best fit.

Table 4.1. Optimized parameters for ATP and dATP SS curve fitting. The two dATP cases represent the f^+ value determined from BD with 1 actin or 2 actin molecules, and in each case k_P^+ and g^+ were optimized based on the calculated f^+.

	$k_{Ca}^+(\mu M^{-1}ms^{-1})$	$k_{Ca}^-(ms^{-1})$	$k_B^+(ms^{-1})$	$k_B^-(ms^{-1})$	$f^+(ms^{-1})$	$k_P^+(ms^{-1})$	
ATP	0.0935	1.0	24.7	0.09	0.1	0.754	
dATP (1 actin)					1.377	7.4	
dATP (2 actin)					0.448	2.6	
	$g^+(ms^{-1})$	γ_B	γ_M	μ_M	$k_{tr}(s^{-1})$		
ATP	1.0	98	10	7	13.64		
dATP (1 actin)	11.2				19.53		
dATP (2 actin)	3.45				17.0		

Sensitivity of the steady-state force curve to cooperative parameters γ_B, γ_M, and μ_M was tested using the optimized ATP curve as a baseline parameter set 4.2. γ_B affects the calcium sensitivity of the steady-state force greatly, as larger values of γ_B decrease the calcium sensitivity of the thin filament. A large change in cooperativity is observed when moving from

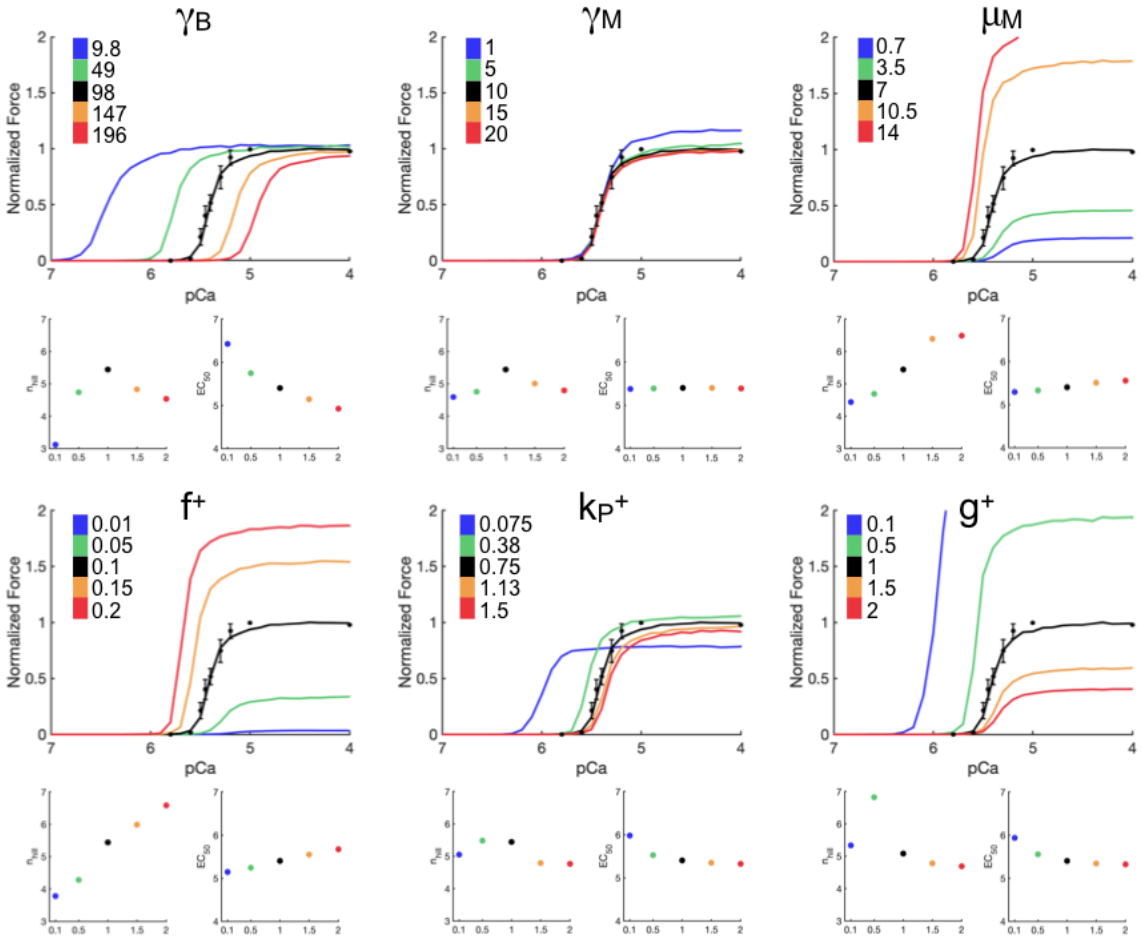

Figure 4.2. Sensitivity analysis of cooperative parameters γ_B, γ_M, and μ_M, and XB parameters f^+, k_P^+, and g^+. For all parameters, values used for steady state curves are 10% *(Blue), 50% (Green), 100% (Black), 150% (Orange), and 200% (Red) of optimized WT value. Experimental steady state values are indicated using black dots with error bars, and the optimized WT curve is an identical solid black line in each graph. Corresponding EC_{50} and n_{hill} beneath, with dot colors corresponding to the curve above.

a value of 9.8 to 49, but beyond this value the cooperativity does not change significantly. γ_M is the least sensitive cooperative parameter for the given starting parameter set. This parameter is still necessary for cooperativity in the model, however, because of the change in cooperativity evident in the change from $\gamma_M = 1$ (no cooperativity) to $\gamma_M = 5$. Increasing μ_M leads to increased calcium sensitivity and cooperativity, as higher values ease the movement into the Open force producing Tm position.

4.4.2 Brownian dynamics studies show increased XB attachment rate for dATP-myosin

After optimizing the ATP curve, attempts were made to optimize the dATP curve by altering just 3 parameters: f^+ (XB attachment), k_P^+ (powerstroke rate), and g^+ (XB detachment). These three parameters were chosen because they are transition points that directly involve ATP and its interaction with myosin S1 [58]. As hypothesized previously [66, 74], our initial assumption was that all three forward XB parameters should be increased to lead to higher force production and faster XB cycling. For the purposes of our model, we also assumed that these three parameter changes should be sufficient to explain all changes in crossbridge behavior as a result of dATP treatment. Previously performed Brownian dynamics simulations of myosin-actin association using a single actin monomer showed a significant increase in XB association rate for all measures reaction distances [226]. Matching the association rate with the optimized ATP rate (10^8) leads to a reaction distance of 13.72 Å. At this reaction distance, the Brownian dynamics simulation predicted that dATP would increase the association rate f^+ (XB attachment) 13-fold to 13.77 (Figure 4.3B).

Additional Brownian dynamics simulations were performed on an identical system, but with two actin monomers rather than one. Structural studies have shown significant interactions between myosin S1 and multiple actin molecules along the thin filament [217, 228]. In this second BD study, increases were again observed in association rate at all reaction distances for dATP- versus ATP- myosin. However, at all reaction distances a smaller increase was observed

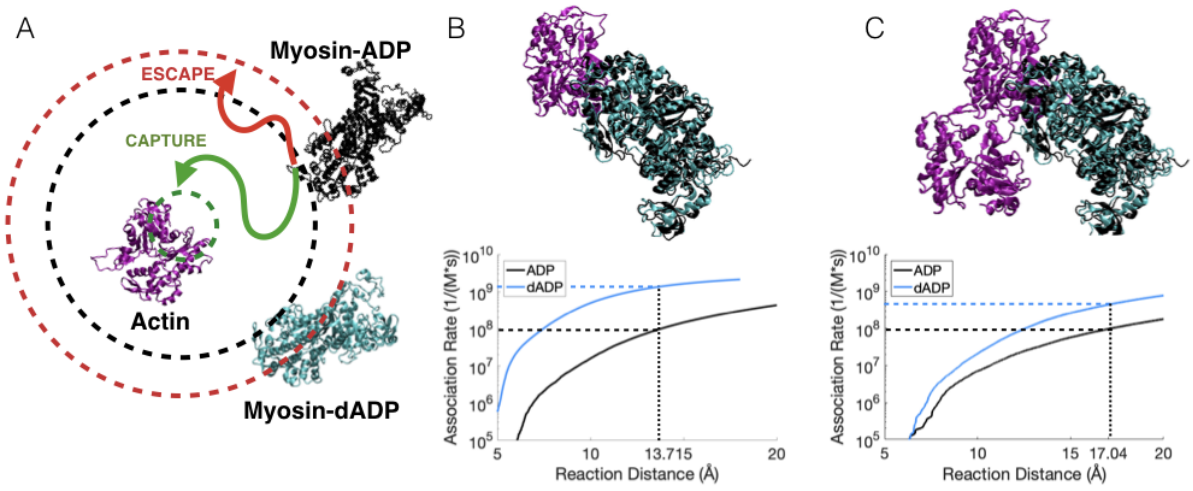

Figure 4.3. BrownDye simulations of acto-myosin association were performed to determine the electrostatically-based differences in association rate between ADP- and dADP-bound myosin. A. For each BrownDye trajectory, a myosin monomer was generated randomly on a spherical surface approximately 120 A from the actin monomer. A timecourse was run on the molecules combining random diffusion and electrostatic forces to determine if the molecules moved close enough to be within the prescribed reaction distance, or if the molecules moved farther away and escaped. B. The bound conformation of ADP-myosin (black) or dADP-myosin (cyan) with a single actin monomer, visualized using VMD [200]. Below, a plot of second-order association rates for actin-myosin binding as a function of prescribed reaction distance. For WT simulations, the association rate was optimized to 1e8 1/(M*s) which corresponds to a reaction distance of 13.72 A. C. The bound conformation of ADP-myosin (black) or dADP-myosin (cyan) with an actin dimer, again overlaid on PDB: 5KG8. In this case, the WT association rate corresponds to a reaction distance of 17 A.

compared to the single actin monomer study, demonstrating less of an electrostatic effect of dATP binding when multiple actin molecules are present in the system. In this case, the ATP association rate of $10^8(M.s)^{-1}$ corresponds to a reaction distance of 17 Å. At 17 Å, the dATP association rate was calculated as $4.48 \times 10^8(M.s)^{-1}$, a 4.5-fold increase (Figure 4.3C).

The results show a clear increase in XB attachment when dATP is bound to myosin rather than ATP, for both the case of myosin in complex with one (13.8-fold increase) and two actin monomers (4.5-fold increase). This is consistent with previous hypotheses that dATP increases force by increasing XB attachment rate. From this result, we also conclude that the interaction between myosin and two adjacent actin molecules simultaneously greatly affects the electrostatics of the XB binding event compared to binding of myosin to a single actin monomer.

4.4.3 dATP increases maximum steady state force and Calcium sensitivity

Considering a single calculated f^+ determined directly from BD simulations, sensitivity analysis was performed on the other two XB parameters, k_P^+ and g^+. Increasing k_P^+ leads to a slightly increased hill coefficient, significant decreases in calcium sensitivity and small increases in maximal steady state force (Figure 4.4A). Increasing g^+ caused increases in the hill coefficient, slight decreases in calcium sensitivity and significant decreases in maximal force (Figure 4.4B). Accurate recreation of the dATP curve requires an increase in maximum force and calcium sensitivity, which mathematically requires a combination of increases in k_P^+ and g^+ as hypothesized.

After optimizing for k_P^+ and g^+, the dATP experimental steady state curve could indeed be reliably recreated with a unique set of parameters for each potential f^+ value 4.5. For the case of BD with a single actin monomer, dATP XB attachment rate $f^+ = 1.377\mu M^{-1}ms^{-1}$. A combination of $k_P^+ = 7.4ms^{-1}$, a 9.8-fold increase, and $g^+ = 11.2ms^{-1}$, an 11.2-fold increase, minimized the residual compared to experimental dATP data (4.5A). For the 2 actin monomer

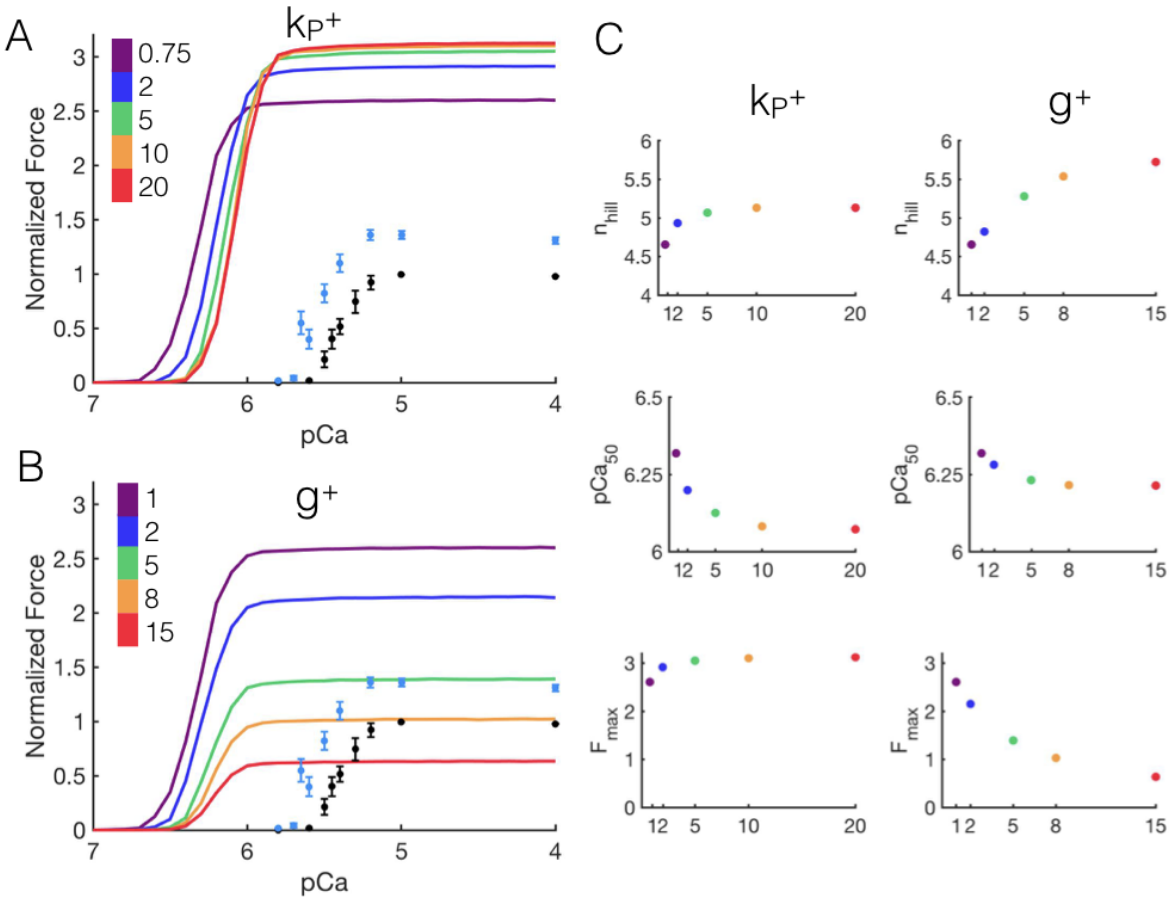

Figure 4.4. Sensitivity analysis of powerstroke rate and XB detachment rate when setting attachment rate according to actin monomer BD simulations (f^+ = 7.4, all other rates from WT optimization). A. beginning with WT k_P^+ value of 0.75 (purple line), as k_P^+ increases the maximal steady-state force increases slightly and Calcium sensitivity decreases, with the highest $k_P^+ = 20$ being the red line. B. beginning with the WT g^+ value of 1 (purple line), as g^+ increases the maximal steady-state force decreases and Calcium sensitivity is not significantly altered, with the highest $g^+ = 15$ being the red line.C. Side-by-side analysis of hill coefficient (N_{hill}), calcium sensitivity (pCa_{50}) and max SS force (F_{max}) as either k_P^+ or g^+ is increased. A decrease in both F_{max} and pCa_{50} are necessary to match cyan experimental data, indicating that some combination of increases to both these rates is required.

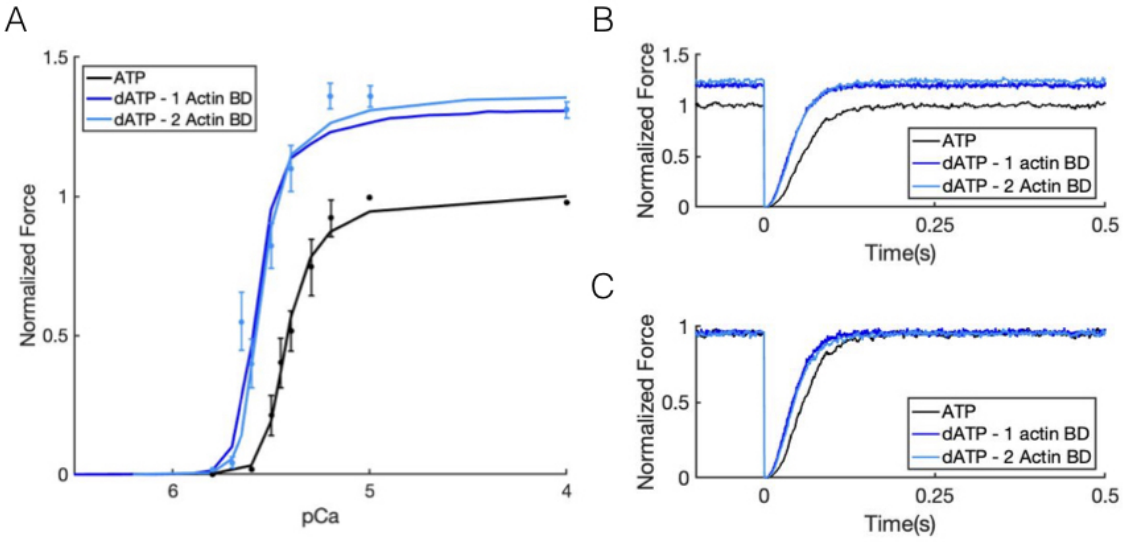

Figure 4.5. Using BD-calculated f^+, there is one unique combination of increases to k_P^+ and g^+ which minimizes the least squares error compared to experimental dATP data. A. Optimized WT and dATP curves match experimental data from Regnier et al. Experimental data are dots with error bars, and solid lines are simulations (black = ATP, blue = dATP using parameters from 1 actin BD simulation, cyan = dATP using BD results from 2 actin simulation). B. Slack restretch experiments used to calculate k_{tr} for different parameter sets at pCa = 4.0 (black = ATP, blue = dATP from 1 actin BD, cyan = dATP from 2 actin BD) Absolute forces were normalized to the maximum WT force to demonstrate differences in steady state force production. C. absolute forces from (B) were normalized to maximum force of each simulation, to demonstrate differences in tension redevelopment kinetics.

case, f^+ was calculated as $0.448\mu M^{-1}ms^{-1}$. The combination of $k_P^+ = 2.6ms^{-1}$, a 3.3-fold increase, and $g^+ = 3.45ms^{-1}$, a 3.5-fold increase, led to the best fit in this case. The best fits for both cases to the experimental steady-state force-pCa curves can be seen in 4.5B. The maximum force is slightly higher in the two-actin case than the one-actin case, but both curves have similar least squares residuals (one-actin: 0.22, two-actin: 0.15).

4.4.4 k_{tr} narrows possibilities for dATP XB parameters

To determine which BD simulated outcome is the most physiologically realistic, k_{tr} studies were compared to experimental results. At pCa = 4.0, experiments determined $k_{tr} = 17.6s^{-1}$, a 27.5% increase over WT. For the one-actin BD simulation, $k_{tr} = 19.53s^{-1}$, a

43% increase over WT simulations. In the two-actin BD simulation, $k_{tr} = 17.0s^{-1}$, a 24.7% increase. The simulated k_{tr} experiments are displayed in 4.5B, visualized to demonstrate change in maximum force (top) and tension redevelopment (bottom) in the separate images. The experimental fold increase of 27.5% is in between the two BD-derived parameter sets, but is significantly closer to the two-actin case, only differing by 0.6 s^{-1} in absolute k_{tr}. The two-actin BD simulation resulted in a parameter set that could closely reproduce both the steady-state curve and k_{tr} results.

4.4.5 Nonlinear force increases are observed at low dATP/ATP ratios

Steady-state simulations were performed on the system at various ratios of dATP to ATP with competitive nucleotide binding. In Figure 4.7 the steady state force is displayed for various dATP percents at pCa = 5.5 and pCa = 4.0 to allow for comparisons to experimental studies in skinned pig trabeculae [69]. For the one-actin BD case, exaggerated nonlinear increases are seen at very low dATP levels at both pCa 4.0 and 5.5 (4.6, dark blue lines). Even when thin filament cooperativity is not included in the model (all cooperative parameters = 1, no coupling between RUs) nonlinear increases are still seen due to the overwhelming effects of the large rate increases on overall XB cycling speed and force production. Focusing on the 5% dATP level considered to be an upper bound of dATP gene therapy, at pCa 4.0 the there is a 12.7% increase in steady state force compared to WT. 100% dATP leads to a 30.2% increase in force, meaning that 42.1% of the overall force increase due to dATP is present when only 5% of the total energetic pool is dATP. Without RU-RU coupling, the force increase at 5% dATP is similar but slightly less pronounced, with 40.0% of the total dATP force increase.

For the two-actin BD simulation with less exaggerated increases to all XB parameters, nonlinear increases are visible at physiological pCa values (pCa = 5.5), but the relationship appears slightly more linear at pCa 4.0 (4.6, light blue lines). At both pCa values, the nonlinearity of the relationship is decreased compared with the one-actin model. At the therapeutic

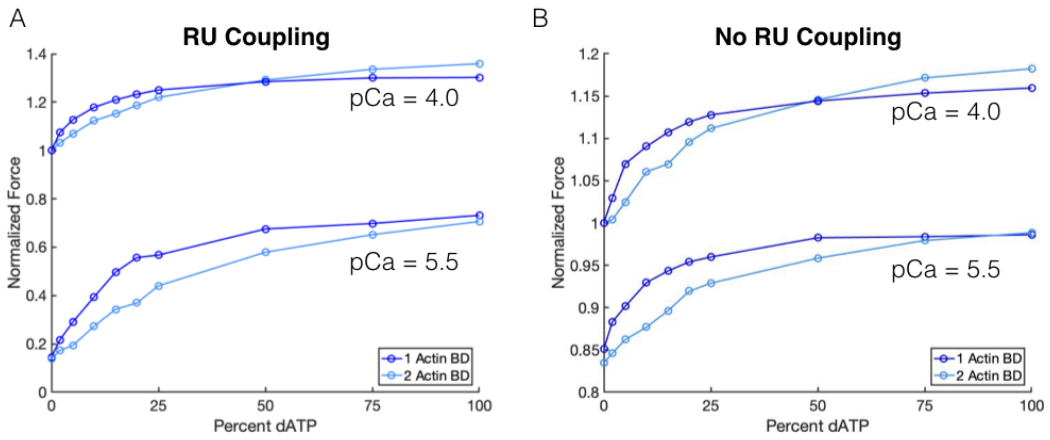

Figure 4.6. Steady state force at pCa 5.5 and pCa 4.0 as a function of dATP/ATP ratio (WT = 0% dATP). Dark blue curves: parameters from 1 actin BD study, cyan curves: parameters from 2 actin BD study. A. Full model simulations including optimized cooperative parameters B. Force results when RU-RU coupling is removed (all cooperative coefficients = 1)

5% dATP value, there was a 6.8% increase in steady-state force at pCa 4.0 compared with WT. This is 19.1% of the force increase achieved with 100% dATP. Again, a smaller effect was seen with no RU-RU coupling. at 5% dATP, only 13.3% of the total dATP force increase is observed. We still see a nonlinear response, but the effect is less pronounced without coupling of RUs.

4.4.6 dATP enhances twitch kinetics

Twitch simulations were performed by inputting calcium transients measured in adult rat cardiomyocytes by Korte *et al.* [73] into the model and observing force outputs (4.7A). The input transients are visible in insets of Figure 4.7A and C. First, the WT calcium transient was tested on varying ratios of dATP to ATP. Increasing dATP percent led to increased maximum twitch force, with the 100% dATP case resulting in a 90.2% increase in maximum twitch force compared to WT. At 10% dATP, the maximum force increase was 18.2 %, again outputting higher force increases at low dATP levels than one would expect if the relationship between F_{max} and dATP % were linear. Interestingly, the relaxation time to 50% force (RT_{50}) was increased from 45 ms to 55 ms in the 100% dATP case compared to WT (**??**B). As for the time to 90% relaxation (RT_{90}), in the 100% dATP case $RT_{90} = 105ms$, an increase compared to the

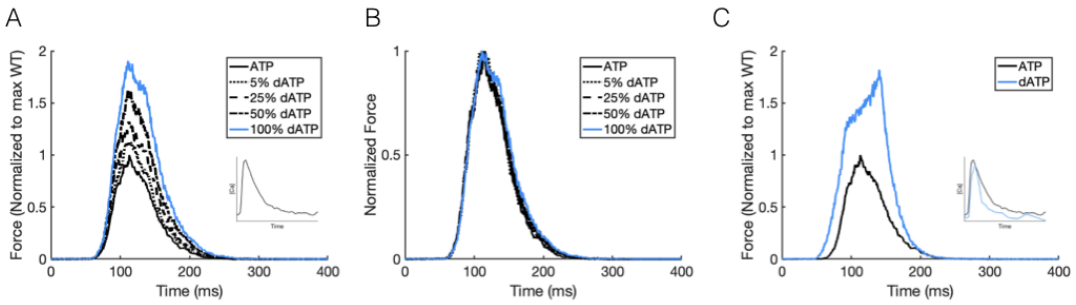

Figure 4.7. Twitch simulations with experimental calcium transient inputs. A. Force (normalized to maximum WT force) as a function of time. The input calcium transient is displayed in the inset, and is digitized from [73]. Solid black line: WT. dotted line: 25% dATP. dashed line: 50% dATP. dot-dash line: 75% dATP. solid cyan: 100% dATP. B. Identical twitch results, normalized to the maximum force for each data set. Thw WT curve relaxes faster than all dATP cases. C. Black line: WT twitch with WT calcium transient from Korte et al. Cyan line: 100% dATP twitch with dATP treatment calcium transient from Korte et al, as indicated by the blue line in the inset.

WT case where RT_{90} =90 ms In the original experiments, these values both decreased with dATP treatment, although a direct value comparison isn't possible because the experiments measured shortening in intact cells, whereas our model simulates isometric skinned trabeculae. During the original experiments, however, an altered calcium transient was observed in the case of dATP treatment. When the WT calcium transient was input to generate WT force and the dATP calcium transient was used for the 100% dATP twitch, RT_{50} remained unchanged between the WT and dATP case at 45 ms (4.7C). RT_{90}, on the other hand, decreased in the dATP case to 80 ms from the WT value of 90 ms. This result suggests that experimentally observed altered twitch kinetics during dATP therapy owe in part to effects of the treatment on intracellular calcium handling. Further study should be pursued on the effect of dATP on the ATP-dependent Ca^{2+} pumps, especially the sarcoendoplasmic reticulum Ca^{2+}-ATP-ase, SERCA.

4.5 Discussion

In this study, we used a multi-scale computational modeling approach to gain insight into the mechanisms by which 2-deoxy-ATP, even in low ratios to ATP, can significantly increase myocyte twitch force and thin filament calcium sensitivity and alter twitch force kinetics. Using atomistic Brownian dynamics simulations, we predicted significant increases in the attachment rate of dADP-myosin to actin than ADP-myosin. These results then constrained the parameter estimation of a Markov-state model of cooperative myofilament interactions so that unique estimates of the crossbridge dissociation and power-stroke kinetics could be obtained from previously measured steady-state force-calcium and transient force redevelopment measurements in rat trabeculae. These optimizations suggested that the attachment rate increase predicted by BD simulations of myosin association to an actin (4.5 fold), combined with modest increases in both the powerstroke and XB detachment rate (3.3 and 3.5 fold, respectively), reliably reproduce tension development and steady state experimental results. The increase in duty cycle (due to a more significant increase in attachment than detachment rate) contributes to the observed force increases in steady state results, as originally predicted in experimental studies which stated that increases to f^+ must be higher than increases to g^+ [67].

A compelling reason that dATP treatment is so promising is that large force effects have been observed even at small dATP/ATP ratios. Using the optimized dATP XB cycling rates, our model predicts that a large positive nonlinear force increase will occur in steady state force, with a 6.8% increase in steady state force occurring at just 5% dATP in an excess Ca^{2+} environment (pCa = 4.0). In an experimental study on pig trabeculae, nonlinear increases in steady-state force were observed between 0% dATP and 20% dATP for pCa 5.5 but force increases were proportional to dATP concentration at pCa 4.0 [69]. Our study demonstrated a nonlinear pattern at all pCa values, even without RU-RU coupling present. Intuitively, it would seem that the observed pattern occurs due to thin filament cooperativity, as a small number of bound dATP XBs could precipitate thin filament activation of neighboring RUs. Indeed,

for the more realistic two-actin BD parameters, without RU coupling, the nonlinear effects are less pronounced. However, there are other factors at play which must contribute to the positive nonlinearity apparent even without coupling. One potential contributor may be the large increase in XB cycling speed and duty cycle of dATP-bound XBs. From the two-actin BD simulation, f^+ increased by 4.5-fold and g^+ was increased by 3.5-fold. XB duty cycle, $f^+/(f^+ + g^+)$, was 0.09 for WT and 0.11 for dATP because the increase in f^+ was greater than that in g^+. At any given time during dATP-aided XB cycling, XBs are more likely to be attached, which may have an outsize effect on overall force production. Although our model replicates the overall positive nonlinear phenomenon, there were quantitative differences between our model results and experimental results in the pig studies [69]. This discrepancy is likely due to species. Pig muscle experiments test cardiac muscle with β-MHC as the dominant isoform, whereas our model is optimized for rats expressing α-MHC. In fact, an experimental study testing differences between the effects of dATP on α- and β-MHC demonstrated varied impact on steady state and developing force between the isoforms [67].

The model described in this work also makes predictions about alterations to twitch kinetics due to dATP treatment. Positive nonlinear increases in steady state forces are observed in twitch simulations, indicating that low therapeutic levels of dATP can provide significant increases in cardiac contractility in physiological scenarios. Interestingly, when providing the WT calcium transient in all simulations, the model increases maximum force as the percent dATP increases, but relaxation rates decrease in the case of both RT_{50} and RT_{90}. This result seems to be in opposition to experimental *in-vivo* results in various species displaying improved relaxation kinetics. However, when using dATP- affected calcium transients gathered from experimental data [73], accelerated relaxation rates were indeed observed in the model. Therefore, an integrated model of excitation-contraction coupling should be employed to further explore mechanisms by which dATP alters the complex feedback web between the sarcomere, in a dual role as force producer and calcium buffer, and calcium handling ATPases such as

PMCA, SERCA, and NCX.

It should be noted that the BD system used in this study to measure the role of differing electrostatic interactions on the association rate between actin and myosin was simplified. We considered a free floating myosin S1 and 2 actin molecules rather than myosin as part of a much larger thick filament system and a thin filament containing dozens of actin monomers as well as other thin filament proteins such as troponin, tropomyosin, and myosin binding protein C. However, we chose to model the actin-myosin interaction in a simplified system in order to study the specific effects of dATP on the kinetics before integrating into a larger-scale model which incorporates other thin filament proteins such as troponin. The ability of this simplified system to recreate both steady state and slack-restretch experimental results is strong evidence of the significant role that electrostatic acto-myosin interactions have in the differences between observed contractility for ATP- and dATP- myosin. Further molecular level study should be pursued to validate the accuracy of the specific rate constants, e.g. the 3.3 fold increase in powerstroke speed and 3.5 fold increase in detachment rate resulting from dATP binding predicted by our model.

Our results strengthen the hypothesis that the mechanism of dATP therapy, with regard to increases in contractility, is localized to myosin. Increasing cardiac dATP does not affect cooperative mechanisms directly, but rather conformationally alters myosin so that it has an increased affinity to the actin thin filament when detached, coupled with an increased tendency to detach from actin when in the post-powerstroke state. We also considered the possibility that an altered myosin S1 conformation may lead to a faster powerstroke. Our results show that with these constraints on a Markov Chain model of the sarcomere, we can reliably reproduce experimental results regarding the effects of dATP therapy on steady state force production and tension kinetics. The experimentally observed improvement in twitch relaxation during dATP treatment was hypothesized to occur due to increased XB detachment rate. Indeed, our optimization after taking into account the increased attachment rate predicted by BrownDye

concluded that the only way to match kinetic and steady state results determined through experiments is to increase the detachment rate of XBs by 3.5 or 11.2 times depending on the BD study chosen for optimization. Using our novel framework of integration from atomistic scale to a Monte Carlo Markov Chain model of sarcomere mechanics, we have achieved broad insights into the electrostatic effects of dATP on myosin-actin interactions and quantified the impact of dATP on sarcomere force development.

4.6 Acknowledgements

Chapter 4, in full, has been submitted for publication of the material: McCabe KJ, Aboelkassem Y, Dewan S, Regnier M, and McCulloch AD. "Predicting the effects of dATP on cardiac contraction using a Markov Chain model of the sarcomere". J Physiol. *(Submitted)*. The dissertation author was the primary investigator and author of this material.

Chapter 5

A Multiscale Computational Modeling Study to Determine the effects of 2-deoxy-ATP on SERCA Pump Function

5.1 Abstract

This study seeks to determine the effect of 2-deoxy-ATP on the SR-ATPase (SERCA), an ATP- driven pump which expels Ca^{2+} from the cytosol during cardiac relaxation. This multiscale study investigates the effects of dATP on calcium handling within the cardiomyocyte at the molecular and cellular level. We are the first to perform Gaussian accelerated Molecular Dynamics (GaMD) simulations on a new crystal structure of cardiac SERCA 2A (PDB: 5MPM). Three 160 ns simulation cases were investigated - apo, ATP-bound, and dATP-bound (2 replicates). dATP was found to cause the separation of cytosolic domains, which could indicate increased pump speed during dATP treatment. Transmembrane domains surrounding calcium binding Sites I and II were found to stabilize when either nucleotide was added to the system. BrownDye simulations were performed on representative structures from each simulation to determine nucleotide and calcium association rates. dATP was found to have an 80% higher association rate to apo SERCA than ATP. For dATP-bound SERCA, BrownDye simulations showed higher Ca^{2+} affinity for Site II than Site I, which is the opposite effect seen in simulations with ATP-bound SERCA. This ”site swap” phenomenon is likely an effect of altered electrostatic surfaces in the critical Ca^{2+} pathway into the transmembrane region as well as altered position of Ca^{2+} gating residue E309. BrownDye-gathered rate changes for nucleotide and Ca^{2+} binding were able to partially explain the effects of dATP treatment observed experimentally when integrated into a cell-scale ODE model of calcium handling. We provide the first biophysical evidence of mechanistic differences in SERCA pump function caused by interactions with dATP.

5.2 Introduction

Sarcoendoplasmic reticulum Ca2+-ATPase (SERCA) 2A is a P-Type ATPase [229] which is critical for sequestration of calcium into the sarcomplasmic reticulum (SR) during cardiac relaxation and is the dominant SERCA isoform in cardiac muscle [230, 231]. SERCA is a transmembrane protein embedded in the SR lipid membrane which consists of 3 cytosolic domains (Nucleotide binding domain - "N", Phosphorylation domain - "P", Actuator domain - "A") as well as 10 transmembrane (TM) helices, M1 through M10 (Figure 5.1A) [232]. The nucleotide binding region is located within the cytosolic domains closest to the N domain. Calcium binding occurs in the transmembrane region between helices M4, M5, M6, and M8, at binding locations known as Site I and Site II [233]. Generally, SERCA moves through two major states as it pumps calcium into the SR in an ATP-driven manner - E1 and E2. The first state, E1, exists when the calcium binding sites face the cytosolic side of the membrane [234]. Binding of ATP and 2 calcium ions, followed by ATP hydrolysis and various phosphorylation and dephosphorylation events, reconform the protein so that the calcium binding sites can escape into the SR lumen [234]. The SR-facing conformation is known as E2. Release of ADP, Pi, and Ca^{2+} ions into the SR lumen allow the protein to move back into the E1 state [235]. A simplified ODE model of SERCA function developed by Tran et al describes several rate-limiting steps within the cycle: (1) MgATP binding, (2) binding of the first calcium ion to site I (site II binding is then considered to occur instantaneously), (3) ADP release, coupled with the E1-E2 transition, (4) Pi release, coupled with E2-E1 transition [236]. In this study, we choose to focus on (1) and (2) in order to examine the effects of a novel treatment for heart failure on SERCA 2A.

2-deoxy-ATP (dATP) is a naturally occuring nucleotide which is nearly identical in structure to ATP, excepting a missing oxygen on the 2' carbon of the ribose ring (Figure 5.1B). Despite the nearly identical structure of the two molecules, force production has been found to increase dramatically in cardiac cells when ATP is replaced by dATP [66, 67]. This finding

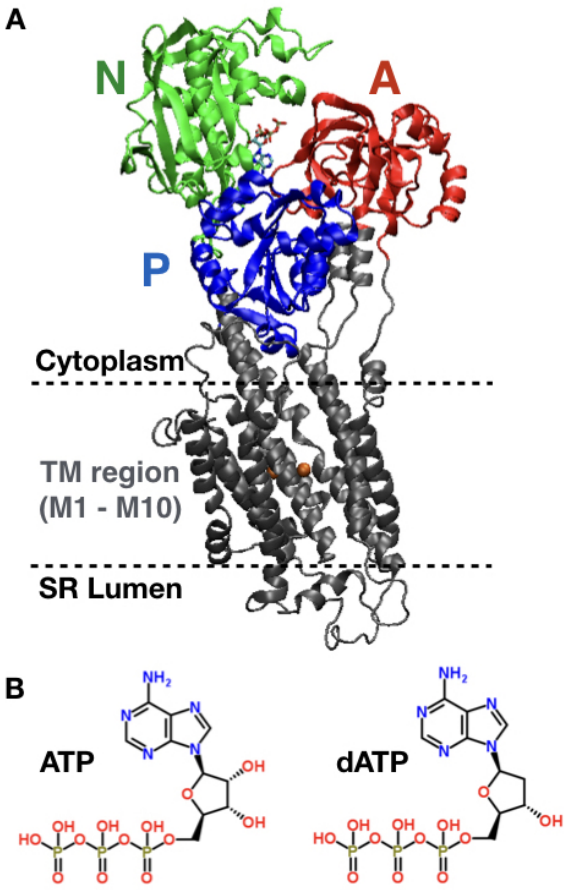

Figure 5.1. (A) SERCA 2A structure with docked ATP in the nucleotide binding pocket in the cytosolic region. Structure minimized from PDB: 5MPM. SERCA displayed as ribbons, with domains highlighted as follows: Nucleotide binding domain (N, Green), Actuator Domain (A, Red), Phosphorylation Domain (P, Blue), Transmembrane region (Helices M1-M10, grey). ATP is displayed in the nucleotide binding pocket as balls and sticks, and calcium ions are visualized as orange spheres in the transmembrane region. (B) structure of ATP versus 2-deoxy-ATP (dATP).

has led to various studies exploring the potential for dATP as a therapeutic myosin activator to treat heart failure [69, 74, 75, 76]. In one such study, upregulation of dATP to 5% of the overall ATP pool led to increased cell shortening, but also had a marked effect on the calcium transient [73]. This study reported decreased time to 50% and 90% calcium transient decay, indicating that calcium relaxation is enhanced during dATP treatment [73]. Although calcium relaxation kinetics are not meant to be the main function of the drug, this phenomenon may be an additional therapeutic benefit as many heart failure conditions are characterized by decreased function and expression of SERCA 2A [237, 238].

It is necessary to explore the effects of dATP on SERCA 2A at multiple scales in order to uncover potential mechanisms of upregulation which will affect the overall cardiac calcium transient. We conducted 160 ns Gaussian accelerated Molecular Dynamics (GaMD) simulations of a new crystal structure of SERCA 2A (PDB: 5MPM) embedded in a lipid bilayer [239, 240]. Simulations were conducted on 3 separate systems- apo, ATP-bound, and dATP-bound. Analysis of the MD trajectories and energy landscapes allow us to locate key areas in the cytosolic and transmembrane domains of SERCA which may be affected by dATP binding. We then perform rigid body molecular Brownian Dynamics (BD) studies to measure association rate between SERCA 2A and ATP, dATP, and calcium ions in both Site I and II [**?**]. BrownDye analysis uncovers a potential pathway by which calcium may bind Site II before Site I when dATP is bound to the N domain, which is in conflict with known mechanisms of SERCA function. We also find that dATP shows increased affinity for SERCA2A compared to ATP. Finally, we integrate the results into an ODE model of calcium handling which allows us to determine the effects of the observed molecular changes on the calcium transient as a whole [241].

5.3 Methods

5.3.1 Gaussian Accelerated Molecular Dynamics Preparation and Simulations

We began with a crystal structure of cardiac SERCA 2A E2 purified from pig heart and retrieved from the RCSB Protein Data Bank (PDB: 5MPM)[240]. We removed the ligands CZA and MgF_3, but kept 2 Mg^{2+} ions and one K^+ ion from the original structure for stability. Using ProPKA 3.1 and previous studies on the homologous SERCA 1A structure, GLU 309, 770, and 907 were protonated and a disulfide bond was added between CYS 875 and CYS 887 using VMD 1.9.4 in order to simulate the protein at pH = 7.0 [242, 243, 244, **?**]. Maestro was used to perform an initial RMSD 0.3 A backbone minimization to prevent atom overlap [245]. To generate Mg-ATP and Mg-dATP bound structures, the Glide tool was used to dock the nucleotides into the binding pocket on the cytosolic side of SERCA [246, 247]. For the dATP case, 2 possible locations of the nucleotide were identified as likely binding positions, so the outcome closer to the ATP docking location was chosen as the dATP coordinate set. The protein was embedded in a 12.5 x 12.5 nm POPC lipid bilayer using the VMD 1.9.4 Membrane Builder tool, surrounded by a water box measuring 125 x 125 x 160 Å, and ionized with 0.15 M KCl according to a protocol by Autzen and Musgaard [248, **?**]. A POPC bilayer was chosen due to the observation that 65% of the cardiac SR membrane is made up of POPC [249]. The amber14 force field was used to parameterize the protein [220], lipid [250], water and ions. To parameterize ATP and dATP, Antechamber and the generalized amber force field (gaff) were used [251, 252]. Prep files for ATP and Mg^{2+} were gathered from the Amber Parameter Database hosted by the Bryce group [253, 254].

Gaussian Accelerated Molecular Dynamics (GaMD) simulations were performed using amber14 [255, 256]. First, minimization protocols were run successively on the solvent, lipid, sidechains, and whole system. The system was then heated to 100 K quickly (50 ps) and then slowly the temperature was raised to a physiological temperature of 310 K (250 ps).

Simulations were run with a 2 fs timestep and 10 Ånon-bonding cutoff. An unrestrained equilibration was then run on the heated system for 1000 ps. 50 ns of conventional MD was run on the system, followed by 160 ns of dual-boosted GaMD simulations (both dihedral and total potential energy boosts). In GaMD, a Gaussian distribution is used to provide a boost potential for the system in order to enhance energy sampling at shorter simulation time scales [239]. A total of 5 160 ns GaMD simulations were run: 1 for apo SERCA, 2 for ATP-bound SERCA, and 2 for dATP-bound SERCA.

VMD was used for trajectory and structure visualization [**?**]. Atomic distances and dihedral angle calculations were performed for all trajectories using cpptraj [257]. Energetic reweighting of trajectory data was performed after all simulations using a Gaussian approximation of cumulant expansion to the second order. This step is necessary because a boost potential was applied at each time step in order to flatten the energy landscape during the simulation and increase conformational sampling [256]. Briefly, the potential for mean force (PMF) as a function of reaction coordinate A_j is calculated as

$$PMF(A_j) = -\frac{1}{\beta} \ln p(A_j) \tag{5.1}$$

Where $\beta = k_B T$ and $p(A_j)$ is the canonical ensemble distribution. Because boost potentials followed a Gaussian distribution, $p(A_j)$ must be calculated from the ensemble distribution of the boosted data set as:

$$p(A_j) = p^*(A_j) \frac{\langle e^{\beta \Delta V(r)} \rangle_j}{\sum_{j=1}^{M} \langle e^{\beta \Delta V(r)} \rangle_j} \ln p(A_j), J = 1, ..., M \tag{5.2}$$

where $\Delta V(r)$ is the boost potential of each frame, M is the number of bins, and $\langle e^{\beta \Delta V(r)} \rangle_j$ is the ensemble-averaged Boltzmann factor for frames in bin j.$\langle e^{\beta \Delta V(r)} \rangle$ is approxi-

mated using second order cumulant expansion and is calculated as:

$$\langle e^{\beta \Delta V(r)} \rangle = \exp \left\{ \sum_{k=1}^{\infty} \frac{\beta^k}{k!} \sigma_{\Delta V}^2 \right\} \tag{5.3}$$

5.3.2 Brownian Dynamics Simulations

Representative structures for SERCA apo, ATP-bound and dATP-bound conditions were extracted from trajectories based on the lowest energy frame. For apo, this was 153.8 ns of simulation time, for ATP 137.6 ns, and dATP 136.0 ns. Structures were stripped of solvent and lipids in order to simulate on the protein alone. APBS 1.3 was used to calculate electrostatic grids for SERCA, as well as ATP, dATP, and Ca^2+ [164]. Amber restart files were converted to PQR files using ambpdb [255].

First, Brownian Dynamics simulations were performed to determine the association rate of ATP and dATP to the nucleotide binding region of apo SERCA using BrownDye [162]. Reaction pairs were determined by manual inspection of the bound system to determine 6 possible pairs for dATP or ATP binding SERCA: ARG 489 Cz - (d)ATP PG, LYS 492 Nz - (d)ATP PB, PHE 487 CG - (d)ATP C5, LYS 205 Nz - (d)ATP PB, LYS 205 Nz - (d)ATP PA, and ARG 559 Cz - (d)ATP C3*. A minimum of 3 pairs were required to come within the reaction distance to consider a trajectory to bind. No specific reaction distance was set, rather the closest distance for each trajectory was recorded in order to calculate rates for a wide range of possible reaction distances. Simulations were run with a dimensionless dielectric for the solvent of 78 and a Debye length of 7.86. The dielectric constant for both solutes was set to 4.0. 1 million trajectories each were run for ATP- apo SERCA and dATP- apo SERCA. The output of the simulations was a list of closest distance between the molecules for each trajectory, which was converted to a table of association rates versus reaction distances with the function rates_of_distances in BrownDye.

Similar simulations were performed to determine association rate of Ca^2+ to Site I and

Site II in the SERCA transmembrane region. For Site I, reaction pairs were determined as: ASP 799 CG - Ca^{2+}, GLU 770 CD - Ca^{2+}, GLU 907 CD - Ca^{2+}. For Site II, the three reaction pairs were set as: ASN 795 CG - Ca^{2+}, GLU 770 CD - Ca^{2+}, GLU 309 CD - Ca^{2+}. The same simulation parameters as above were employed, and 6 different simulations were run: apo Site I, apo Site II, ATP Site I, ATP Site II, dATP Site I, and dATP Site II. In each case, 1 million trajectories were run.

5.3.3 Calcium Transient Modeling

To model the Ca^{2+} transient, the Himeno model was employed [241]. This model was chosen because it explicitly includes a 3-state simplified SERCA model developed by Tran et. al. which includes parameters for ATP binding, Ca^{2+} binding, and E1-E2 transitions [236]. State P_1 is E1 SERCA, which undergoes a reversible reaction dictated by rates k_1^+ and k_1^- to state P_{2-5}, which is E1 SERCA with ATP and 2 Ca^{2+} ions bound. Ca^{2+} binding is considered to be fully cooperative, i.e. binding of the second Ca^{2+} ion is instantaneous after the first Ca^{2+} binding event. Reaction rates k_2^+ and k_2^- encompass MgADP dissociation as well as the E1-E2 transition, leading the model to state P_{6-10}. Finally reversible reaction rates k_3^+ and k_3^- return the pump to state P_1 [236].

dATP experimental data were digitized from Korte et al. figure 1B (GFP and R1R2, respectively) [73]. Fura ratio units were converted to Ca^{2+} concentration by setting the maximum fluorescence value to 0.45 uM, and the minimum value to 0.05 uM, since these are approximately the maximum and minimum Ca^{2+} values typically seen in the Himeno model [241]. The Himeno model was optimized to match the ATP Ca2+ transient by varying Amp_{SERCA}, Amp_{NCX}, Amp_{NaK}, and f_n, the same parameters which were tuned by Himeno et al. in parameterizing their original model [241]. Optimization was conducted using Particle Swarm Optimization (PSO) in MATLAB. The timescale of the applied current in the Himeno model was adjusted to reflect the change in species from human to rat and provide a closer fit

for the WT transient.

5.4 Results

5.4.1 dATP demonstrates stronger interactions than ATP with the nucleotide binding pocket of SERCA 2A

GaMD simulations were performed on dATP- and ATP-bound SERCA. Likely, the most obvious changes to SERCA molecular structure would begin within the cytosolic nucleotide binding pocket and then cascade through the molecule into the transmembrane region. To investigate the differential interactions of ATP and dATP with the binding pocket, a series of analyses were completed. Upon visual inspection, ATP appears to flip back and forth within the pocket in 2 main positions. The first position (Figure 5.2A, top left) closely resembles the position of ATP analogs in crystal structures with ring stacking between ATP and PHE 487 [258]. However, throughout the simulation ATP often flips downward into a conformation where the phosphate groups face upwards and the adenine ring closely associates with ARG 559 (Figure 5.2A, bottom left). In the case of dATP, the nucleotide remained more stable in the binding pocket nestled into the N domain (Figure 5.2A, top right). An analysis counting the number of nonnative contacts, defined as a 3 Ådistance, between each nucleotide atom and atoms within the protein identified significantly higher contact levels for dATP within the binding pocket than ATP (Figure 5.2A, bottom right). The average number of contacts over all simulation time was 35.6 for ATP, and 49.0 for dATP.

Three residues of interest were investigated to measure nucleotide interaction: PHE 487, LYS 514, and ARG 559. These residues were chosen due to their recognized roles as crucial interaction residues with ATP through mutagenesis and crystallography studies [259, 260, 258]. The atom pairs used to define distances were: LYS 514 CE - ATP N6, PHE 487 CD2 - (d)ATP C6, and ARG 559 NH2 - (d)ATP O2A. Results are shown both as distances vs simulation time and Potential Mean Force (PMF) plots versus atomic distance (Figure 5.2B). For LYS

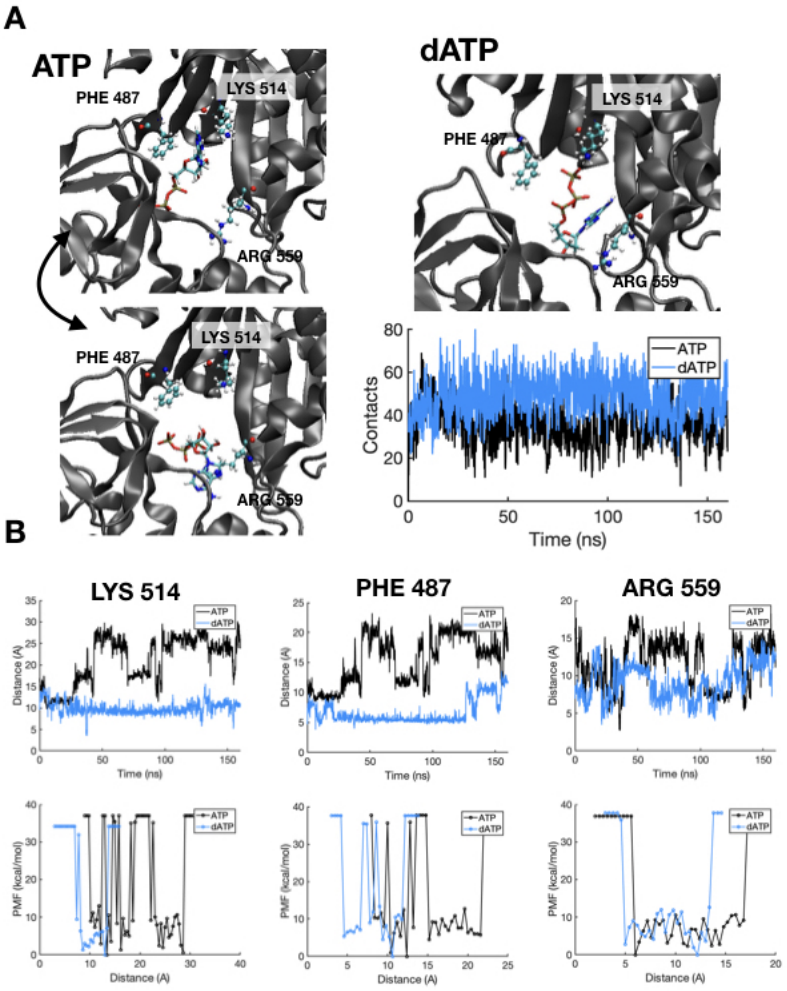

Figure 5.2. Differences between ATP and dATP interactions with the nucleotide binding pocket. (A) Visualized interactions between ATP/dATP (licorice) and relevant binding pocket residues PHE 487, LYS 514, and ARG 559 (ball and stick) residues within cytosolic SERCA domains (grey ribbon). Left, ATP demonstrates two major positions within the binding pocket, alternating between close interactions with PHE487/LYS514 and moving dowanward in the pocket toward ARG 559. Top right, dATP holds a more stable position within the binding pocket, closer to all 3 highlighted residues. Bottom right, number of atomic contacts between nucleotide and SERCA as a function of simulation time. (B) Top, plots demonstrating distance between the nucleotide and 3 residues of interest as a function of simulation time. Bottom, energy plots displaying potential of mean force as a function of atomic distance. Atomic distances were measured as: LYS 514 CE - ATP N6, PHE 487 CD2 - (d)ATP C6, and ARG 559 NH2 - (d)ATP O2A. In all 3 cases, dATP favors closer interactions with the binding pocket than ATP. ATP also exhibits two energy wells for LYS 514 and PHE 487, indicating a bimodal interaction structure.

514, dATP shows a more stable interaction with an average distance of 9.895 Åand a standard deviation σ of 1.484. ATP demonstrates a bimodal interaction with the residue, with an average distance of 21.02 and a σ of 5.595. Similar results are seen for the interaction with PHE487: for ATP, the average distance is 15.42 with a σ of 4.205, and for dATP the average is 6.662 with a σ of 2.03. Interactions with ARG 559 are more similar between the two nucleotides, but dATP favors a slightly closer interaction (average: 9.107, σ: 2.346) than ATP (average: 11.69, σ: 3.234). PMF plots demonstrate that dATP low energy wells occur at lower distances for all three residues of interest. PMF plots for LYS 514 and PHE 487 indicate two low energy wells for ATP. For LYS 514, low energy wells occur near 14 and 25 Å, and for PHE 487 the low energy distances are at 10 and 18 Å.

Closer analysis of the nucleotides themselves reveal differential conformations of ATP and dATP throughout the simulation. In Figure 5.3A, 100 representative frames of either ATP (top) or dATP (bottom) are overlayed and visualized as lines. ATP occupies a more ”open” conformation at all frames, while dATP appears to occupy a folded conformation. Ramachandran-type plots were used to compare angles θ 1 through 6 as identified in Figure 5.3B. dATP shows a preference for more acute angles in θ_1 while ATP favors trans conformations in both θ_1 and θ_2. dATP also demonstrates more stability in θ_3 and θ_4, while ATP appears more flexible in these domains. dATP prefers gauche conformations in θ_5 while θ_5 in ATP tends to be closer to 0 degrees. In Table 5.1, average and standard deviations of all angles are provided for both ATP and dATP. Standard deviations are significantly higher for dATP than ATP in θ_2, and θ_5 which are reflected by dispersed points in the Ramachandran-type plots. Conversely, θ_4 has a higher standard deviation in ATP than dATP and this is reflected through angle dispersion in the plots. Overall, nucleotide dihedral angles and overall molecule shape are makedly different between ATP and dATP, which likely affects the interactions between the nucleotide and protein residues within the N domain.

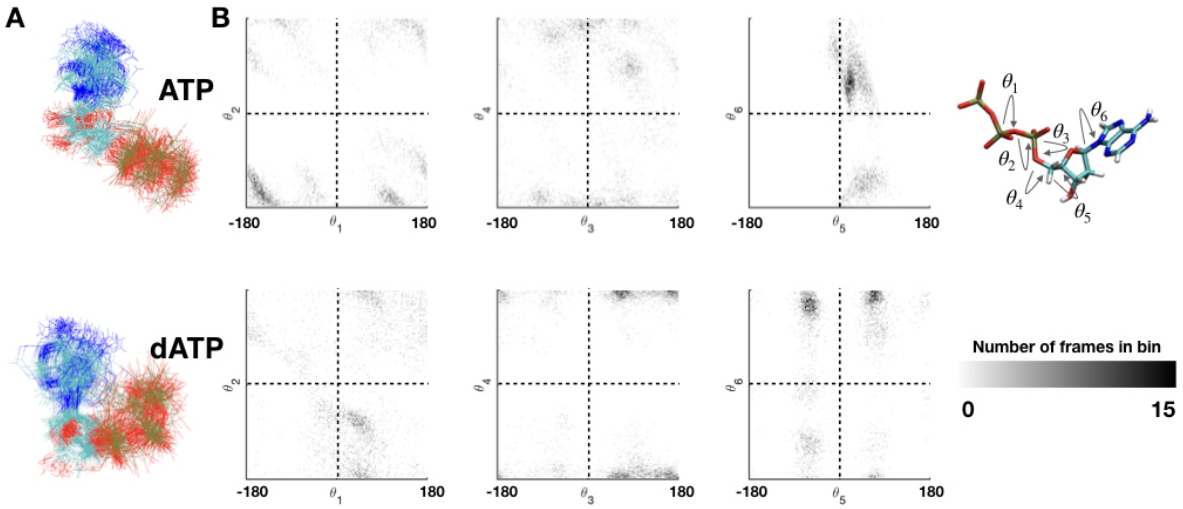

Figure 5.3. (A) Overlays of 100 frames each from ATP and dATP simulations demonstrating differential conformation of the nucleotides. (B) Ramachandran-type plots indicating favorable dihedral angles at 6 different points along the nucleotide. Top, ATP plots. Bottom, dATP plots. dATP shows a preference for more acute angles in θ_1 while ATP favors trans conformations in both θ_1 and θ_2. dATP also demonstrates more stability in θ_3 and θ_4, while ATP appears more flexible in these domains. dATP prefers gauche conformations in θ_5 while θ_5 in ATP tends to be closer to 0 degrees.

Table 5.1. Standard deviation and average values of various dihedral angles for ATP and dATP over a 160 ns GaMD simulation, as defined in 5.3

Dihedral Angle	ATP Average	ATP σ	dATP Average	dATP σ
θ_1	-149.4	52.88	52.16	59.94
θ_2	-152.2	36.71	178.9	60.51
θ_3	4.411	85.03	81.09	73.71
θ_4	176.2	61.83	178.6	28.43
θ_5	27.26	27.66	43.29	64.36
θ_6	166.9	69.6	155	49.86

5.4.2 Cytosolic domains separate as a result of nucleotide binding

Cytosolic domain movement in regions N, A, and P is key to the E1 to E2 transition by which Ca^{2+} is allowed to move into the SR lumen. To investigate the effects of ATP-versus dATP binding on these cytosolic domains, a distance analysis was performed by calculating the Cα - Cα distance between the following residue pairs in the same manner as a recent MD study [261]: T171-E679 (A-P), R489-E679 (N-P), K515-T171(N-A). Figure5.4 identifies the locations of these residue pairs, and displays distance-time plots as well as PMF energy landscape plots for apo, ATP, and dATP cases.

First considering the A-P domain interaction, both ATP and dATP binding stabilize a slightly more open conformation. For apo SERCA, the average distance between the domains was 28.35 Åwith a standard deviation of 0.4909. Both ATP and dATP had similar increases to the inter-domain distance (ATP: average= 28.86, σ = 0.368; dATP: average = 29.17, σ = 0.5367). Both nucleotides separate the domains, which is consistent with findings that the P and A domains separate to allow ATP to make contact with the phosphorylation site D315 [262]. dATP shows a slight tendency toward higher distances, with low energy conformations occurring in the 30 and 30.2 Åbins of the PMF plot, indicating that the presence of dATP may lead to faster phosphorylation of the protein due to farther A-P domain distances 5.4. Closing of the A and N domains has also been associated with the movement from SERCA E1(Ca) to E1P, but this appears to occur after the calcium binding step [263].

Another important step in the SERCA pump cycle is the opening of the N-P domain interface. This movement leads to rearrangement of transmembrane helices M1 - M6 which allows Ca^{2+} to escape into the SR lumen [262]. dATP exhibits a pronounced effect on the interdomain distances for this interface. For apo SERCA, the average N-P distance is 24.16 Åwith a standard deviation of 1.016. ATP bound SERCA demonstrates a slight opening of the domains and a more stable interaction, with an average distance of 24.88 Åand standard deviation of 0.6524. dATP bound SERCA results in even larger distances, with an average of

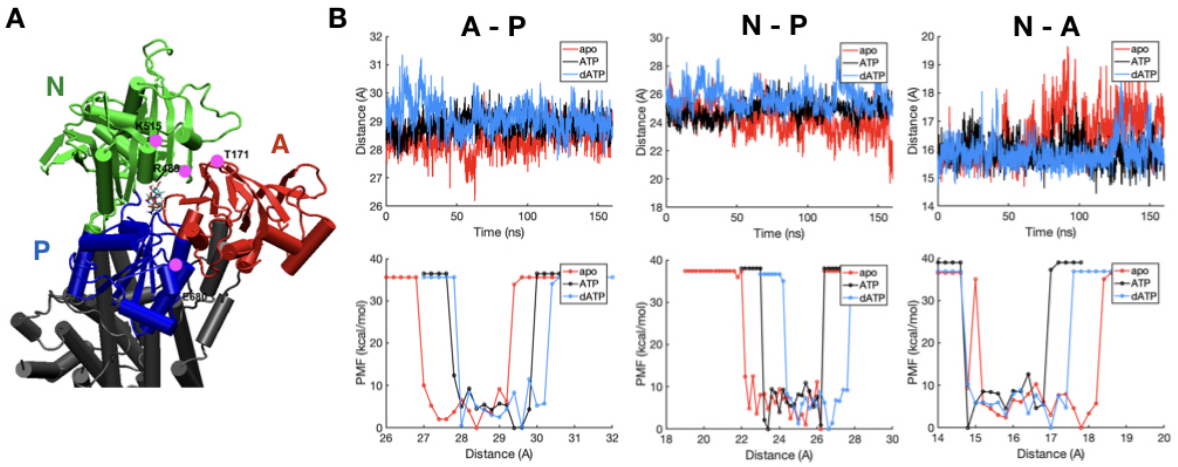

Figure 5.4. Effects of nucleotide binding to the cytosolic domains of SERCA. (A) A cartoon visualization showing the 3 cytosolic domains: N (green), A (red), and P (blue). Distances were measured between alpha carbons of: T171-E680 (A-P), R489-E680 (N-P), K515-T171(N-A). (B) Distance plots as a function of time, and PMF plots from GaMD reweighted data. For A-P, both ATP binding and dATP binding have similar increased effects on inter-domain distance. For N-P, ATP binding does not greatly increase the distance between the domains but dATP binding significantly increases inter-domain distance. For N-A, both ATP and dATP binding decrease the overall distance between the reference residues.

25.78 and standard deviation of 0.8388. The distance plot of the simulations shows that apo SERCA is trending toward a more closed N-P interface, whereas both ATP and dATP tend to stabilize the structure 5.4. Just as in the A-P case, dATP-SERCA demonstrates low energy states in the high distance realm of 26 - 28 Å, which indicates that the binding of dATP may facilitate the transition from cytosolic- to SR-facing SERCA.

The final cytosolic domain interaction is the N-A interface. The 110° hinging motion of the A domain is the most visible indicator of the transition between the ”open” and ”closed” SERCA conformations [264]. In this case, apo-SERCA favors the most open interface out of the 3 simulation cases. The average and standard deviation of inter-domain distances for the N-A interaction are as follows: (1) apo, average = 16.52, σ = 0.8466. (2) ATP, average = 15.91, σ = 0.449. (3) dATP, average = 15.87, σ = 0.5029. Lower standard deviations and averages for both ATP and dATP indicate that nucleotide binding stabilizes the structure in the

closed conformation. Although apo-SERCA trends toward a more open conformation as the simulation occurs, a full transition to the open state is not observed in any of the 3 cases 5.4. This is in agreement with recent FRET and MD studies showing that SERCA prefers the closed conformational state, but is often crystallized in the open state perhaps due to a local energy minimum in solution [265, 263].

5.4.3 Nucleotide binding stabilizes the interactions between Transmembrane Regions crucial to Ca^{2+} binding

The transmembrane helices of SERCA are the Ca^{2+}-binding region. Speficially, Sites I and II are located between helices M4, M5, M6, and M8, as visualized in the top left of Figure 5.5 [262, 264]. To investigate interhelical distances, the center of mass of the following atom pairs were used: : TM5 E770 CD - TM6 D799 CG, TM5 E770 OE1 - TM8 E907 OE2,TM6 D799 CG - TM8 907 OE. From the PMF plots in Figure 5.5, it appears that dATP and ATP have a nearly identical effect on inter-helix distances between TM5 and TM6 as well as TM5 and TM8. Specifically, apo-SERCA shows a preferred distance range of 6-8 Åfor TM5-TM6, but both ATP and dATP result in a smaller low energy window from 6.5 to 8 Å. This stabilization is also apparent from the standard deviations of the distances. For the TM5-TM6 interhelical distance, the standard deviations are 0.2563 for ATP and 0.2533 for dATP, while the standard deviation for the apo case is 0.4797. For the TM5-TM8 distances, the standard deviations for ATP and dATP SERCA are 0.3988 and 0.2533, respectively, while the apo standard deviation is 0.7219.

A slightly different trend can be extracted from the interactions between TM6 and TM8, which encompass the boundary of Ca^{2+} site I. in the apo case, the average interhelical distance is 6.439 Åand the standard deviation is 0.2972. For ATP, the average distance is 6.253 Åwith a standard deviation of 0.2593. In the case of dATP-SERCA, the average distance is 6.227 Åwith a standard deviation of 0.2692. Both ATP and dATP binding result in smaller interhelical distance, but the closure of these two domains is more pronounced in the case of dATP-bound

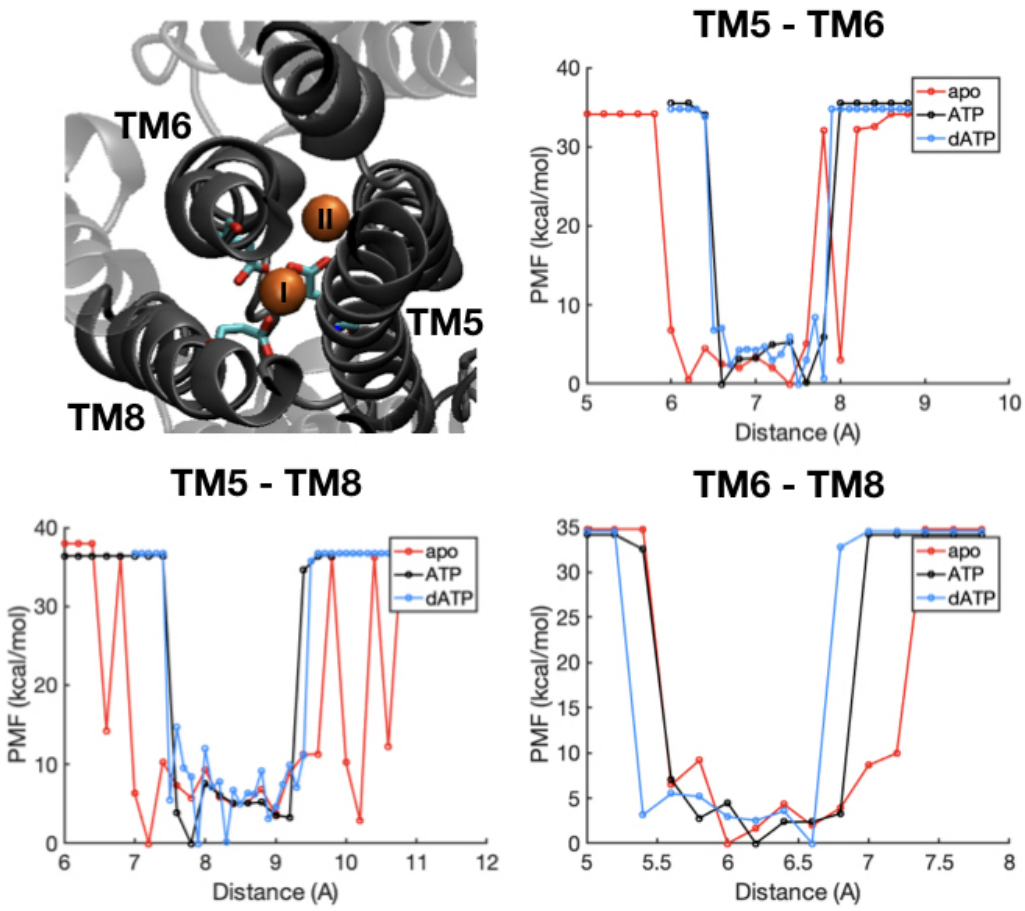

Figure 5.5. Top left, structure diagram of the TM helical structure in the Ca^{2+} binding region. SERCA is visualized in grey new cartoon, Ca^{2+} ions are orange spheres. Highlighted licorice residues were used to calculate interhelical distances: TM5 E770, TM6 D799, and TM8 E907. Energy landscapes describe the potential of mean force as a function of TM region distance. Distances were measured as: TM5 E770 CD - TM6 D799 CG, TM5 E770 OE1 - TM8 E907 OE2, TM6 D799 CG - TM8 907 OE. For both TM5-TM6 and TM5-TM8, both ATP and dATP binding both have identical effects of stabilizing the distance between the helices. For TM6-TM8, however, both ATP and dATP stabilize a closer structure between the helices, with dATP having a slightly more pronounced effect.

SERCA. Smaller distances between TM6 and TM8 may result in a hindered path for Ca^{2+} into Site I and an opening of the helices around Site II for facilitation of Ca^{2+} binding.

5.4.4 dATP-bound SERCA demonstrates altered Ca^{2+} affinity in Sites I and II compared to ATP-bound SERCA

Brownian Dynamics (BD) studies were performed to investigate the differential binding of ATP and dATP to the SERCA pump, as well as the Ca^{2+} association into both Site I and Site II for ATP- and dATP-bound SERCA. Nucleotide association rates were found to differ between ATP and dATP simulations testing interactions with the lowest energy structure from GaMD apo SERCA simulations. The ATP association rate was set to 2.59e+06 1/(M*s) based on model optimization of the Himeno calcium handling model [241] to a wildtype calcium transient from a dATP study on rat cardiomyocytes from Korte at al (Table 5.2 [73]. The WT ATP association rate was the output of BrownDye simulations when the reaction distance for association was 5.49 Å(where 3 atom pairs outlined in the methods were required to be within the reaction distance for a reaction event to occur). Using the same simulation criteria and a reaction distance of 5.49 Å, the dATP association rate was found to be 4.7177e+06 1/(M*s). This represents an 80% increase in association rate over ATP. This analysis suggests that in a cardiac system with elevated levels of dATP, dATP will competitively bind SERCA and may affect SERCA pump function even at low therapeutic levels of 2-5% of the overall ATP pool.

Similar Brownian Dynamics studies were performed on ATP-bound and dATP-bound SERCA to test association rates with Ca^{2+} in both Site I and II. Figure 5.6 displays association rate as a function of define reaction distance. A specific association rate was not chosen, but it is assumed that the propser association rate is in the low 10^9 range due to the outcome of a similar Brownian Dynamics study, which found the association rate of Ca2+ to site I to be 3.13e+09 [266]. For the range of reaction distances displayed in Figure 5.6, an interesting phenomenon can be observed. In the case of ATP-bound SERCA, Ca^{2+} binds Site I at significantly higher rates than Site II. This is in agreement with mechanistic understanding in the field, which

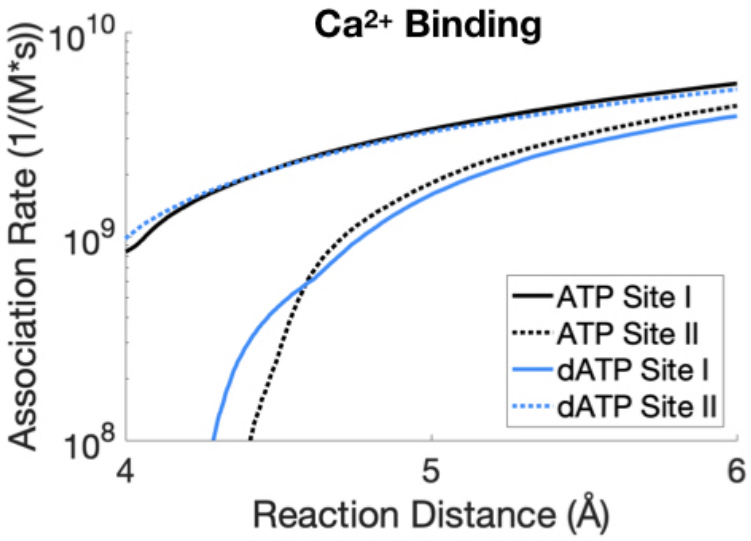

Figure 5.6. Results of Brownian Dynamics simulations of Ca^{2+} binding ATP-or dATP-bound SERCA after GaMD was used to generate the lowest energy structure in each case. Rates are plotted as a function of reaction distance due to the uncertainty in the Ca^{2+} on rates from experimental data. ATP data is in black, with Site I binding as a solid line and Site II as a dotted line. dATP data is in cyan, with Site I solid and Site II dotted. Site II has much lower association rates than Site I for the ATP-bound structure, but the opposite is true for dATP-bound SERCA.

suggests that Ca^{2+} first binds Site I and then a cooperative binding mechanism increases Ca^{2+} binding affinity for Site II [267, 268, 269]. However, in the dATP case the opposite results occur. Ca^{2+} association in Site II is nearly identical to the ATP-Site I association rates, whereas Site 1 binding in the dATP case can be an order of magnitude less, or even more pronounced at reaction distances between 4 and 4.5 Å. This finding leads us to explore alternative Ca^{2+} pathways within the transmembrane region which may explain the affinity reversal.

There are two main pathways by which Ca^{2+} is thought to enter the transmembrane region. The L1 pathway exists near residues D812, D814, and D817 [270], and the L3 pathway is located near residues near residues E51, E58, D59, and D109 [271, 272], as described in Huang et al [267]. Recent MD studies suggest that the L3 pathway is the main entry point for Ca^{2+}, so we focus on this larger pathway for the purposes of this study [273]. We explored the lowest-energy structures of both ATP- and dATP-bound SERCA to investigate possible

mechanisms by which Site II binding is preferred in the dATP-bound case. In visual inspection of the transmembrane region (Figure 5.7A), it appears that the L1 region is conserved between ATP-and dATP-bound SERCA. However, there appears to be a flipdown of D109 in the dATP case (rightmost residue highlighted) which may alter the shape of the L3 pathway significantly. Indeed, upon generating an electrostatic map of ATP- and dATP-bound SERCA (Figure 5.7B, red = 3.0 kT/e, blue= +3.0 kT/e), there is a clear difference between the electrostatic surfaces of L3 in the two simulation cases. in the dATP case, the L3 portal is consolidated slightly lower into the transmembrane region, and appears to have a ”U” shape rather than the more condensed L3 shape in the ATP case. We also notice different electrostatic surfaces on the SR luminal side, which appears to have 2 portals in the ATP case but one consolidated pathway in the dATP case.

It is well accepted that E309 acts as a gating residue for cooperative binding of Ca^{2+} to SERCA [274, 262]. In this capacity, E309 serves as a shield when no Ca^{2+} is bound within the transmembrane pump, so Ca^{2+} ions which enter through the L3 region are forced to bypass Site II and bind Site I. After Site I binding occurs, E309 undergoes a flip which opens Site II. In Figure 5.7C, we outline the differing position of E309 in lowest energy conformations of apo, ATP-bound, and dATP-bound SERCA. The diagram shows the position of E309 as well as D799, which is an important residue in Site I binding, and E58 which marks the bottom of the L3 pathway. The diagram also displays the center of mass atomic distance between Site II Ca^{2+} and E309 C. E309 is closest to the Site II Ca^{2+} in the apo state with a distance of 6.57 Å. The residue moves upward slightly in the TM region in the ATP case, where the distance is 7.33 Å. In the dATP case, E309 appears to have moved fully above the Site II Ca^{2+} and has a distance of 8.94Å. The L3 pathway is at the top right of this figure, which means Ca^{2+} is presumed to move downward into the TM region until it encounters E309. In the apo and ATP case, it is intuitive to see the shielding mechanism by which E309 blocks Site II and forces Ca^{2+} to move into Site I for binding. However, in the ATP case the shifting of E309 appears to have the

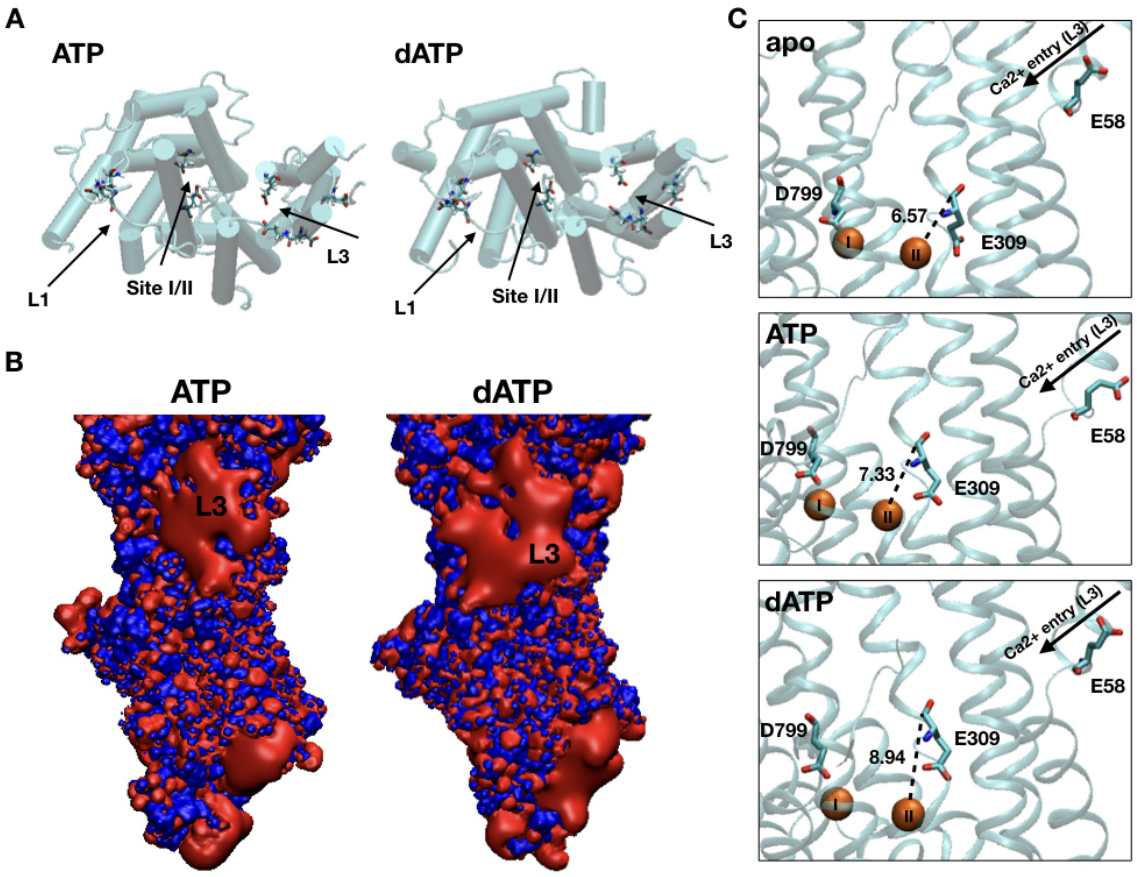

Figure 5.7. Investigation of probable Ca^{2+} entry pathways into Sites I and II. (A) Top-down view into the transmembrane region, with TM helices represented as cyan cylinders. Likely Ca^{2+} entry pathways L1 and L3 are highlighted, along with associated residues D812, D814, D817 (L1) and residues E51, E58, D59, and E109 (L3). In the dATP case, E109 appears to flip downward and create a different pathway for Ca^{2+} through L3, although the L1 pathway appears unchanged between the two cases. (B) Electrostatic depictions of SERCA, with the large negative L3 region highlighted. In the dATP case, the L3 pathway appears broken up by the presence of positive residues on the surface, and appears to indicate a lower pathway for Ca^{2+} entry into the transmembrane region. (C) Representative structures of apo (top), ATP-bound (middle) and dATP-bound (bottom) SERCA illuminate a potential explanation for why dATP binding causes Site II to become more Ca^{2+} sensitive. Transmembrane helices are displayed in cyan new cartoon, and residues D799, E309, and E58 are highlighted as licorice. Orange spheres depict the locations of Ca^{2+} in Site I and II, and direction of Ca^{2+} entry through the L3 pathway is highlighted with a black arrow in the top right of each image. E309, the recognized gating residue, normally sits almost parallel to Ca2+ site II, forcing calcium to bypass Site II and first bind Site I. In the dATP-bound SERCA case, E309 moves upwards in the transmembrane region, potentially allowing Ca^{2+} to bind Site II first by moving underneath the residue.

opposite effect. Namely, the residue has moved upwards within the region and blocks entry into Site I, encouraging Ca^{2+} ions to move underneath the residue and bind to Site II. The changing position of E309, combined with the observed lower L3 region as visualized with electrostatics, suggest that dATP-bound SERCA may preferentially bind Ca^{2+} in Site II rather than Site I.

5.4.5 Differential nucleotide and Ca^{2+} association rates contribute to experimentally observed calcium transients in dATP-treated human cells

As described in the Methods section, the Himeno model was optimized to WT calcium transient data using Particle Swarm Optimization (PSO). Parameters adjusted were Amp_{SERCA}, Amp_{NCX}, Amp_{NaK}, f_n. Optimized WT parameters are documented in Table 5.2.

Within the Tran model, k_1^+ (rate of ATP binding to SERCA) and $k_{d,Cal}$ (dissociation constant for Ca2+ binding to SERCA) were altered based on the Brownian Dynamics simulation results [236]. At 5.5 Å, which is the reaction distance corresponding to the WT rate of ATP binding to SERCA (2.59e6 1/(M*s)), the dATP association simulations predicted an 82.2% increase in mucleotide binding rate (4.72e6 1/(M*s)). Since Ca^{2+} binding is assumed in the Tran model to be 100% cooperative, we chose the association rates from site 1 for ATP, and site 2 for dATP, which had the higher respective rates. We chose a relatively low reaction distance of 4 Ådue to the close proximity of the binding sites (6 Å) in order to eliminate the possibility that an association at one site may register as an association event for the other. At 4 A, the ATP-SERCA Ca^{2+} association rate to Site 1 was calculated as 8.403e8 1/(M*s), whereas the dATP Site II association rate was 9.733e8. This means that a 15.8% increase in the Ca^{2+} binding rate for dATP-SERCA at Site II was observed compared to the rate for ATP-SERCA at Site I, so $k_{d,Cal}$ was decreased by 15.8%. In Figure 5.8A, the dATP Ca^{2+} transient is simulated by altering only k_1^+ and $k_{d,Cal}$ in the model according to these BD calculations. The transient relaxation rate is increased, but only slightly (time to 50% decay of 285.3 ms compared to 307.1 ms for WT), and a good fit to the experimental data is not achieved. Next, PSO was used

Table 5.2. Optimized values for WT and dATP-treated Ca^{2+} transients based on the Himeno et al model of calcium handling.

Parameter	WT Optimized Value	Optimized dATP Values (SERCA Only)	Optimized values for other pumps (calculated individually)
Amp_{SERCA} (mM/ms)	94.47	94.47	
Amp_{NCX} (mM/ms)	128.52	128.52	421.8
Amp_{NaK} (mM/ms)	17.77	17.77	170.5
Amp_{PMCA} (mM/ms)	0.19	0.19	2.1
f_n	1.37	1.37	
k_1^+ 1/(M*s)	2.59e6	**4.72e6**	
k_2^+ 1/(mM*s)	2540	**3716**	
$k_{d,Cal}$ (mM)	0.0027	**0.0023**	

to optimize another SERCA-related rate k_2^+, which is determined by ADP dissociation and the E1-E2 conformational transition. When optimizing for this rate as well as the BD rates, a very close fit is achieved with a time to 50% decay of 256.4 ms compared to the dATP experimental value of 240.2 ms. k_2^+ optimized results are displayed in Figure 5.8B and rates are displayed in column 3 of Table 5.2. The best fit required a 46% increase in k_2^+, from 2540 1/(mM*s) to 3716 1/(mM*s). With these optimized dATP parameters, the maximum flux through the SERCA pump was increased by 30% as shown in Figure 5.8C.

Further, we investigated whether adjusting the flux of other Ca^{2+}-ATPases may allow for fitting of the dATP experimental data. Amp_{PMCA}, Amp_{NaK}, and Amp_{NCX} (amplitudes of the Plasma Membrane Ca^{2+} ATPase, Na^+/K^+ ATPase, and Na^+/Ca^{2+} exchanger, respectively) were each optimized separately to determine whether a dATP-based effect on these pumps may provide realistic Ca^{2+} transients. All optimization was done with PSO using the altered ATP and Ca2+ binding rates from Brownian Dynamics simulations as described above. The output

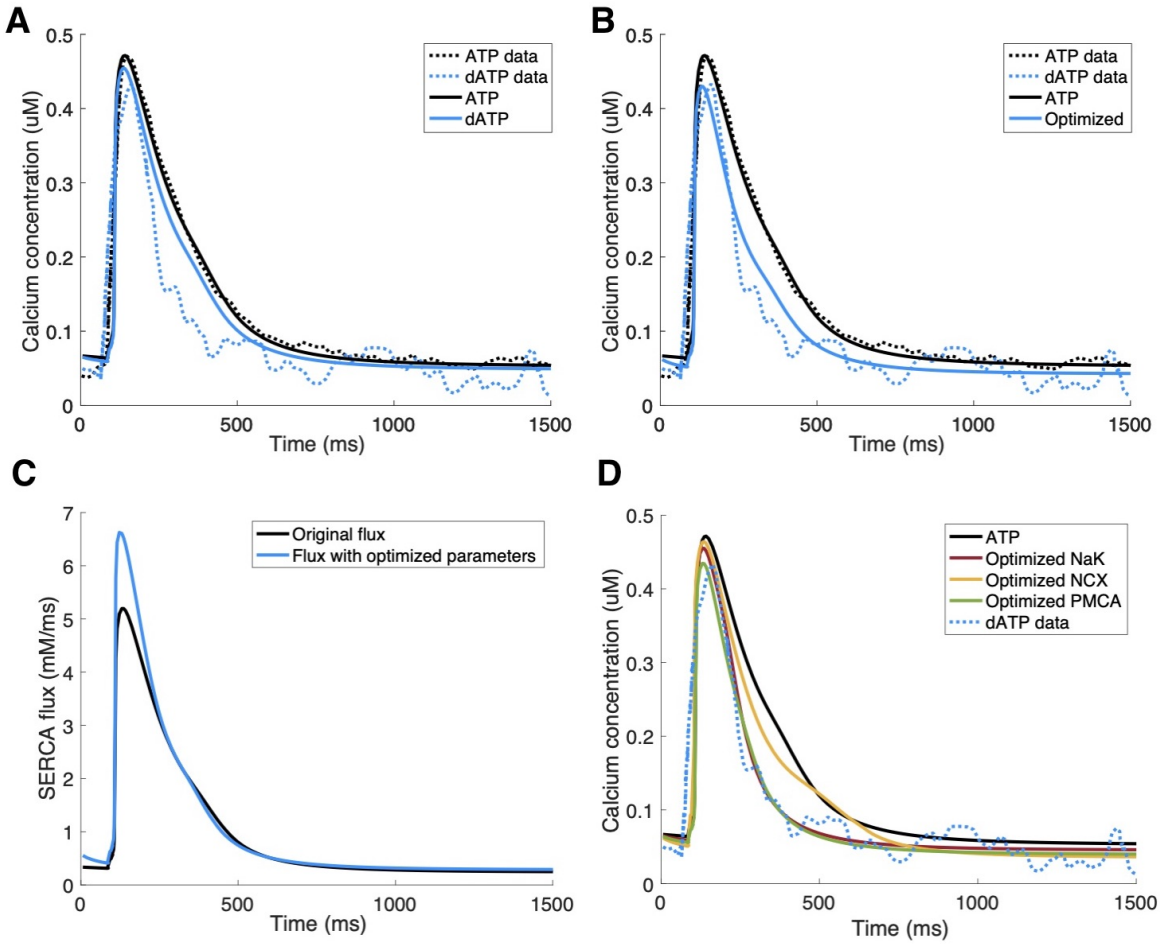

Figure 5.8. Calcium transient modeling using ref. [241]. Optimized WT (ATP) simulated curve is displayed as a solid black line. Experimental Ca^{2+} transient for WT (black dotted line) and dATP treatment (blue dotted line) from [73]. (A) ATP Ca^{2+} transient (solid cyan) when altering only the ATP binding rate and Ca2+ binding rate (4A reaction distance) based on BD results. (B) Optimization to dATP experimental curve (Simulation: Solid cyan, experiment: dotted cyan) by altering SERCA parameter k_{2+} (ADP dissociation) in the Tran model, in addition to BD parameter changes included in (A). (C) SERCA flux, in mM/ms, for WT optimized simulation (Solid black) and dATP optimized curve from (B). (D) dATP optimized Ca2+ transients when adjusting the flux of of PMCA (Green line), NCX (Yellow line) or NaK pump (Red line), after changing the ATP binding rate and Ca2+ binding rate in the same way as (A).

transient after optimization for each of the 3 cases is displayed in Figure 5.8D and optimized values can be found in Table 5.2. In the case of NaK pump optimization, a 9.6 fold increase was required to achieve a best fit. The time to 50% relaxation was decreased to 244.0 ms, providing a good fit to experimental data (in which time to 50% relaxation was 240.2 ms). Optimizing NCX resulted in a worse fit, with a time to 50% relaxation of 279.0 ms. PMCA optimization had a similar outcome to NaK optimization, with an 11 fold increase in Amp_{PMCA} resulting in a time to 50% relaxation of 246.9 ms. These results provide evidence that PMCA and NaK may be candidates for future investigations of dATP effects on Ca^{2+} handling. Indeed, some combination of increases to k_2^+, Amp_{PMCA}, and Amp_{NaK} may be the mechanistic solution for the transient effects, although an analysis of this interplay would require further molecular study to constrain the model to a single solution.

5.5 Discussion and Conclusions

The results outlined in this study constitute several pieces of evidence which may contribute to improved SERCA pump function in dATP treatment. Firstly, the separation of cytosolic domains A and P indicates faster phosphorylation of dATP-SERCA compared to ATP-SERCA. A-P domain separation is associated with nucleotide movement toward the D315 phosphorylation site [262]. dATP-bound SERCA results in increased N-P cytosolic domain distance which is a precursor to Ca^{2+} release into the cytosol. Our simulations did not capture the major protein pumping movement due to the requirement that Ca^{2+} bind before phosphorylation and movement to the SR facing state of SERCA occurs [263]. Transmembrane helices TM6 and TM8 move closer together after dATP binding to SERCA, which may serve to occlude Site I as the initial binding site for Ca^{2+}.

We also found that in dATP-bound SERCA, Ca^{2+} associates first to Site II rather than the well understood mechanism of Site I binding followed by cooperative Site II binding [267, 268, 269]. This differential affinity is due to rearrangement of the L3 Ca^{2+} binding

pathway as well as upward movement of gating residue E309 within the transmembrane region. The L3 region is seen as the most viable Ca^{2+} entry point because the negatively charged residues in the region contribute to a strongly negative electrostatic potential surface, which will in turn attract cations. Therefore, the lower and differently shaped L3 negative surface potential we observed in the case of dATP-bound SERCA may allow Ca^{2+} ions to more easily enter Site II by entering below E309. Additionally, E309 moves upwards away from Site II in the dATP case compared to apo and ATP-bound SERCA, which further served to block Site I entry and allow the first binding event to happen at Site II. The overall association rates for dATP at Site II are similar to ATP Site I association rates. This observation indicates that the rearrangement of L3 does not affect the overall affinity of Ca^{2+} in the transmembrane region, but rather serves to shuttle Ca^{2+} into a different site after passing through L3. dATP demonstrates an 80% higher association rate than ATP to the N domain of SERCA, which indicates that the effects of increased dATP in the cytosol may outpace the levels of dATP in the system, and that dATP can indeed competitively bind SERCA 2A.

Inputting the BrownDye-gathered rates of dATP versus ATP association and Ca^{2+} association (k_1^+ and $k_{d,Cal}$) did not allow us to fully recreate the experimental Ca^{2+} transient, but it appears that dATP involvement in the SERCA pump cycle may have larger downstream affects on protein conformation which may further contribute to the steeper transient relaxation during dATP treatment. In fact, increasing rate k_2^+ by only 46% in addition to altering the BD rates allowed for a good match to the experimental dATP calcium transient. There are also other ATPases which contribute to the calcium transient such as PMCA, NaK and NCX, which are found to improve transient relaxation kinetics when their fluxes are increased in the ODE model. Likely, some combination of SERCA upregulation and these other pumps together provide the mechanism for improved relaxation during dATP treatment. In order to explore further downstream effects of dATP on SERCA function, further MD studies should be conducted on Ca^{2+}-bound SERCA with either ATP or dATP bound to investigate the large-scale movements

associated with Ca^{2+} escape into the SR lumen (E1-E2 transition, or rate k_2^+). MD studies with calcium bound would also serve to answer a crucial question about cooperative binding - when the first calcium ion binds Site II rather than Site I, does the same cooperative binding process occur? Is it more or less cooperative than the traditional pathway?

As in previous BrownDye studies exploring Ca^{2+} - SERCA association [266], our Ca^{2+} association rates were higher than experimental results have predicted. In fact, the on rates predicted from experimental data were in the range of 10^6 to 10^8, and our calculated rates were in the range of 10^9 to 10^{10}, one to four orders of magnitude higher than expected [266, 269]. There are several reasons for the overestimation of these rates. Firstly, our BrownDye simulations did not include any lipids, which would serve to provide significant steric hindrance to calcium attempting to enter the TM region. Additionally, the simulations begin by generating calcium randomly on a spherical surface surrounding the protein. In the physiological system, Ca^{2+} ions are presumed to enter Sites I and II through the cytosolic side, and a lipid bilayer separates the Ca^{2+} pool in the cytosol from that of the SR. Therefore, it is important to interpret the results as evidence that SERCA has high affinity for Ca^{2+} due to the large negative electrostatic surface potentials in the transmembrane region, and that SERCA has much higher affinity for Site I than site II (in the ATP case) or vice versa (in the dATP case).

This study is the first to model cardiac isoform SERCA 2A, although multiple MD studies have been performed on other isoforms more common in skeletal muscle [261, 267, 266, 274, 275, 270]. Due to our investigation of dATP as a specific treatment for cardiac muscle, this was an ideal case study to investigate a new crystal structure of SERCA. Additionally, to our knowledge this is the first study to investigate directly the effects of nucleotides bound to Ca^{2+}- free SERCA. We were able to demonstrate the stabilizing effect of nucleotide binding to the cytosolic domain and the effects of ATP versus dATP on Ca^{2+} affinity. This study has demonstrated the power of multiscale modeling for investigating the effects of ATP analogs

on cardiac cells, as we integrated knowledge from the atomic to the cellular level to uncover potential mechanisms of dATP which scale up to a significantly altered calcium transient and cardiac function as a whole.

5.6 Acknowledgements

Chapter 5, in full, is currently being prepared for submission for publication of the material: McCabe KJ, Hirakis SP, Teitgen AE, Duclos A, Regnier M, Amaro RE, and McCulloch AD. "A multiscale computational modeling study to determine the effects of 2-deoxy-ATP on SERCA pump function". *(in preparation).* The dissertation author was the primary investigator and author of this material.

Chapter 6

Conclusion

Broadly, this dissertation seeks to answer questions about cardiac mechanics mechanisms by bridging spatial and temporal gaps using a variety of computational techniques. On the atomistic scale, Gaussian accelerated Molecular Dynamics studies are performed to determine the effects of small molecule dATP on a calcium ATPase. Scaling up slightly, we use Brownian dynamics modeling employing rigid body molecular interactions to determine association rates between a variety of species including: tropomyosin-actin filament for thin filament activation insights, myosin-actin to probe crossbridge cycling dynamics, and nucleotide-SERCA to test effects of dATP on calcium handling processes. Subcellularly, ODE and Monte Carlo Markov state models of the sarcomere are developed to test the effects of DCM-associated mutations as well as drug treatment on cardiac contractility. A cellular ODE model of calcium handling allows us to test drug effects on the calcium transient of the cardiomyocyte. Rather than using these models separately, they are coupled together across scales in an attempt to add detail into complex models of cardiac function and integrate the most relevant information in order to solve problems in cardiac physiology.

In Chapter 1, Molecular Dynamics simulations of troponin C determine differential conformations of the protein as a result of DCM-associated mutations D75Y, E59D, and G159D, especially focusing on a critical protein-opening step which precedes further thin filament activation. Brownian dynamics modeling is also employed to determine calcium binding rates

for the three mutations of interest. The rates determined from these two steps in the thin filament activation process are then integrated into transition rates for an ODE Markov State model of sarcomere activation and force production in order to predict the effects of the mutations on overall contractility. The mixed success of this study provides a crucial lesson regarding the challenges of integrating across scales using simplified systems.

Chapter 2 consists of a Brownian Dynamics study of tropomyosin-actin interactions, testing 19 different locations of Tm movement azithumally around an actin filament for differences in association rate. Specific association rates in this case are not integratable as rate constants for higher order models because the Tm-actin interaction involves a sliding motion where the molecules stay in close contact at all times rather than a standard binding interaction. However, investigation of the association rates as a function of Tm position on the filament reveal a multi-well association profile which closely matches known preferential positions of Tm measured experimentally. This work has provided the basis of a unique Tm activation energy landscape which can be used in stochastic ODE (SODE) modeling of thin filament activation, and demonstrates the strong electrostatic influence behind the preferred positions of trpopmyosin on the actin thin filament.

The remaining chapters re-orient the physiological framework slightly by focusing on mechanisms of dATP as a cardiac therapeutic. In Chapter 3, a combination of electrostatics analysis using APBS and association studies using Brownian dynamics are used to explore the effects of dADP versus ADP binding on acto-myosin interactions. First, the actin-myosin binding region is probed to find differences in contact residue pairs. More polar residues are found to come in contact with each other after dADP binding, which suggests a higher likelihood of hydrogran binding and more stable interactions. Then, a Brownian dynamics study of rigid myosin and actin allows us to discover the electrostatics-driven differences in association rate with ADP- or dADP-bound myosin. Irrespective of the simplified actin representation and the reaction distance chosen, association rates were higher with dADP-bound

myosin, indicating higher electrostatic affinity which was first hypothesized in [79].

Next, the Brownian dynamics results are integrated into a Monte Carlo Markov State model of the sarcomere in Chapter 4. We built a 5-state lumped parameter model which accounts for Ca^{2+} binding, thin filament activation via Tm movement into the Closed and Open states, and XB cycling (both pre- and post- powerstroke modelled separately) with functionality for competitive ATP- and dATP-binding. After initial optimization to experimental data from Regnier et. al. [67], rates from Brownian dynamics acto-myosin association studies were directly incorporated into the model and allowed for a unique set of increases to attachment, powerstroke, and detachment rates that agrees with experimental findings. We were also able to reproduce the phenomenon of positive nonlinear steady-state force increases as a function of percent dATP [69]. Twitch simulations also allowed us to demonstrate computationally the contractile augmentation which occurs even at low dATP levels. This study allowed for quantification of the effects of dATP treatment on the three major transitions which make up XB cycling for the first time.

Finally, our investigation turned to the impact of dATP on SERCA, which provides insights into mechanisms of experimentally observed increases in Ca^{2+} relaxation during dATP treatment [73]. In Chapter 5, 160 ns simulations of apo, Mg^{2+}ATP-bound, and Mg^{2+}dATP-bound SERCA 2A were performed and analyzed. dATP was observed to make more contacts with the SERCA 2A mucleotide binding pocket than ATP, and adopted a disparate dihedral angle pattern throughout the molecule. dATP displayed an 80% increase in association rate to apo SERCA compared to ATP, highlighting the potential for competitive dATP binding in an elevated dATP treatment environment. dATP-SERCA was also found to prefer slightly more open cytosolic interfaces between the N-P domains and the A-P domains, which may predict faster phosphorylation and pump function. Key transmembrane helices became stabilized by the presence of both nucleotides. In the case of dATP-SERCA, the shape of the Ca2+ L3 binding pathway was altered and set slightly lower into the transmembrane region. This,

combined with upward movement of gating ligand E390, suggests that Ca^{2+} follows a different path for Ca^{2+} binding than ATP or apo SERCA. In fact, Brownian dynamics modeling showed that dATP-SERCA has higher association rates for Ca^{2+} binding Site II than Site I, which is the opposite of the ATP-SERCA findings. Although this study gives an incomplete picture of the effects of dATP on SERCA function, there are strong indications that dATP binding enhanges the SERCA pump cycle which may explain the enhanced calcium transient relaxation present during dATP treatment.

As outlined in the chapters above, the modeling methods herein contain challenges and limitations. In the case of MD modeling, the short timescales studied make it difficult to visualize major conformational changes in the protein. Two methods herein worked to combat this issue: in chapter 1, the Anton supercomputer allowed us the computational power to extend MD simulations to the multiple μs timescale. In Chapter 5, GaMD was employed to boost protein energies in an attempt to sample a wider range of energetic conformations over a short timescale. Additionally, MD modeling must be performed in a relatively small and simplified system due to the complex nature of the calculation of forces at every atomic position. Therefore, it is difficult to investigate the effects of multiple proteins interacting in the case of the sarcomere or calcium handling. In BD simulations, the system is simplified even further into a set of rigid bodies and an implied solvent, which allows for much larger timescales but loss of atomistic detail regarding residue rearrangement in the binding region. Therefore, these simulations are most successful when one has experimental data to compare association rates (as in Chapter 1 and Chapter 4) or when one is investigating general electrostatic trends rather than exact quantification (as in chapters 2 and 5). Markov State models of the sarcomere were employed in Chapters 1 and 4 as a tool to integrate rate data gathered from smaller scale models. The ODE model in chapter 1 benefits from extremely fast solving time, but lacks the spatial detail necessary to investigate mechanisms of cooperative activation or details of crossbridge cycling. The Monte Carlo model used in Chapter 4 provides more detail, but requires longer

solve times due to the requirement of averaging hundreds of separate simulations dictated by random number generation. Even this model is greatly simplified, lumping crucial steps of protein-protein interaction at various stages of activation and relaxation. However, the addition of more explicit steps would lead to the problem of overfitting, as many individual transitions have not been experimentally measured and would require optimization. As in any model, these methods seek to maintain a delicate balance between detail and efficiency to answer specific questions of interest.

Whether investigating the effects of DCM-associated mutations or testing a drug which has promise as a treatment for DCM patients, multiscale modeling can answer a wide range of physiological questions which are unanswerable with current experimental techniques. The enclosed work is an exploration and application of the ways in which computational technologies at different scales can augment each other to fill the gaps in our understanding of cardiac mechanics.

Bibliography

[1] P. Richardson, W. McKenna, M. Bristow, B. Maisch, B. Mautner, J. OConnell, et al., Report of the 1995 world health organization/international society and federation of cardiology task force on the definition and classification of cardiomyopathies, Circulation 93 (1996) 841842. doi:10.1161/01.CIR.93.5.841.

[2] J. G. Seidman, C. Seidman, The genetic basis for cardiomyopathy: from mutation identification to mechanistic paradigms, Cell 104 (2001) 557567. doi:10.1016/S0092-8674(01)00242-2.

[3] S. Karkkainen, K. Peuhkurinen, Genetics of dilated cardiomyopathy, Ann. Med 39 (2007) 91107. doi:10.1080/07853890601145821.

[4] Q. Lu, X. Wu, S. Morimoto, Inherited cardiomyopathies caused by troponin mutations, J. Geriatr. Cardiol. 10 (2013) 91101. doi:10.3969/j.issn.1671-5411.2013.01.014.

[5] A. N. Chang, J. D. Potter, Sarcomeric protein mutations in dilated cardiomyopathy, Heart Fail Rev 10 (2005) 225235. doi:10.1007/s10741-005-5252-6.

[6] M. Kamisago, S. D. Sharma, S. R. DePalma, S. Solomon, P. Sharma, B. McDonough, et al., Mutations in sarcomere protein genes as a cause of dilated cardiomyopathy, N. Engl. J. Med 343 (2000) 16881696. doi:10.1056/NEJM200012073432304.

[7] D. Li, G. Z. Czernuszewicz, O. Gonzalez, T. Tapscott, A. Karibe, J. B. Durand, et al., Novel cardiac troponin t mutation as a cause of familial dilated cardiomyopathy, Circulation 104 (2001) 21882193.

[8] T. M. Olson, N. Y. Kishimoto, F. G. Whitby, V. V. Michels, Mutations that alter the surface charge of alpha-tropomyosin are associated with dilated cardiomyopathy, J. Mol. Cell. Cardiol 33 (2001) 723732. doi:10.1006/jmcc.2000.1339.

[9] J. Mogensen, R. T. Murphy, T. Shaw, A. Bahl, C. Redwood, H. Watkins, et al., Severe disease expression of cardiac troponin c and t mutations in patients with idiopathic dilated cardiomyopathy, J. Am. Coll. Cardiol 44 (2004) 20332040. doi:10.1016/j.jacc.2004.08.027.

[10] R. T. Murphy, J. Mogensen, A. Shaw, T. Kubo, S. Hughes, W. J. McKenna, Novel mutation in cardiac troponin i in recessive idiopathic dilated cardiomyopathy, Lancet 363 (2004) 371372. doi:10.1016/S0140-6736(04)15468-8.

[11] N. K. Lakdawala, L. Dellefave, C. S. Redwood, E. Sparks, A. L. Cirino, S. Depalma, et al., Familial dilated cardiomyopathy caused by an alpha-tropomyosin mutation: the distinctive natural history of sarcomeric dilated cardiomyopathy, J. Am Coll. Cardiol 55 (2010) 320329. doi:10.1016/j.jacc.2009.11.017.

[12] N. K. Lakdawala, B. H. Funke, S. Baxter, A. L. Cirino, A. E. Roberts, D. P. Judge, et al., Genetic testing for dilated cardiomyopathy in clinical practice, J. Card. Fail 18 (2012) 296303. doi:10.1016/j.cardfail.2012.01.013.

[13] T. Branishte, V. Minciuna, A. Braniste, Aspects of molecular mechanisms in myocardial hypertrophy, particular morphological changes and cell bioenergetic characteristics in patients with dilated cardiomyopathy., Rev. Med Chir. Soc. Med. Nat. Iasi 117 (2013) 851856.

[14] A. Prez-Serra, R. Toro, G. Sarquella-Brugada, D. de Gonzalo-Calvo, S. Cesar, E. Carro, et al., Genetic basis of dilated cardiomyopathy, Int. J. Cardiol 224 (2016) 461–472. doi:10.1016/j.ijcard.2016.09.068.

[15] J. A. Spudich, R. S. Rock, A crossbridge too far, Nat. Cell Biol 4 (2002) E8E10. doi:10.1038/ncb0102-e8.

[16] E. M. McNally, J. R. Golbus, M. J. Puckelwartz, Genetic mutations and mechanisms in dilated cardiomyopathy, J. Clin. Invest 123 (2013) 1926. doi:10.1172/JCI62862.

[17] J. A. Spudich, Hypertrophic and dilated cardiomyopathy: four decades of basic research on muscle lead to potential therapeutic approaches to these devastating genetic diseases, Biophys. J. 106 (2014) 12361249. doi:10.1016/j.bpj.2014.02.011.

[18] C. Du, S. Morimoto, K. Nishii, R. Minakami, M. Ohta, N. Tadano, et al., Knock-in mouse model of dilated cardiomyopathy caused by troponin mutation, Circ. Res. 101 (2007) 185194. doi:10.1161/CIRCRESAHA.106.146670.

[19] S. Morimoto, Q. Lu, K. Harada, F. Takahashi-Yanaga, R. Minakami, M. Ohta, et al., Ca2+-desensitizing effect of a deletion mutation delta k210 in cardiac troponin t that causes familial dilated cardiomyopathy, Proc. Natl. Acad. Sci. U.S.A 99 (2002) 913918. doi:10.1073/pnas.022628899.

[20] Q. Lu, S. Morimoto, K. Harada, C.-k. Du, F. Takahashi-Yanaga, Y. Miwa, et al., Cardiac troponin t mutation r141w found in dilated cardiomyopathy stabilizes the troponin t-tropomyosin interaction and causes a ca2+ desensitization, J. Mol. Cell. Cardiol 35 (2003) 14211427. doi:10.1016/j.yjmcc.2003.09.003.

[21] M. Mirza, S. Marston, R. Willott, C. Ashley, J. Mogensen, W. McKenna, et al., Dilated cardiomyopathy mutations in three thin filament regulatory proteins result in a common functional phenotype, J. Biol. Chem 280 (2005) 2849828506. doi:10.1074/jbc.M412281200.

[22] C. C. Lim, H. Yang, M. Yang, C.-k. Wang, J. Shi, E. A. Berg, et al., A novel mutant cardiac troponin c disrupts molecular motions critical for calcium binding affinity and cardiomyocyte contractility, Biophys. J. 94 (2008) 35773589. doi:10.1529/biophysj.107.112896.

[23] D. Dweck, D. P. Reynaldo, J. R. Pinto, J. D. Potter, A dilated cardiomyopathy troponin c mutation lowers contractile force by reducing strong myosin-actin binding, J. Biol Chem 285 (2010) 1737117379. doi:10.1074/jbc.M109.064105.

[24] M. Memo, M. Leung, D. G. Ward, C. dos Remedios, S. Morimoto, L. Zhang, et al., Familial dilated cardiomyopathy mutations uncouple troponin i phosphorylation from changes in myofibrillar ca2+ sensitivity, Cardiovasc. Res 99 65–73. doi:10.1093/cvr/cvt071.

[25] B. J. Biesiadecki, T. Kobayashi, J. S. Walker, R. J. Solaro, P. P. de Tombe, The troponin c g159d mutation blunts myofilament desensitization induced by troponin i ser23/24 phosphorylation, Circ. Res 100 (2007) 1486–1493. doi:10.1161/01.RES.0000267744.92677.7f.

[26] P. Robinson, M. Mirza, A. Knott, H. Abdulrazzak, R. Willott, S. Marston, et al., Alterations in thin filament regulation induced by a human cardiac troponin t mutant that causes dilated cardiomyopathy are distinct from those induced by troponin t mutants that cause hypertrophic cardiomyopathy, J Biol. Chem 277 (2002) 4071040716. doi:10.1074/jbc.M20.3446200.

[27] A. Kalyva, F. I. Parthenakis, M. E. Marketou, J. E. Kontaraki, P. E. Vardas, Biochemical characterisation of troponin c mutations causing hypertrophic and dilated cardiomyopathies, J. Muscle Res. Cell Motil. 35 (2014) 161 178. doi:10.1007/s10974-014-9382-0.

[28] J. R. Moore, L. Leinwand, D. M. Warshaw, Understanding cardiomyopathy phenotypes based on the functional impact of mutations in the myosin motor, Circ. Res 111 (2012) 375385. doi:10.1161/CIRCRESAHA.110.223842.

[29] P. Robinson, P. J. Griffiths, H. Watkins, C. S. Redwood, Dilated and hypertrophic cardiomyopathy mutations in troponin and alpha-tropomyosin have opposing effects on the calcium affinity of cardiac thin filaments, Circ. Res 101 (2007) 12661273. doi:10.1161/CIRCRESAHA.107.156380.

[30] J. Davis, L. C. Davis, R. N. Correll, C. A. Makarewich, J. A. Schwanekamp, F. Moussavi-Harami, et al., A tension-based model distinguishes hypertrophic versus dilated cardiomyopathy, Cell 165 (2016) 11471159. doi:10.1016/j.cell.2016.04.002.

[31] D. Dweck, N. Hus, J. D. Potter, Challenging current paradigms related to cardiomyopathies. are changes in the ca2+ sensitivity of myofilaments containing cardiac troponin c mutations (g159d and l29q) good predictors of the phenotypic outcomes?, J. Biol. Chem 283 (2008) 3311933128. doi:10.1074/jbc.M804070200.

[32] N. K. Lakdawala, J. J. Thune, S. D. Colan, A. L. Cirino, F. Farrohi, J. Rivero, et al., Subtle abnormalities in contractile function are an early manifestation of sarcomere mutations in dilated cardiomyopathy, Circ. Cardiovasc. Genet 5 (2012) 503510. doi:10.1161/CIRCGENETICS.112.962761.

[33] J. C. Tardiff, Its never too early to look: subclinical disease in sarcomeric dilated cardiomyopathy, Circ. Cardiovasc. Genet 5 (2012) 483486. doi:10.1161/CIRCGENETICS.112.964817.

[34] M. Ohba, R. Hosokawa, N. Kambara, E. Tadamura, M. Mamede, S. Kubo, et al., Difference in myocardial flow reserve between patients with dilated cardiomyopathy and those with dilated phase of hypertrophic cardiomyopathy: evaluation by 15o-water pet, Circ. J 71 (2007) 884890. doi:10.1253/circj.71.884.

[35] M. A. Burke, S. Chang, H. Wakimoto, J. M. Gorham, D. A. Conner, D. C. Christodoulou, et al., Molecular profiling of dilated cardiomyopathy that progresses to heart failure, JCI Insight 1 (2016) e86898. doi:10.1172/jci.insight.86898.

[36] F. Ahmad, S. K. Banerjee, M. L. Lage, X. N. Huang, S. H. Smith, S. Saba, et al., The role of cardiac troponin t quantity and function in cardiac development and dilated cardiomyopathy, PLoS ONE 3 (2008) e2642. doi:10.1371/journal.pone.0002642.

[37] M. Ramratnam, G. Salama, R. K. Sharma, D. W. R. Wang, S. H. Smith, S. K. Banerjee, et al., Gene-targeted mice with the human troponin t r141w mutation develop dilated cardiomyopathy with calcium desensitization, PLoS ONE 11 (2016) e0167681. doi:10.1371/journal.pone.0167681.

[38] J. Varguhese, Y. Li, Molecular dynamics and docking studies on cardiac troponin, C J Biomol Struct Dyn 29 (2011) 123135.

[39] S. Lindert, P. M. Kekenes-Huskey, G. Huber, L. Pierce, J. A. McCammon, Dynamics and calcium association to the n-terminal regulatory domain of human cardiac troponin c: a multiscale computational study, J. Phys Chem. B 116 (2012) 84498459. doi:10.1021/jp212173f.

[40] S. Lindert, Y. Cheng, P. Kekenes-Huskey, M. Regnier, J. A. McCammon, Effects of hcm ctni mutation r145g on troponin structure and modulation by pka phosphorylation elucidated by molecular dynamics simulations, Biophys. J. 108 (2015) 395407. doi:10.1016/j.bpj.2014.11.3461.

[41] J. J. Rice, P. P. de Tombe, Approaches to modeling crossbridges and calcium-dependent activation in cardiac muscle, Prog. Biophys. Mol. Biol 85 (2004) 179195. doi:10.1016/j.pbiomolbio.2004.01.011.

[42] S. Campbell, F. Lionetti, K. Campbell, A. McCulloch, Coupling of adjacent tropomyosins enhances cross-bridge-mediated cooperative activation in a markov model of the cardiac thin filament, Biophys J 98 (2010) 22542264.

[43] S. Dewan, K. McCabe, M. Regnier, A. McCulloch, S. Lindert, Molecular effects of ctnc dcm mutations on calcium sensitivity and myofilament activation-an integrated multiscale modeling study, J. Phys. Chem. B 120 (2016) 82648275.

[44] J. Hussan, P. P. de Tombe, J. J. Rice, A spatially detailed myofilament model as a basis for large-scale biological simulations, IBM J. Res Dev. 50 (2006) 583 600. doi:10.1147/rd.506.0583.

[45] J. Rice, F. Wang, D. Bers, P. de Tombe, Approximate model of cooperative activation and crossbridge cycling in cardiac muscle using ordinary differential equations, Biophys J 95 (5) (2008) 2368–90.

[46] S. Goktepe, O. J. Abilez, K. K. Parker, E. Kuhl, A multiscale model for eccentric and concentric cardiac growth through sarcomerogenesis, J. Theor. Biol 265 (2010) 433442. doi:10.1016/j.jtbi.2010.04.023.

[47] S. G. Campbell, A. D. McCulloch, Multi-scale computational models of familial hypertrophic cardiomyopathy: genotype to phenotype, J. R. Soc. Interface 8 (2011) 15501561. doi:10.1098/rsif.2011.0184.

[48] N. A. Trayanova, Whole-heart modeling: applications to cardiac electrophysiology and electromechanics, Circ. Res 108 (2011) 113128. doi:10.1161/CIRCRESAHA.110.223610.

[49] R. C. P. Kerckhoffs, J. Omens, A. D. McCulloch, A single strain-based growth law predicts concentric and eccentric cardiac growth during pressure and volume overload, Mech. Res Commun 42 (2012) 4050. doi:10.1016/j.mechrescom.2011.11.004.

[50] Y. Zhang, V. H. Barocas, S. A. Berceli, C. E. Clancy, D. M. Eckmann, M. Garbey, et al., Multi-scale modeling of the cardiovascular system: disease development, progression, and clinical intervention, Ann. Biomed. Eng 44 (2016) 26422660. doi:10.1007/s10439-016-1628-0.

[51] K. Tondel, S. Land, S. A. Niederer, N. P. Smith, Quantifying inter- species differences in contractile function through biophysical modelling, J. Physiol. 593 (2015) 10831111. doi:10.1113/jphysiol.2014.279232.

[52] A. Fabiato, Calcium-induced release of calcium from the cardiac sarcoplasmic reticulum, Am. J. Physiol. Cell Physiol. 245 (1983) C1C14.

[53] A. F. Huxley, R. Niedergerke, Structural changes in muscle during contraction; interference microscopy of living muscle fibres, Nature 173 (1954) 971973. doi:10.1038/173971a0.

[54] H. Huxley, J. Hanson, Changes in the cross-striations of muscle during contraction and stretch and their structural interpretation, Nature 173 (1954) 973976. doi:10.1038/173973a0.

[55] A. Gordon, E. Homsher, M. Regnier, Regulation of contraction in striated muscle, Physiol. Rev. 80 (2000) 853–924.

[56] P. Vibert, R. Craig, W. Lehman, Steric-model for activation of muscle thin filaments, J Mol Biol 266 (1) (1997) 814.

[57] P. P. de Tombe, R. D. Mateja, K. Tachampa, A. Mou, F. Y., G. P., T. C. Irving, Myofilament length dependent activation, J. Mol. Cell Cardiol 48 (2010) 851 858. doi:10.1016/j.yjmcc.200912.017.

[58] E. Pate, R. Cooke, A model of crossbridge action: The effects of atp, adp, and pi, J Muscle Res Cell Motil 10 (1989) 181196.

[59] R. Cooke, Actomyosin interaction in striated muscle, Physiol Rev 77 (1997) 671697.

[60] B. Tanner, T. Daniel, M. Regnier, Filament compliance influences cooperative activation of thin filaments and the dynamics of force production in skeletal muscle, PLoS Comput Biol 8 (5) (2012) e1002506.

[61] D. M. Bers, Excitationcontraction coupling and cardiac contractile force edn 2, Kluwer Academic, Dordrecht, Netherlands.

[62] D. M. Bers, Cardiac excitation-contraction coupling, Nature 415 (2001) 198205.

[63] L. Li, G. Chu, E. G. Kranias, D. M. Bers, Cardiac myocyte calcium transport in phospholamban knockout mouse: relaxation and endogenous camkii effects, Am. J. Physiol 274 (1998) H1335H1347.

[64] T. W. Traut, Physiological concentrations of purines and pyrimidines, Molecular and cellular biochemistry 140 (1) (1994) 1–22.

[65] P. Reichard, A. Ehrenberg, Ribonucleotide reductase–a radical enzyme, Science (1983) 514–519.

[66] M. Regnier, A. Rivera, P. Chase, 2-deoxy-atp enhances contractility of rat cardiac muscle, Circ Res 86 (2000) 1211–1217.

[67] M. Regnier, H. H Martin, R. Barsotti, A. Rivera, D. Martyn, E. Clemmens, Cross-bridge versus thin filament contributions to the level and rate of force development in cardiac muscle, Biophys J 87 (3) (2004) 1815–1824.

[68] A. J. Baker, Refueling the heart: using 2-deoxy-atp to enhance cardiac contractility, Journal of molecular and cellular cardiology 51 (6) (2011) 883–884.

[69] B. Schoffstall, A. Clark, P. Chase, Positive inotropic effects of low datp/atp ratios on mechanics and kinetics of porcine cardiac muscle, Biophys J 91 (6) (2006) 2216–2226.

[70] B. Schoffstall, P. B. Chase, Increased intracellular [datp] enhances cardiac contraction in embryonic chick cardiomyocytes, Journal of cellular biochemistry 104 (6) (2008) 2217–2227.

[71] F. Moussavi-Harami, M. V. Razumova, A. W. Racca, Y. Cheng, A. Stempien-Otero, M. Regnier, 2-deoxy adenosine triphosphate improves contraction in human end-stage heart failure, Journal of molecular and cellular cardiology 79 (2015) 256–263.

[72] Y. Cheng, K. A. Hogarth, M. L. O'Sullivan, M. Regnier, W. G. Pyle, 2-deoxy-adenosine triphosphate restores the contractile function of cardiac myofibril from adult dogs with naturally occurring dilated cardiomyopathy, American Journal of Physiology-Heart and Circulatory Physiology.

[73] F. Korte, J. Dai, K. Buckley, E. Feest, N. Adamek, M. Geeves, C. Murry, M. Regnier, Upregulation of cardiomyocyte ribonucleotide reductase increases intracellular 2 deoxy-atp, contractility, and relaxation, J Mol Cell Cardiol 51 (6) (2011) 894–901.

[74] S. Nowakowski, S. Kolwicz, F. Korte, Z. Luo, J. Robinson-Hamm, J. Page, M. Regnier, Transgenic overexpression of ribonucleotide reductase improves cardiac performance, Proceedings of the National Academy of Sciences 110 (15) (2013) 6187–6192.

[75] S. D. Lundy, S. A. Murphy, S. K. Dupras, J. Dai, C. E. Murry, M. A. Laflamme, M. Regnier, Cell-based delivery of datp via gap junctions enhances cardiac contractility, Journal of molecular and cellular cardiology 72 (2014) 350–359.

[76] K. Thomson, G. Odom, C. Murry, G. M. GG, F. Moussavi-Harami, S. Teichman, X. Chen, S. Hauschka, J. Chamberlain, M. Regnier, Translation of cardiac myosin activation with 2-deoxy-atp to treat heart failure via an experimental ribonucleotide reductase-based gene therapy, Biophys J 1 (7) (2016) 666–679.

[77] S. C. Kolwicz Jr, G. L. Odom, S. G. Nowakowski, F. Moussavi-Harami, X. Chen, H. Reinecke, S. D. Hauschka, C. E. Murry, G. G. Mahairas, M. Regnier, Aav6-mediated cardiac-specific overexpression of ribonucleotide reductase enhances myocardial contractility, Molecular Therapy 24 (2) (2016) 240–250.

[78] S. Kadota, J. Carey, H. Reinecke, J. Leggett, S. Teichman, M. A. Laflamme, C. E. Murry, M. Regnier, G. G. Mahairas, Ribonucleotide reductase-mediated increase in datp improves cardiac performance via myosin activation in a large animal model of heart failure, European journal of heart failure 17 (8) (2015) 772–781.

[79] S. Nowakowski, M. Regnier, V. Daggett, Molecular mechanisms underlying deoxy-adp. pi activation of pre-powerstroke myosin, Protein Sci 26 (4) (2017) 749–762.

[80] O. K. Baryshnikova, I. M. Robertson, P. Mercier, B. D. Sykes, The dilated cardiomyopathy g159d mutation in cardiac troponin c weakens the anchoring interaction with troponin i, Biochemistry 47 (2008) 10950–10960. doi:10.1021/bi801165c.

[81] W. J. Dong, J. Xing, Y. Ouyang, J. An, H. C. Cheung, Structural kinetics of cardiac troponin c mutants linked to familial hypertrophic and dilated cardiomyopathy in troponin complexes, J. Biol Chem 283 (2008) 34243432. doi:10.1074/jbc.M703822200.

[82] R. Hershberger, N. Norton, A. Morales, D. Li, J. Siegfried, J. Gonzalez-Quintana, Coding sequence rare variants identified in mybpc3, myh6, tpm1, tnnc1, and tnni3 from 312 patients with familial or idiopathic dilated cardiomyopathy, Circ. Cardiovasc. Genet 3 (2010) 155161. doi:10.1161/CIRCGENETICS.109.912345.

[83] E. Rampersaud, J. D. Siegfried, N. Norton, D. Li, E. Martin, R. E. Hershberger, Rare variant mutations identified in pediatric patients with dilated cardiomyopathy, Prog. Pediatr. Cardiol. 31 (2011) 3947. doi:10.1016/j.ppedcard.2010.11.008.

[84] J. R. Pinto, J. D. Siegfried, M. S. Parvatiyar, D. Li, N. Norton, M. A. Jones, et al., Functional characterization of tnnc1 rare variants identified in dilated cardiomyopathy, J. Biol. Chem 286 (2011) 3440434412. doi:10.1074/jbc.M111.267211.

[85] A. P. Landstrom, M. S. Parvatiyar, J. R. Pinto, M. L. Marquardt, J. M. T. Bos, D. J., et al., Molecular and functional characterization of novel hypertrophic cardiomyopathy susceptibility mutations in tnnc1- encoded troponin c, J. Mol. Cell. Cardiol 45 (2008) 281288. doi:10.1016/j.yjmcc.2008.05.003.

[86] K. Y. van Spaendonck-Zwarts, J. P. van Tintelen, D. J. van Veldhuisen, R. van der Werf, J. D. Jongbloed, W. J. Paulus, et al., Peripartum cardiomyopathy as a part of familial dilated cardiomyopathy, Circulation 121 (2010) 21692175. doi:10.1161/CIRCULATIONAHA.109.929646.

[87] S. Carballo, P. Robinson, R. Otway, D. Fatkin, J. D. H. Jongbloed, N. de Jonge, et al., Identification and functional characterization of cardiac troponin i as a novel disease gene in autosomal dominant dilated cardiomyopathy, Circ. Res 105 (2009) 375382. doi:10.1161/CIRCRESAHA.109196055.

[88] C. Murakami, S. Nakamura, M. Kobayashi, K. Maeda, W. Irie, B. Wada, et al., Analysis of the sarcomere protein gene mutation on cardiomyopathy - mutations in the cardiac troponin i gene, Leg. Med. (Tokyo) 12 (2010) 280283. doi:10.1016/j.legalmed.2010.07.002.

[89] G. Venkatraman, K. Harada, A. V. Gomes, W. G. L. Kerrick, J. D. Potter, Different functional properties of troponin t mutants that cause dilated cardiomyopathy, J. Biol. Chem 278 (2003) 4167041676. doi:10.1074/jbc.M302148200.

[90] R. E. Hershberger, J. R. Pinto, S. B. Parks, J. D. Kushner, D. Li, S. Ludwigsen, et al., Clinical and functional characterization of tnnt2 mutations identified in patients with dilated cardiomyopathy, Circ. Cardiovasc. Genet. 2 (2009) 306 313. doi:10.1161/CIRCGENETICS.108.846733.

[91] A. N. Chang, N. J. Greenfield, A. Singh, J. D. Potter, J. R. Pinto, Structural and protein interaction effects of hypertrophic and dilated cardiomyopathic mutations in alpha-tropomyosin, Front. Physiol. 5 (2014) 460. doi:10.3389/fphys.2014.00460.

[92] M. X. Li, P. M. Hwang, Structure and function of cardiac troponin c (tnnc1): implications for heart failure, cardiomyopathies, and troponin modulating drugs, Gene 571 (2015) 153166. doi:10.1016/j.gene.2015.07.074.

[93] P. M. Kekenes-Huskey, S. Lindert, J. A. McCammon, Molecular basis of calcium-sensitizing and desensitizing mutations of the human cardiac troponin c regulatory domain: a multi-scale simulation study, PLoS Comp Biol 8 (2012) e1002777. doi:10.1371/journal.pcbi.1002777.

[94] S. Lindert, P. Kekenes-Huskey, J. McCammon, Long-timescale molecular dynamics simulations elucidate the dynamics and kinetics of exposure of the hydrophobic patch in troponin c, Biophys. J 103 (2012) 17841789.

[95] B. R. Ertz-Berger, H. He, C. Dowell, S. M. Factor, T. E. Haim, S. Nunez, et al., Changes in the chemical and dynamic properties of cardiac troponin t cause discrete cardiomyopathies in transgenic mice, Proc. Natl. Acad. Sci. U.S.A 102 (2005) 1821918224. doi:10.1073/pnas.0509181102.

[96] X. E. Li, K. Holmes, W. Lehman, H. Jung, S. Fischer, The shape and flexibility of tropomyosin coiled coils: Implications for actin filament assembly and regulation, J Mol Biol 395 (2010) 327–339.

[97] X. E. Li, W. Lehman, S. Fischer, The relationship between curvature, flexibility and persistence length in the tropomyosin coiled-coil, J. Struct. Biol 170 (2010) 313318. doi:10.1016/j.jsb.2010.01.016.

[98] C. K. P. Loong, M. A. Badar, P. B. Chase, Tropomyosin flexural rigidity and single ca2+ regulatory unit dynamics: implications for cooperative regulation of cardiac muscle contraction and cardiomyocyte hypertrophy, Front Physiol 3 (2012) 80.

[99] J. von der Ecken, M. Mü, W. Lehman, D. J. Manstein, P. A. Penczek, S. Raunser, Structure of f-actin-tropomyosin complex, Nature 519 (2015) 114–7.

[100] X. Li, W. Suphamungmee, M. Janco, M. Geeves, S. Marston, S. F. et al, The flexibility of two tropomyosin mutants, d175n and e180g, that cause hypertrophic cardiomyopathy, Biochem. Biophys. Res. Commun 424 (2012) 493496.

[101] W. Zheng, S. Hitchcock-DeGregori, B. Barua, Investigating the effects of tropomyosin mutations on its flexibility and interactions with filamentous actin using molecular dynamics simulation, J. Muscle Res. Cell Motil 37 (2016) 131147.

[102] . Davis, S. Tikunova, Ca2+ exchange with troponin c and cardiac muscle dynamics., Cardiovasc. Res 77 (2008) 619626.

[103] J. F. Varughese, J. M. Chalovich, Y. Li, Molecular dynamics studies on troponin (tni-tnt-tnc) complexes: insight into the regulation of muscle contraction, J. Biomol. Struct. Dyn. 28 (2010) 159174. doi:10.1080/07391102.2010.10507350.

[104] J. Jayasundar, J. Xing, J. Robinson, H. Cheung, W. Dong, Molecular dynamics simulations of the cardiac troponin complex performed with fret distances as restraints, PLoS ONE 9 (2014) e87135.

[105] E. Manning, J. Tardiff, S. Schwartz, A model of calcium activation of the cardiac thin filament, Biochemistry 50 (2011) 74057413.

[106] E. P. Manning, P. J. Guinto, J. C. Tardiff, Correlation of molecular and functional effects of mutations in cardiac troponin t linked to familial hypertrophic cardiomyopathy: an integrative in silico/in vitro approach, J. Biol. Chem 287 (2012) 1451514523. doi:10.1074/jbc.M111.257436.

[107] R. C. P. Kerckhoffs, J. H. Omens, A. D. McCulloch, L. J. Mulligan, Ventricular dilation and electrical dyssynchrony synergistically increase regional mechanical nonuniformity but not mechanical dyssynchrony: a computational model, Circ. Heart Fail 3 (2010) 528536. doi:10.1161/circheartfailure.109.862144.

[108] D. S. Herman, L. Lam, M. R. G. Taylor, L. Wang, P. Teekakirikul, D. Christodoulou, et al., Truncations of titin causing dilated cardiomyopathy, N. Engl. J. Med 366 (2012) 619628. doi:10.1056/NEJMoa1110186.

[109] H. Lu, B. Isralewitz, A. Krammer, V. Vogel, K. Schulten, Unfolding of titin immunoglobulin domains by steered molecular dynamics simulation, Biophys. J. 75 (1998) 662671. doi:10.1016/s0006-3495(98)77556-3.

[110] H. Lu, A. Krammer, B. Isralewitz, V. Vogel, K. Schulten, Computer modeling of force-induced titin domain unfolding, Adv. Exp. Med. Biol. 481 (2000) 143–162. doi:10.1007/978-1-4615-4267-4_9.

[111] M. Gao, H. Lu, K. Schulten, Unfolding of titin domains studied by molecular dynamics simulations, J. Muscle Res. Cell Motil 23 (2002) 513 521. doi:10.1023/A:1023466608163.

[112] D. Thirumal Kumar, C. George Priya Doss, P. Sneha, I. A. Tayubi, R. Siva, C. Chakraborty, et al., Influence of v54m mutation in giant muscle protein titin: a computational screening and molecular dynamics approach, J. Biomol. Struct. Dyn 35 (5) (2017) 917–928. doi:10.1080/07391102.2016.1166456.

[113] D. Noble, Modeling the heartfrom genes to cells to the whole organ, Science 295 (2002) 16781682. doi:10.1126/science.1069881.

[114] J. J. Rice, G. Stolovitzky, Y. Tu, P. P. de Tombe, Ising model of cardiac thin filament activation with nearest-neighbor cooperative interactions, Biophys. J. 84 (2003) 897909. doi:10.1016/S0006-3495(03)74907-8.

[115] J. L. Puglisi, F. Wang, D. M. Bers, Modeling the isolated cardiac myocyte, Prog. Biophys. Mol. Biol 85 (2004) 163178. doi:10.1016/j.pbiomolbio.2003.12.003.

[116] Y. Aboelkassem, J. Bonilla, K. McCabe, S. Campbell, Contributions of ca2+-independent thin filament activation to cardiac muscle function, Biophys J 109 (2015) 2101 2112.

[117] L. R. Sewanan, J. R. Moore, W. J. Lehman, S. G. Campbell, Predicting effects of tropomyosin mutations on cardiac muscle contraction through myofilament modeling, Front. Physiol. 7 (2016) 473.

[118] V. L. M. Rundell, V. Manaves, A. F. Martin, P. P. de Tombe, Impact of beta-myosin heavy chain isoform expression on cross-bridge cycling kinetics, Am. J. Physiol. Heart Circ. Physiol 288 (2005) H896H903. doi:10.1152/ajpheart.00407.2004.

[119] J. van der Velden, A. F. Moorman, G. J. Stienen, Age- dependent changes in myosin composition correlate with enhanced economy of contraction in guinea-pig hearts, J. Physiol. 507(Pt 2) (1998) 497510. doi:10.1111/j.1469-7793.1998.497bt.x.

[120] K. Nakao, W. Minobe, R. Roden, M. R. Bristow, L. A. Leinwand, Myosin heavy chain gene expression in human heart failure, J. Clin. Invest 100 (1997) 23622370. doi:10.1172/JCI119776.

[121] P. P. de Tombe, R. J. Solaro, Integration of cardiac myofilament activity and regulation with pathways signaling hypertrophy and failure, Ann. Biomed. Eng 28 (2000) 9911001. doi:10.1114/11312189.

[122] S. M. Harrison, D. M. Bers, Influence of temperature on the calcium sensitivity of the myofilaments of skinned ventricular muscle from the rabbit, J. Gen. Physiol 93 (1989) 411 428. doi:10.1085/jgp.93.3.411.

[123] S. M. Harrison, D. M. Bers, Temperature dependence of myofilament ca2+ sensitivity of rat, guinea pig, and frog ventricular muscle, Am. J. Physiol. 258 (1990) C274C281.

[124] P. P. de Tombe, G. J. M. Stienen, Impact of temperature on cross-bridge cycling kinetics in rat myocardium, J. Physiol. 584 (2007) 591600. doi:10.1113/jphysiol.2007.138693.

[125] H. E. ter Keurs, J. J. Bucx, P. P. de Tombe, P. Backx, T. Iwazumi, The effects of sarcomere length and ca++ on force and velocity of shortening in cardiac muscle, Adv. Exp. Med. Biol. 226 (1988) 581593.

[126] D. P. Dobesh, J. P. Konhilas, P. P. de Tombe, Cooperative activation in cardiac muscle: impact of sarcomere length, Am. J. Physiol. Heart Circ. Physiol. 282 (2002) H1055H1062. doi:10.1152/ajpheart.00667.2001.

[127] K. Edman, The velocity of unloaded shortening and its relation to sarcomere length and isometric force in vertebrate muscle fibres, J. Physiol. 291 (1979) 143159. doi:10.1113/jphysiol.1979.sp012804.

[128] P. J. Hunter, A. D. McCulloch, H. E. ter Keurs, Modelling the mechanical properties of cardiac muscle, Prog. Biophys. Mol. Biol 69 (1998) 289331. doi:10.1016/S0079-6107(98)00013-3.

[129] K. S. McDonald, M. R. Wolff, R. L. Moss, Force-velocity and power-load curves in rat skinned cardiac myocytes, J. Physiol 511 (1998) 519531. doi:10.1111/j.1469-7793.1998.519bh.x.

[130] T. J. Herron, F. S. Korte, K. S. McDonald, Loaded shortening and power output in cardiac myocytes are dependent on myosin heavy chain isoform expression., AM. J. Physiol. Heart Circ. Physiol. 281 (2001) H1217H1222.

[131] P. M. L. Janssen, L. B. Stull, E. Mrban, Myofilament properties comprise the rate-limiting step for cardiac relaxation at body temperature in the rat., Am. J Physiol. Heart Circ. Physiol. 282 (2002) H499H507. doi:10.1152/ajpheart.00595.2001.

[132] J. P. Konhilas, T. C. Irving, P. P. de Tombe, Frank-starling law of the heart and the cellular mechanisms of length-dependent activation, Pflugers Arch 445 (2002) 305310. doi:10.1007/s00424-002-0902-1.

[133] R. L. Moss, S. H. Buck, regulation of cardiac contraction by calcium, in supplement 6: Handbook of physiology, the cardiovascular system, the heart (wiley-blackwell) (2011) 420454doi:10.1002/cphy.cp020111.

[134] J. Lumens, T. Delhaas, B. Kirn, T. Arts, Three-wall segment (triseg) model describing mechanics and hemodynamics of ventricular interaction, Ann. Biomed. Eng 37 (2009) 22342255. doi:10.1007/s10439-009-9774-2.

[135] J. M. Winters, L. Stark, Muscle models: what is gained and what is lost by varying model complexity, Biol. Cybern. 55 (1987) 403420. doi:10.1007/BF00318375.

[136] V. Gurev, J. Constantino, J. J. Rice, N. A. Trayanova, Distribution of electromechanical delay in the heart: insights from a three-dimensional electromechanical model, Biophys. J. 99 (2010) 745754. doi:10.1016/j.bpj.2010.05.028.

[137] K. Tran, N. P. Smith, D. S. Loiselle, E. J. Crampin, A metabolite- sensitive, thermodynamically constrained model of cardiac cross-bridge cycling: implications for force development during ischemia, Biophys. J. 98 (2010) 267276. doi:10.1016/j.bpj.2009.10.011.

[138] S. Sugiura, T. Washio, A. Hatano, J. Okada, H. Watanabe, T. Hisada, Multi-scale simulations of cardiac electrophysiology and mechanics using the university of tokyo heart simulator, Prog. Biophys. Mol. Biol 110 (2012) 380389. doi:10.1016/j.pbiomolbio.2012.07.001.

[139] T. Washio, J.-i. Okada, S. Sugiura, T. Hisada, Approximation for cooperative interactions of a spatially-detailed cardiac sarcomere model, Cell Mol. Bioeng 5 (2012) 113126. doi:10.1007/s12195-011-0219-2.

[140] P. B. Chase, J. Macpherson, T. Daniel, A spatially explicit nanomechanical model of the half-sarcomere: myofilament compliance affects ca 2+-activation, Annals of biomedical engineering 32(11) (2004) 1559–1568.

[141] A. Kataoka, C. Hemmer, P. B. Chase, Computational simulation of hypertrophic cardiomyopathy mutations in troponin i: influence of increased myofilament calcium sensitivity on isometric force, atpase and [ca2+]i, J. Biomech. 40 (2007) 20442052. doi:10.1016/j.jbiomech.2006.09.026.

[142] L. B. Stull, M. K. Leppo, E. Marban, P. M. L. Janssen, Physiological determinants of contractile force generation and calcium handling in mouse myocardium, J. Mol. Cell Cardiol 34 (2002) 13671376. doi:10.1006/jmcc.20.02.2065.

[143] S. Nishimura, S.-i. Yasuda, M. Katoh, K. P. Yamada, H. Yamashita, Y. Saeki, et al., Single cell mechanics of rat cardiomyocytes under isometric, unloaded, and physiologically loaded conditions, Am. J. Physiol. Heart Circ. Physiol. 287 (2004) H196H202. doi:10.1152/ajpheart.00948.2003.

[144] W. A. Clark, Jr., R. A. Chizzonite, A. W. Everett, M. Rabinowitz, R. Zak, Species correlations between cardiac isomyosins. a comparison of electrophoretic and immunological properties., J. Biol. Chem 257 (1982) 54495454.

[145] A. C. Zeigler, W. J. Richardson, J. W. Holmes, J. J. Saucerman, A computational model of cardiac fibroblast signaling predicts context- dependent drivers of myofibroblast differentiation, J. Mol. Cell. Cardiol 94 (2016) 7281. doi:10.1016/j.yjmcc.2016.03.008.

[146] K. A. Ryall, D. O. Holland, K. A. Delaney, M. J. Kraeutler, A. J. Parker, J. J. Saucerman, Network reconstruction and systems analysis of cardiac myocyte hypertrophy signaling, J. Biol. Chem 287 (2012) 4225942268. doi:10.1074/jbc.M112.382937.

[147] U. Kuzmanov, H. Guo, D. Buchsbaum, J. Cosme, C. Abbasi, R. Isserlin, et al., Global phosphoproteomic profiling reveals perturbed signaling in a mouse model of dilated cardiomyopathy, Proc. Natl. Acad. Sci. U.S.A 113 1259212597. doi:10.1073/pnas.16064.44113.

[148] E. C. Dyer, A. M. Jacques, A. C. Hoskins, D. G. Ward, C. E. Gallon, A. E. Messer, J. P. Kaski, M. Burch, J. C. Kentish, M. Sb., Functional analysis of a unique troponin c mutation, gly159asp, that causes familial dilated cardiomyopathy, studied in explanted heart muscle, Circulation. Heart failure 2 (2009) 456–464.

[149] C. S. Farah, R. Fc., The troponin complex and regulation of muscle contraction, Faseb J 9 (1995) 755–767.

[150] M. X. Li, X. Wang, S. Bd., Structural based insights into the role of troponin in cardiac muscle pathophysiology, Journal of Muscle Research and Cell Motility 25 (2004) 559–579.

[151] T. Kobayashi, R. Solaro, Calcium, thin filaments, and the integrative biology of cardiac contractility, Annu Rev Physiol 67 (2005) 39–67.

[152] L. Spyracopoulos, M. X. Li, S. K. Sia, S. M. Gagne, M. Chandra, R. J. Solaro, S. Bd., Calcium-induced structural transition in the regulatory domain of human cardiac troponin c, Biochemistry 36 (1997) 12138–12146.

[153] M. X. Li, L. Spyracopoulos, S. Bd., Binding of cardiac troponin-1147-163 induces a structural opening in human cardiac troponin-c, Biochemistry 38 (1999) 8289–8298.

[154] I. M. Robertson, Y. B. Sun, M. X. Li, S. B. A. structural and, and functional perspective into the mechanism of ca(2+)-sensitizers that target the cardiac troponin complex. j, Mol. Cell. Cardiol 49 (2010) 1031–1041.

[155] S. M. Gagne, M. X. Li, R. T. McKay, S. Bd., The nmr angle on troponin c, Biochem Cell Biol 76 (1998) 302–312.

[156] S. Takeda, A. Yamashita, K. Maeda, Y. Maeda, Structure of the core domain of human cardiac troponin in the ca2+-saturated form, Nature 424 (2003) 35–41.

[157] X. Wang, P. Mercier, P. J. Letoumeau, S. Bd., Effects of phe-to-trp mutation and fluorotryptophan incorporation on the solution structure of cardiac troponin c, and analysis of its suitability as a potential probe for in situ nmr studies, Protein Sci 14 (2005) 2447–2460.

[158] J. Varguhese, T. Baxley, J. Chalovich, Y. Li, A computational and experimental approach to investigate bepridil binding with cardiac troponin, J. Phys. Chem. B 115 (2011) 23922400.

[159] D. Wang, I. M. Robertson, M. X. Li, M. E. McCully, M. L. Crane, Z. Luo, A. Y. Tu, V. Daggett, B. D. Sykes, R. M., Structural and functional consequences of the cardiac troponin c l48qca(2+)- sensitizing mutation, Biochemistry 51 (2012) 4473–4487.

[160] X. Wang, M. X. Li, S. BD, Structure of the regulatory n-domain of human cardiac troponin c in complex with human cardiac troponin 1147-163 and bepridil, J Biol Chem 277 (2002) 31124–31133.

[161] M. Christen, P. H. Hunenberger, D. Bakowies, R. Baron, R. Burgi, D. P. Geerke, T. N. Heinz, M. A. Kastenholz, V. Krautler, C. Oostenbrink, et al., The gromos software for biomolecular simulation: Gromos05, Journal of computational chemistry 26 (2005) 1719–1751.

[162] G. A. Huber, J. A. McCammon, Browndye: a software package for brownian dynamics, Computer Physics Communications 181 (2010) 1896–1905.

[163] T. D. abd P Czodrowski, H. Li, J. Nielsen, J. Jensen, G. Klebe, N. Baker, Pdb2pqr: expanding and upgrading automated preparation of biomolecular structures for molecular simulations, Nucleic Acids Res 35 (2007) W522–5.

[164] N. Baker, D. Sept, S. Joseph, M. Holst, J. McCammon, Electrostatics of nanosystems: application to microtubules and the ribosome, Natl. Acad. Sci. USA 98 (2001) 10037–10041.

[165] A. L. Hazard, S. C. Kohout, N. L. Stricker, J. A. Putkey, F. Jj., The kinetic cycle of cardiac troponin c: calcium binding and dissociation at site ii trigger slow conformational rearrangements, Protein Sci 7 (1998) 2451–2459.

[166] S. C. Little, B. J. Biesiadecki, A. Kilic, R. S. Higgins, P. M. Janssen, D. Jp., The rates of ca2+ dissociation and cross-bridge detachment from ventricular myofibrils as reported by a fluorescent cardiac troponin c, J. Biol. Chem 287 (2012) 2793027940.

[167] L. S. Tobacman, Thin filament-mediated regulation of cardiac contraction, Annu. Rev. Physiol. 58 (1996) 447–481.

[168] T. Kobayashi, L. Jin, de Tombe Pp., Cardiac thin filament regulation, Pflug. Arch. Eur. J. Phy 457 (2008) 3746.

[169] N. M. Cordina, C. K. Liew, P. R. Potluri, P. M. Curmi, P. G. Fajer, T. M. Logan, J. P. Mackay, B. L.J., Ca2+- induced pre-nmr changes in the troponin complex reveal the possessive nature of the cardiac isoform for its regulatory switch, PLoS One 9 (2014) ell2976.

[170] A. Crivici, I. M., Molecular and structural basis of target recognition by calmodulin, Annual review of biophysics and biomolecular structure 24 (1995) 85116.

[171] S. B. Tikunova, J. Davis, Designing calcium-sensitizing mutations in the regulatory domain of cardiac troponin c, J. Biol. Chem 279 (2004) 3534135352.

[172] W. Dong, S. S. Rosenfeld, C. K. Wang, A. M. Gordon, H. Cheung, Kinetic studies of calcium binding to the regulatory site of troponin c from cardiac muscle, J. Biol. Chem 271 (1996) 688694.

[173] Y. Ogawa, Calcium binding to troponin c and troponin: Effects of mg2+, ionic strength and ph, J. Biochem 97 (1985) 10111023.

[174] D. E. Shaw, M. M. Deneroff, R. O. Dror, J. S. Kuskin, R. H. Larson, J. K. Salmon, C. Young, B. Batson, K. J. Bowers, J. C. Chao, et al., Anton, a special-purpose machine for molecular dynamics simulation, Commun. Acm 51 (2008) 9197.

[175] S. K. Sia, M. X. Li, L. Spyracopoulos, S. M. Gagne, W. Liu, J. A. Putkey, B. Sykes, Structure of cardiac muscle troponin c unexpectedly reveals a closed regulatory domain, J. Biol. Chem 272 (1997) 1821618221.

[176] W. J. Dong, J. Xing, M. Villain, M. Hellinger, J. M. Robinson, M. Chandra, R. J. Solaro, P. K. Umeda, H. Cheung, Conformation of the regulatory domain of cardiac muscle troponin c in its complex with cardiac troponin i, J. Biol. Chem 274 (1999) 3138231390.

[177] S. K. Gollapudi, M. Chandra, Cardiomyopathy-related mutations in cardiac troponin c, l29q and g159d, have divergent effects on rat cardiac myofiber contractile dynamics, Biochemistry research international 2012 (824068).

[178] G. N. Phillips., J. P. Fillers, C. Cohen, Motions of tropomyosin. crystal as metaphor, Biophys J 32 (1980) 485–502.

[179] J. J. Earley, Simple harmonic motion of tropomyosin: proposed mechanism for length-dependent regulation of muscle active tension, Am J Physiol. 261 (1991) C1184–95.

[180] D. F. McKillop, M. A. Geeves, Regulation of the interaction between actin and myosin subfragment 1: Evidence for three states of the thin filament, Biophys. J. 65 (1993) 693–701.

[181] S. E. Hitchcock-DeGregori, Tropomyosin: function follows structure, Adv Exp Med Biol. 644 (2008) 60–72.

[182] P. Gunning, G. O'neill, E. Hardeman, Tropomyosin-based regulation of the actin cytoskeleton in time and space, Physiol Rev. 88 (2008) 1–35.

[183] C. Wang, L. M. Coluccio, New insights into the regulation of the actin cytoskeleton by tropomyosin, Int Rev Cell Mol Biol 281 (2010) 91 – 128.

[184] W. Zheng, B. Barua, S. E. Hitchcock-DeGregori, Probing the flexibility of tropomyosin and its binding to filamentous actin using molecular dynamics simulations, Biophys. J. 105 (2013) 1882–1892.

[185] M. El-Mezgueldi, Tropomyosin dynamics, J Muscle Res Cell Motil 35 (2014) 203–210.

[186] Y. Aboelkassem, N. Trayanova, Tropomyosin dynamics during cardiac thin filament activation as governed by a multi-well energy landscape, Biophys J 110 (2016) 524a.

[187] C. Risi, J. Eisner, B. Belknap, D. H. Heeley, H. D. White, G. F. Schrder, V. E. Galkin, Ca2+ -induced movement of tropomyosin on native cardiac thin filaments revealed by cryoelectron microscopy, PNAS 114 (2017) 6782–6787.

[188] Y. Aboelkassem, N. Trayanova, Tropomyosin fluctuations over a multi-well energy landscape: A brownian ratchet model of cardiac muscle contraction, Biophys J 112 (2017) 259a–260a.

[189] Y. Aboelkassem, K. J. McCabe, G. Huber, J. Sundnes, A. D. McCulloch, Turning the azimuthal motions of adjacent tropomyosins into a coupled n-body problem in a brownian model of cardiac thin filament activation, Biophys J 114 (2018) 502a–503a.

[190] Y. Aboelkassem, N. Trayanova, Tropomyosin dynamics during cardiac muscle contraction as governed by a multi-well energy landscape, Prog Biophys Mol Biol xx (2018) yy–zz.

[191] S. Mijailovich, O. Kayser-Herold, X. Li, H. Griffiths, M. Geeves, Cooperative regulation of myosin-s1 binding to actin filaments by a continuous flexible tm-tn chain, Eur Biophys J 41 (2012) 1015–1032.

[192] E. Behrmann, M. Muller, P. Penczek, H. Mannherz, D. Manstein, S. Raunser, Structure of the rigor actin-tropomyosin-myosin complex, Cell 150 (2) (2012) 327–338.

[193] C. Bacchiocchi, S. S. Lehrer, Ca^{2+}-induced movement of tropomyosin in skeletal muscle thin filaments observed by multi-site fret, Biophys. J. 82 (2002) 1524–1536.

[194] M. F. L. Holthauzen, F. Correa, C. S. Farah, Ca^{2+}-induced rolling of tropomyosin in muscle thin filaments: the alpha- and beta-band hypothesis revisited., J Biol Chem 279 (2004) 15204–15213.

[195] D. Smith, R. Maytum, M. Geeves, Cooperative regulation of myosin-actin interactions by a continuous flexible chain i: Actin-tropomyosin systems, Biophys. J. 84 (2003) 3155–3167.

[196] D. Smith, M. Geeves, Cooperative regulation of myosin-actin interactions by a continuous flexible chain ii: Actin-tropomyosin-troponin and regulation by calcium, Biophys. J. 84 (2003) 3168–3180.

[197] M. A. Geeves, H. Griffiths, S. Mijailovich, D. A. Smith, Cooperative $[ca^{2+}]$-dependent regulation of the rate of myosin binding to actin: solution data and the tropomyosin chain model, Biophys. J. 100 (2011) 2679–2687.

[198] N. A. Metalnikova, A. K. Tsaturyan, A mechanistic model of ca regulation of thin filament in cardiac muscle, Biophys. J. 105 (2013) 941–950.

[199] D. Smith, Path-integral theory of an axially confined work-like chain, J. Phys. Math. Gen. 34 (2001) 4507–4523.

[200] W. Humphrey, A. Dalke, K. Schulten, Vmd - visual molecular dynamics, J Molec Graphics 14 (1) (1996) 33–38.

[201] T. Dolinsky, J. Nielsen, J. A. McCammon, N. Baker, Pdb2pqr: an automated pipeline for the setup, excution, and analysis of poisson-boltzmann electrostatics calculations, Nucleic Acids Research 32 (2004) W665–W667.

[202] D. Case, I. B.-S. ..., D. York, P. Kollman, Amber 2018, University of California, San Francisco.

[203] N. Baker, D. Sept, S. Joseph, M. Hoist, J. McCammon, Electrostatics of nanosystems: Application to microtubules and the ribosome, Proc. Natl. Acad. Sci 98 (18) (2001) 10037–10041.

[204] M. Orzechowski, J. R. Moore, S. Fischer, W. Lehman, Tropomyosin movement on f-actin during muscle activation explained by energy landscapes, Archives of Biochemistry and Biophysics 545 (2014) 63–68.

[205] P. Kekenes-Huskey, S. Lindert, J. McCammon, Molecular basis of calcium-sensitizing and desensitizing mutations of the human cardiac troponin c regulatory domain: A multi-scale simulation study, PLoS Comp Biol 8 (2012) e1002777.

[206] B. Ertz-Berger, H. He, C. Dowell, S. Factor, T. Haim, S. Nunez, S. Schwartz, J. Ingwall, J. Tardiff, Changes in the chemical and dynamic properties of cardiac troponin t cause discrete cardiomyopathies in transgenic mice, PNAS 102 (2005) 1821918224.

[207] C. Loong, M. Badr, P. Chase, Tropomyosin flexural rigidity and single ca2+ regulatory unit dynamics: implications for cooperative regulation of cardiac muscle contraction and cardiomyocyte hypertrophy, Front. Physiol 3:80 (2012) 110.

[208] W. Lehman, G. Medlock, X. Li, W. Suphamungmee, A. Tu, A. S. et al, Phosphorylation of ser283 enhances the stiffness of the tropomyosin head-to-tail overlap domain, Arch. Biochem. Biophys 571 (2015) 1015.

[209] T. Frembgen-Kesner, C. T. Andrews, S. Li, N. A. Ngo, S. A. Shubert, A. Jain, O. J. Olayiwola, M. R. Weishaar, A. H. Elcock, Parametrization of backbone flexibility in a coarse-grained force field for proteins (coffdrop) derived from all-atom explicit-solvent molecular dynamics simulations of all possible two-residue peptides, J. Chem. Theo. Comp. 11 (2015) 2341–2354.

[210] M. J. Rynkiewicz, T. Prum, S. Hollenberg, F. A. Kiani, P. M. Fagnant, S. B. Marston, K. M. Trybus, S. Fischer, J. R. Moore, W. Lehman, Tropomyosin must interact weakly with actin to effectively regulate thin filament function, Biophys. J. 113 (2017) 2444–2451.

[211] B. A. Luty, S. E. Amrani, J. A. McCammon, Simulation of the bimolecular reaction between superoxide and superoxide dismutase: Synthesis of the encounter and reaction steps, J.Am.Chem.Soc. 115 (1993) 11874–11877.

[212] L. W. Votapka, B. R.Jagger, A. L. Heyneman, R. E. Amaro, Seekr: Simulation enabled estimation of kinetic rates, a computational tool to estimate molecular kinetics and its application to trypsin-benzamidine binding, J. Phys. Chem. B 121 (2017) 3597–3606.

[213] M. Regnier, D. Martyn, P. Chase, Calcium regulation of tension redevelopment kinetics with 2-deoxy-atp or low [atp] in rabbit skeletal muscle, Biophysical journal 74 (4) (1998) 2005–2015.

[214] M. Regnier, E. Homsher, The effect of atp analogs on posthydrolytic and force development steps in skinned skeletal muscle fibers, Biophysical journal 74 (6) (1998) 3059–3071.

[215] M. Regnier, D. Lee, E. Homsher, Atp analogs and muscle contraction: mechanics and kinetics of nucleoside triphosphate binding and hydrolysis, Biophysical journal 74 (6) (1998) 3044–3058.

[216] T. Oda, M. Iwasa, T. Aihara, Y. Mada, A. Narita, The nature of the globular- to fibrous-actin transition, Nature 457 (7228) (2009) 441–445.

[217] V. Ropars, Z. Yang, T. Isabet, F. Blanc, K. Zhou, T. Lin, X. Liu, P. Hissier, F. Samazan, B. Amigues, E. Yang, H. Park, O. Pylypenko, M. Cecchini, C. Sindelar, H. Sweeney, A. Houdusse, The myosin x motor is optimized for movement on actin bundles, Science 7 (2016) 12456.

[218] B. A. Luty, J. A. McCammon, H.-X. Zhou, Diffusive reaction rates from brownian dynamics simulations: Replacing the outer cutoff surface by an analytical treatment, The Journal of chemical physics 97 (8) (1992) 5682–5686.

[219] D. Case, I. Ben-Shalom, S. Brozell, D. Cerutti, T. Cheatham, V. Cruzeiro, T. Darden, R. Duke, D. Ghoreishi, M. Gilson, H. Gohlke, A. Goetz, D. Greene, R. Harris, N. Homeyer, S. Izadi, A. Kovalenko, T. Kurtzman, T. Lee, S. LeGrand, P. Li, C. Lin, J. Liu, T. Luchko, R. Luo, D. Mermelstein, K. Merz, Y. Miao, G. Monard, C. Nguyen, H. Nguyen, I. Omelyan, A. Onufriev, F. Pan, R. Qi, D. Roe, A. Roitberg, C. Sagui, S. Schott-Verdugo, J. Shen, C. Simmerling, J. Smith, R. Salomon-Ferrer, J. Swails, R. Walker, J. Wang, H. Wei, R. Wolf, X. Wu, L. Xiao, D. York, P. Kollman, Amber 2018, University of California, San Francisco.

[220] J. Maier, C. Martinez, K. Kasavajhala, L. W. L, K. Hauser, C. Simmerling, ff14sb: Improving the accuracy of protein side chain and backbone parameters from ff99sb, J. Chem. Theory Comput 11 (2015) 3696–3713.

[221] S. Xu, J. Gu, B. Belknap, H. White, C. Y. Leepo, Structural characterization of the binding of myosin.adp.pi to actin in permeabilized rabbit psoas muscle, Biophysical journal 91 (9) (2006) 3370–3382.

[222] S. Teichman, K. Thomson, M. Regnier, Cardiac myosin activation with gene therapy produces sustained inotropic effects and may treat heart failure with reduced ejection fraction, Handb Exp Pharmacol 243 (2017) 447–464.

[223] S. Land, S. Niederer, A spatially detailed model of isometric contraction based on competitive binding of troponin i explains cooperative interactions between tropomyosin and crossbridges, PLoS Comput. Biol 11 (2015) e1004376.

[224] B. Tanner, T. Daniel, M. Regnier, Sarcomere lattice geometry influences cooperative myosin binding in muscle, PLoS computational biology 3 (7) (2007) e115.

[225] P. Chase, D. Martyn, J. Hannon, Isometric force redevelopment of skinned muscle fibers from rabbit activated with and without ca2+, Biophys J 67 (1994) 1994–2001.

[226] J. Powers, C. Yuan, K. McCabe, J. Murray, M. Childers, G. Flint, F. Moussavi-Harami, S. Mohran, R. Castillo, C. Zuzek, W. Ma, A. McCulloch, T. Irving, M. Regnier, Cardiac myosin activation with 2-deoxy-atp: A charged affair, PNAS (submitted).

[227] T. Dolinsky, J. Nielsen, J. McCammon, N. Baker, Pdb2pqr: an automated pipeline for the setup of poisson-boltzmann electrostatics calculations, Nucleic Acids Res 32 (2004) W665–7.

[228] I. Rayment, H. Holden, M. Whittaker, C. Yohn, Lorenz, K. Holmes, R. Milligan, Structure of the actin-myosin complex and its implications for muscle contraction, Science 261 (5117) (1993) 58–65.

[229] M. G. Palmgren, P. Nissen, P-type atpases, Annual Review of Biophysics 40 (2011) 243–266.

[230] A. Zarain-Herzberg, D. MacLennan, M. Periasamy, Characterization of rabbit cardiac sarco(endo)plasmic reticulum ca2+-atpase gene, J Biol Chem 265 (1990) 46704677.

[231] G. I. A. Prasad, R. Pilankatta, The ca2+atpase of cardiac sarcoplasmic reticulum: Physiological role and relevance to diseases, Biochemical and Biophysical Research Communications 369 (1) (2008) 182–187.

[232] T. Rensen, J. Ller, P. Nissen, Phosphoryl transfer and calcium ion occlusion in the calcium pump, Science 304 (2004) 16721675.

[233] D. Clarke, T. Loo, G. Inesi, D. MacLennan, Location of high affinity ca2+-binding sites within the predicted transmembrane domain of the sarcoplasmic reticulum ca2+-atpase, Nature 339 (1989) 476478.

[234] C. Olesen, T. Sorensen, R. Nielsen, J. V. Mller, , P. Nissen, Dephosphorylation of the calcium pump coupled to counterion occlusion, Science 306 (2013) 22512255.

[235] M. Bublitz, M. Musgaard, H. Poulsen, L. Thgersen, C. Olesen, B. Schitt, J. P. Morth, J. V. Mller, , P. Nissen, Ion pathways in the sarcoplasmic reticulum ca2+-atpase, Journal of Biological Chemistry 288 (15) (2013) 10759–10765.

[236] K. Tran, N. P. Smith, D. S. Loiselle, E. J. Crampin, A thermodynamic model of the cardiac sarcoplasmic/endoplasmic ca(2+) (serca) pump, Biophys J 96 (5) (2004) 2029–2042.

[237] M. Periasamyf, S. Huke, Serca pump level is a critical determinant of ca2+ homeostasis and cardiac contractility, J Mol Cell Cardiol 33 (2001) 10531063.

[238] S. Pogwizd, K. Schlotthauer, L. Li, W. Yuan, , D. Bers., Arrhythmogenesis and contractile dysfunction in heart failure: roles of sodium-calcium exchange, inward rectifier potassium current, and residual -adrenergic responsiveness, Circulation research 88 (11) (2001) 1159–1167.

[239] Y. Miao, V. Feher, J. McCammon, Gaussian accelerated molecular dynamics: Unconstrained enhanced sampling and free energy calculation, J. Chem. Theory Comput 11 (2015) 3584–3595.

[240] N. Drachmann, A. Sitsel, J. Andersen, P. Nissen, C. Olesen, Crystal structure of sarcoplasmic reticulum ca2+-atpase, to be published.

[241] Y. Himeno, K. Asakura, C. C. et al, A human ventricular myocyte model with a refined representation of excitation-contraction coupling, Biophys J 109 (2015) 415427.

[242] M. Olsson, C. Sondergaard, M. Rostkowski, J. Jensen, J Chem Theory Comput 7 (2011) 525–537.

[243] C. Sondergaard, M. Olsson, M. Rostkowski, J. Jensen, J Chem Theory Comput 7 (2011) 525–537.

[244] J. Autry, D. Thomas, J. Espinoza-Fonseca, Sarcolipin promotes uncoupling of the serca ca2+ pump by inducing a structural rearrangement in the energy-transduction domain, Biochemistry 55 (44) (2016) 60836086.

[245] Schrodinger release 2018-1: Maestro, Schrodinger, LLC, New York, NY.

[246] R. Friesner, J. Banks, R. Murphy, T. Halgren, J. Klicic, D. Mainz, M. Repasky, E. Knoll, D. Shaw, M. Shelley, J. Perry, P. Francis, P. Shenkin, Glide: A new approach for rapid, accurate docking and scoring. 1. method and assessment of docking accuracy, J. Med. Chem 47 (2004) 17391749.

[247] R. Friesner, R. Murphy, M. Repasky, L. Frye, J. Greenwood, T. Halgren, P. Sanschagrin, D. Mainz, Extra precision glide: Docking and scoring incorporating a model of hydrophobic enclosure for protein-ligand complexes, J. Med. Chem 49 (2006) 61776196.

[248] H. Autzen, M. Musgaard, Md simulations of p-type atpases in a lipid bilayer system. in: Bublitz m. (eds) p-type atpases, Methods in Molecular Biology 1377 (Humana Press, New York, NY).

[249] R. Bick, L. Buja, W. V. Winkle, G. Taffet, Membrane asymmetry in isolated canine cardiac sarcoplasmic reticulum: Comparison with skeletal muscle sarcoplasmic reticulum, The Journal of Membrane Biology 164 (2) (1998) 169175.

[250] C. Dickson, B. Madej, A. Skjevik, R. Betz, K. Teigen, I. Gould, R. Walker, Lipid14: The amber lipid force field, J. Chem. Theory Comput 10 (2) (2014) 865–879.

[251] J. Wang, R. Wolf, J. Caldwell, P. Kollman, D. Case, Development and testing of a general amber force field, Journal of Computational Chemistry 25 (2004) 1157–1174.

[252] J. Wang, W. Wang, P. Kollman, D. Case, Automatic atom type and bond type perception in molecular mechanical calculations, Journal of Molecular Graphics and Modelling 25 (2006) 247–260.

[253] K. Meagher, L. Redman, H. Carlson, Development of polyphosphate parameters for use with the amber force field, Journal of Computational Chemistry 24 (2003) 10–16.

[254] O. Allnr, L. Nilsson, A. Villa, Magnesium ion-water coordination and exchange in biomolecular simulations, J. Chem. Theory Comput 8 (2012) 1493–1502.

[255] D. Case, V. Babin, J. Berryman, R. Betz, Q. Cai, D. Cerutti, I. TE Cheatham, T. Darden, R. Duke, H. Gohlke, A. Goetz, S. Gusarov, N. Homeyer, P. Janowski, J. Kaus, I. Kolossvry, A. Kovalenko, T. Lee, S. LeGrand, T. Luchko, R. Luo, B. Madej, K. Merz, F. Paesani, D. Roe, A. Roitberg, C. Sagui, R. Salomon-Ferrer, G. Seabra, C. Simmerling, W. Smith, J. Swails, R. Walker, J. Wang, R. Wolf, X. Wu, P. Kollman, Amber 14, University of California, San Francisco.

[256] Y. Miao, J. McCammon, Gaussian accelerated molecular dynamics: Theory, implementation, and applications, Annu Rep Comput Chem 13 (2017) 231278.

[257] D. Roe, I. TE Cheatham, Ptraj and cpptraj: Software for processing and analysis of molecular dynamics trajectory data, J. Chem. Theory Comput 9 (7) (2013) 3084–3095.

[258] C. Toyoshima, T. Mizutani, Crystal structure of the calcium pump with a bound atp analogue, Nature 430 (2004) 529535.

[259] J. Clausen, D. McIntosh, B. Vilsen, D. Woolley, J. Andersen, Importance of conserved n-domain residues thr441, glu442, lys515, arg560, and leu562 of sarcoplasmic reticulum ca2+-atpase for mgatp binding and subsequent catalytic steps, J Biol Chem 278 (22) (2003) 20245–58.

[260] S. Hua, H. Ma, D. Lewis, G. Inesi, C. Toyoshima, Functional role of n(nucleotide) and p(phosphorylation) domain interactions in the sarcoplasmic reticulum (serca) atpase, Biochemistry 41 (7) (2003) 22642272.

[261] L. Espinoza-Fonseca, J. Autry, D. Thomas, Microsecond molecular dynamics simulations of mg2+-and k+-bound e1 intermediate states of the calcium pump, PLoS One 9 (4) (2008) e95979.

[262] M. Brini, E. Carafoli, Calcium pumps in health and disease, Physiological reviews 89 (4) (2009) 1341–1378.

[263] L. Espinoza-Fonseca, D. Thomas, Atomiclevel characterization of the activation mechanism of serca by calcium, PLoS One 6 (2008) e26936.

[264] C. Toyoshima, Structural aspects of ion pumping by ca2+- atpase of sarcoplasmic reticulum, Arch Biochem Biophys 476 (2008) 3–11.

[265] D. W. DL, J. Autry, B. Svensson, D. Thomas, Interdomain fluorescence resonance energy transfer in serca probed by cyan-fluorescent protein fused to the actuator domain, Biochemistry 47 (2008) 424656.

[266] P. KekenesHuskey, V. Metzger, B. Grant, J. McCammon, Calcium binding and allosteric signaling mechanisms for the sarcoplasmic reticulum ca2+ atpase, Protein Science 21 (10) (2012) 1429–1443.

[267] Y. H. H. L. Y. B. Y, Molecular dynamics simulation exploration of cooperative migration mechanism of calcium ions in sarcoplasmic reticulum ca 2+atpase, J Comput Chem 30 (2009) 21362145.

[268] Z. Zhang, D. Lewis, C. Strock, G. Inesi, M. Nakasako, H. Nomura, C. Toyoshima, Detailed characterization of the cooperative mechanism of ca 2+binding and catalytic activation in the ca 2+transport (serca) atpase, Biochemistry 39 (2000) 87588767.

[269] G. Inesi, M. Kurzmack, C. Coan, D. Lewis, Cooperative calcium binding and atpase activation in sarcoplasmic reticulum vesicles, J Biol Chem 255 (7) (1980) 3025–31.

[270] Z. Zhang, C. Toyoshima, The role of the m6m7 loop (l67) in stabilization of the phosphorylation and ca2+ binding domains of the sarcoplasmic reticulum ca2+atpase (serca), J Biol Chem 276 (2001) 1523215239.

[271] A. Einholm, Importance of transmembrane segment m1 of the sarcoplasmic reticulum ca2+atpase in ca2+ occlusion and phosphoenzyme processing, J Biol Chem 279 (2004) 1588815896.

[272] A. Lee, J. East, What the structure of a calcium pump tells us about its mechanism, Biochem J 356 (2001) 665.

[273] M. Musgaard, L. Thogersen, B. Schiott, E. Tajkhorshid, Tracing cytoplasmic ca2+ ion and water access points in the ca2+atpase, Biophys J 102 (2012) 268277.

[274] G. Inesi, D. L. D, C. Toyoshima, A. Hirata, L. de Meis, Conformational fluctuations of the ca2+atpase in the native membrane environment, J Biol Chem 283 (2008) 1189.

[275] B. Mueller, M. Zhao, I. Negrashov, R. Bennett, D. Thomas, Serca structural dynamics induced by atp and calcium, Biochemistry 43 (40) (2004) 1284612854.